JOHANN WOLFGANG GOETHE
UNIVERSITÄT
FRANKFURT AM MAIN

Millimetre-wave MIMO FMCW radar architecture towards highly integrated front-ends for high-resolution imaging applications

Dissertation
zur Erlangung des Doktorgrades
der Naturwissenschaften

vorgelgt beim Fachbereich Physik
der Johann Wolfang Goethe-Universität
in Frankfurt am Main

von
Marie Mbeutcha
aus Frankreich

Frankfurt am Main 2022

(D30)

Vom Fachbereich Physik der
J. W. Goethe-Universität als Dissertation angenommen.

Dekan: **Prof. Dr. Harald Appelshäuser**

Gutachter: **Prof. Dr.-Ing. habil. Viktor Krozer,**
Prof. Dr. Visvanathan Ramesh

Datum der Disputation:

Contents

Zusammenfassung

Das Radar ist die einzige bildgebende Technologie, die unabhängig von der Umgebung und den Wetterbedingungen eingesetzt werden kann, was sie zu einer äußerst zuverlässigen Lösung für hochauflösende Bildgebungsanwendungen macht. Dennoch müssen bildgebende Radarsysteme in Anwendungen wie Umweltüberwachung, Wolkenkartierung, Körpererfassung oder autonomes Fahren kritische Anforderungen erfüllen: hohe Auflösung, Kompaktheit, Skalierbarkeit und Effizienz. In dieser Arbeit wird eine modulare, moduliertes-Dauerstrichradar-Front-End-Lösung (FMCW) für solche Anwendungen vorgestellt. Die hohe Auflösung wird durch die Vergrößerung des Betriebsfrequenzbandes des Radarsystems erreicht. Dies kann bei Millimeterwellenfrequenzen aufgrund des großen verfügbaren Spektrums realisiert werden. Da die Größe der Komponenten mit zunehmender Frequenz abnimmt, sind Millimeterwellensysteme zudem ein guter Kandidat für Kompaktheit. Allerdings ist die vollständige Integration von Radar-Front-Ends bei Millimeterwellenfrequenzen aufgrund der schlechten Signalintegrität und spektrale Reinheit, die für bildgebende Anwendungen unerlässlich sind, eine Herausforderung. Das vorgeschlagene Radar verwendet eine alternative Technik und geht diese Einschränkung durch hochintegrierbare Architekturen an, insbesondere die Hartley-Architektur für die Signalumwandlung und den verbesserten Gegentaktverstärker für die Oberwellenunterdrückung. Die Auflösung abbildender Radargeräte kann durch die Erhöhung der Anzahl von Sendern und Empfängern weiter verbessert werden. Dies hat die Untersuchung von frequenz-, zeit- und energieeffizienten Multiplexing-Techniken für MIMO-Radarsysteme (Multi-Input-Multi-Output) vorangetrieben. Die in dieser Arbeit vorgeschlagene FMCW-Radararchitektur basiert auf der Code-Division-Technik (CDMA) mit Intra-Puls-Modulation. Diese fortschrittliche, skalierbare und nicht komplexe Lösung, die durch die neuesten Errungenschaften der direkten digitalen Synthese (DDS) zur Signalerzeugung ermöglicht wird, garantiert Signalintegrität und eine kompakte Implementierung. Die vorgeschlagene Architektur wird durch eine gründliche Systemanalyse untersucht. Ein Sender- und ein Empfängermodul für einen 35-GHz-Prototyp eines abbildenden Radars wurden entworfen, hergestellt und vollständig charakterisiert, um die Machbarkeit unseres neuen Ansatzes für hochauflösende, hochintegrierte MIMO-Front-Ends zu validieren. Dieser Demonstrator dient als Prototyp für eine zukünftige Single-Chip-Implementierung im W-Band.

Unseres Wissens nach ist diese Forschungsarbeit die einzige, die sich mit einem CDMA-basierten MIMO-FMCW-Radar mit Intrapulsmodulation im Millimeterwellenbereich befasst und dessen Theorie vollständig entwickelt. Darüber hinaus schlagen wir eine Lösung für hochintegrierte Front-Ends vor, die dennoch eine saubere spektrale Emission und eine zuverlässige Entfernungsmessung gewährleistet.

Signalmodell

Betrachten wir ein $N \times M$ MIMO-Radar mit N Sendern (Tx) und M Empfängern (Rx), einem m-PSK-Modulationsverfahren mit $m = 2^n$ und einer Familie von quasi-orthogonalen Codes ($c_i \in [1,N]$) der Länge N_c. Das Sendesignal an Tx i ist ein mit einem Code c_i phasenmoduliertes Chirp. Das empfangene Signal an Rx j ist die Summe der phasenmodulierten Chirps, die von allen Tx i gesendet werden und um die Laufzeit τ_{ij} verzögert sind. Durch des Deramps des empfangenen Signals r_j (t), d.h. Multiplikation des empfangenen Signals mit s_i (t), Filterung und Integration durch Fourier-Transformation, ist es möglich, den Bereich {Tx i, Ziel, Rx j} zu dekodieren und wieder zu erfassen.

Systementwurf und Analyse

Das Signal wird durch direkte digitale Synthese erzeugt. Starke Störsignale werden üblicherweise mit Bandpassfiltern hoher Ordnung unterdrückt, die häufig außerhalb des Chips eingebaut werden. Die größte Herausforderung für das System besteht darin, alternative Architekturen zu finden, die ihre Verwendung für die Single-Chip-Integration einschränken und gleichzeitig die Signalintegration und spektrale Reinheit aufrechterhalten. Die vorgeschlagene Architektur unterdrückt die aus der Mischung resultierende Bildfrequenz mit Hilfe einer modifizierten Version der herkömmlichen Hartley-Architektur. Sie umfasst einen IQ-Mischer mit einem 90°-ZF-Hybridkoppler sowie zwei LPF niedriger Ordnung in der Downconverter-Konfiguration. Die vorgeschlagene Architektur unterdrückt die von den Leistungsverstärkern (PA) erzeugten Oberwellen zweiter Ordnung mit Hilfe einer verbesserten Push-Pull-Architektur. Sie besteht aus zwei parallel geschalteten Leistungsverstärkern und zwei 180°-Hybridkopplern. Um die von den Kopplern verursachten Amplituden- und Phasenungleichgewichte zu begrenzen, wird die Verstärkung eines der Verstärker gesteuert, und wir verschieben die Phase in beiden Pfaden um 180°. Die Leistungsverstärker arbeiten in Sättigung, um die Ausgangsleistung im Vergleich zur Verwendung eines einzelnen PA zu verdoppeln. Je nach Reichweite verfügt das Radar über bis zu drei Verstärkerstufen bei der Zwischenfrequenz (ZF).

Die erwartete Leistung des Radars vor der Nachbearbeitung wird berechnet. Dabei wird der 3-dB-Verlust am HF-Eingangsanschluss des Empfängermoduls berücksichtigt. Für ein 1,05-GHz-Radar, das bei 35,3 GHz arbeitet, beträgt die Entfernungsauflösung etwa 15 cm. Die Verstärkung beträgt 27,5 dB, 45 dB, 62,5 dB und 80 dB für keine, eine, zwei bzw. drei ZF-Verstärkungsstufen.

Die Rauschzahl des Empfängers beträgt 6,28 dB. Die maximale Empfänger-Eingangsleistung beträgt -23 dBm, -38,5 dBm, -56 dBm bzw. -73,5 dBm. Dies entspricht einer Mindestreichweite von 0,69 m bis 12,7 m bei einem Radarquerschnitt von 1 dm^2, unterhalb derer das Radar in die Sättigung geht. Die Empfängerempfindlichkeit des Radars beträgt -62,4 dBm. Dies entspricht einer maximalen Reichweite von 6,69 m, oberhalb derer das Radar das Signal nicht ohne Nachbearbeitung analysieren kann. Die minimal wahrnehmbare Leistung beträgt -74,4 dBm. Der Dynamikbereich beträgt 51,4 dB, 35,9 dB, 18,4 dB bzw. 0,9 dB, was zeigt, dass das Radar in der Lage ist, das Signal in jeder Konfiguration zu erkennen. Die Ergebnisse sind daher zufriedenstellend. Die Empfindlichkeit des Empfängers kann verbessert werden, indem ein Schmalbandsignal gesendet wird. Dies bedeutet jedoch, dass das Rauschen des Empfängers auf Kosten der Entfernungsauflösung reduziert wird, was für die Bildgebungsanwendung nicht relevant ist. Die Verbindungsleistung kann durch eine Erhöhung der Sendeleistung oder eine Integration nach der Verarbeitung verbessert werden.

Systemsimulation des SISO FMCW-Radars

Eine Radarsimulationsumgebung, die eine realistische, auf dem Datenblatt basierende Geräteleistung emuliert, wird mit Keysight ADS, einem Referenz-CAD-Tool für den Systementwurf, entwickelt. Die frequenzabhängige Charakteristik der Nichtlinearität wird durch das Hintereinanderschalten eines nichtlinearen Blocks (typischerweise das nichtlineare Bauelement) zwischen zwei linearen Blöcken (typischerweise Filter) erreicht, wie durch den Wiener-Hammerstein-Modus zur Identifizierung nichtlinearer Systeme beschrieben. Die Antenne und die Wellenausbreitung zum Ziel basieren auf einem innovativen elektromagnetischen 3D-Ausbreitungsmodell. Die Systemvalidierung der vorgeschlagenen Radararchitektur wird für eine SISO-Konfiguration (single-input single-output) durchgeführt. Die Leistungsaufnahme beträgt 30 Watt, bestimmt durch die Leistungsverstärker. Eine frequenzbasierte Simulation des harmonischen Gleichgewichts zeigt, dass die vorgeschlagene Architektur eine Ausgangsleistung von 34,9 dBm liefern kann; dies ist auf die Verstärkung bei der Kombination beider Pfade des verbesserten Gegentaktverstärkers zurückzuführen. Die Hartley-Architektur und der verbesserte Gegentaktverstärker erreichen zusammen einen störungsfreien Dynamikbereich (SFDR) von 45,2 dBc innerhalb des Bandes und einen SFDR von 107,9 dBc außerhalb des Bandes, was besser ist als bei einer Architektur mit Bildunterdrückungsfiltern und die Signalintegrität erleichtert. Eine zeitbasierte Hüllkurvensimulation zeigt, dass das Deramp-Signal mit einem Signal-zu-Nebenkeulen-Verhältnis von 10 dBc klar erkannt wird, was für eine gute Signalintegrität spricht.

Systemsimulation des MIMO-FMCW-Radars bei Basisbandfrequenz

Es wird das Signalmodell des FMCW-MIMO-Radars mit Codemultiplexverfahren angewendet, das für die gleichzeitige Signalisierung mit allen Tx und den Empfang mit allen Rx vorgesehen ist.

Die Demonstration wird mit Matlab für ein Radar mit einer Bandbreite von 1,05 GHz, einer Entfernungsauflösung von ca. 15 cm und einer Pulsbreite von 500 µs bei einer Basisbandfrequenz durchgeführt. BPSK- und QPSK-Intrapuls-Modulationstechniken werden in verschiedenen Entfernungsszenarien verglichen. Die Ergebnisse zeigen, dass die Entfernungsschätzung mit einem zufriedenstellenden Haupt-zu-Nebenkeule-Verhältnis innerhalb eines bestimmten Coderatenbereichs am genauesten ist. Darüber hinaus hat die Intrapuls-Phasenmodulation den Vorteil, dass sie im Vergleich zur klassischen Pulsmodulation frequenz-, zeit- und energiesparend ist. Die hohe Coderate kann durch neueste DDS-Technologien erreicht werden.

Systemsimulation eines MIMO-FMCW-Radars bei Trägerfrequenz

Die vorgeschlagene Systemlösung wird mit Keysight ADS für ein 10-GHz-Radar bei 90 GHz mit einer Entfernungsauflösung von 16 mm und einer Pulsbreite von 500 µs bei Trägerfrequenz validiert. Die Demonstration wird schrittweise an einem 2x1 MIMO-Radar durchgeführt. Die Radararchitektur wird unter idealen Bedingungen simuliert. Es wird gezeigt, dass es in der Tat möglich ist, die Entfernungen von den verschiedenen Sendern wiederherzustellen, indem die Phase der verschiedenen gesendeten Chirps mit Gold-Codes moduliert wird und dann das klassische Deramping mit kodiertem Chirp von Tx 1 zur Identifizierung von Kanal 1 und von Tx 2 zur Identifizierung von Kanal 2 durchgeführt wird. Die Ergebnisse sind besonders vielversprechend, da die Kanalidentifizierung mit geringem Fehler bei der Bereichsschätzung erfolgreich durchgeführt werden kann. Beide Kanäle können mit einem Maximum von 0,42 % der Reichweite und einem Signal-Nebenkeulen-Verhältnis von 13 dBc identifiziert werden, was von einer ausgezeichneten Signalintegrität zeugt. Die Integrität kann durch die Wahl von Codes mit besserer Orthogonalität weiter verringert werden. Die Ergebnisse sind leicht auf ein 8×8-Radar skalierbar, da jede Sendeeinheit unterschiedliche quasi-orthogonale Codes hat und jede Empfangseinheit das gleiche Verhalten zeigt.

Entwurf der Senderschaltung und Messungen

Ein modularer Ka-Band-Sender für das Millimeterwellen-FMCW-Radar wurde auf der Grundlage der vorgeschlagenen fortschrittlichen Architektur entwickelt und gemessen. Der Sender ist ein Prototyp für zukünftige hochintegrierte Radar-Front-Ends. Er besteht aus oberflächenmontierten, Mikrostreifen- und Modulkomponenten, die alle bei W-Band-Frequenzen integriert werden können. Die Messergebnisse der Teilsysteme sind zufriedenstellend. Die Wandlungsverstärkung des Aufwärtswandlers beträgt 7 dB, die Oberseitenband-Bildunterdrückung 10 dBc, die LO-Unterdrückung liegt über 30 dBc. Das Bandpassfilter hat eine Einfügungsdämpfung von 5 dB, eine Eingangs- und Ausgangsrückflussdämpfung von 9 dB und eine Teilbandbreite von 8 %. Die Ausgangsleistung des Gegentaktsignals während der Sättigung beträgt 31,3 dBm und der 1-dB-Kompressionspunkt am

Ausgang liegt bei 31 dBm, was niedriger ist als erwartet in der Systemanalysis. Dies erklärt sich durch die große Größe des 180°-Hybridkoppler auf der Platine und die dadurch bedingte große Einfügungsdämpfung. Die Messungen des vollständigen Senders zeigen, dass die Bandbreite 34,3-35,8 GHz beträgt. Die Ausgangsleistung beträgt bis zu 24 dBm, und der 1-dB-Kompressionspunkt liegt bei 22,5 dBm. Die Bildunterdrückung und die LO-Unterdrückung liegen über 25 dBc. Die Eingangs- und Ausgangsrückflussdämpfung beträgt 15 dB. Die Messungen der vollständigen Senderkette, die noch vielversprechend sind, stimmen aufgrund eines plötzlichen Defekts auf der Platine nicht mit den Messungen des Subsystems überein.

Der Durchlassbereich des Senders ist im gewünschten Frequenzbereich von 35-36 GHz deutlich groß und flach. Die Störsignale werden gut unterdrückt. Dies validiert das vorgeschlagene System und macht es zu einem geeigneten Kandidaten für FMCW- und CDMA-basierte Intrapuls-Modulation für hochauflösende Bildgebungsanwendungen.

Entwurf der Empfängerschaltung und Messungen

Ein Prototyp eines Empfängers mit variabler Verstärkung bei 35 GHz wurde auf der Grundlage unserer vollständig simulierten neuen Architektur entwickelt und vollständig charakterisiert. Die Schaltungen der Empfängerplatinen wurden entworfen und kritische Punkte optimiert, insbesondere die HF-Übergänge, die Einseitenbandumsetzung und die variable ZF-Verstärkung. Die Messergebnisse werden für den Fall vorgestellt, dass die Platine eine ZF-Verstärkungsstufe enthält, wobei verschiedene Messmethoden verwendet wurden. Die Ergebnisse der verschiedenen Messungen sind trotz der unterschiedlichen Messmethoden konstant. Der vorgeschlagene Empfänger hat eine Bandbreite von 34,3-35,8 GHz. Die Umwandlungsverstärkung beträgt typischerweise 45 dB, ist relativ flach über der Eingangsfrequenz und konstant über dem Referenzsignal oder dem LO für die Dämpfung. Dies lässt eine gute Signalintegrität erwarten. Die Bildunterdrückung beträgt typischerweise 7 dBc. Die Eingangs- und Ausgangsrückflussdämpfung beträgt 9 dB. Der SFDR liegt bei 10 dBc. Dies zeugt von einer ausreichenden spektralen Reinheit. Die Messergebnisse stimmen vollständig mit der erwarteten Leistung des simulierten und in der Systemanalyse berechneten Empfängers überein. Dies bestätigt die Machbarkeitsstudie des vorgeschlagenen neuartigen Radarempfängers und zeigt, dass die Empfängerplatine für FMCW-Radaranwendungen zwischen 34,3 und 35,8 GHz vollkommen geeignet ist.

Abstract

High-resolution, compactness, scalability, efficiency – these are the critical requirements which imaging radar systems have to fulfil in applications such as environmental monitoring, cloud mapping, body sensing or autonomous driving. This thesis presents a modular millimetre-wave frequency modulated continuous-wave (FMCW) radar front-end solution intended for such applications. High-resolution is achieved by enlarging the operating frequency band of the radar system. This can be realized at millimetre-wave frequencies due to the large spectrum availability. Furthermore, the size of components decreasing with increasing frequency makes millimetre-wave systems a good candidate for compactness. However, the full integration of radar front-ends is a challenge at millimetre-wave frequencies due to poor signal integrity and spectral purity, which are essential for imaging applications. The proposed radar uses an alternative technique and tackles this limitation by featuring highly-integrable architectures, specifically the Hartley architecture for signal conversion and enhanced push-pull amplifier for harmonic suppression. The resolution of imaging radars can be further improved by increasing the number of transmitters and receivers. This has spurred the investigation of spectrum, time and energy-efficient multiplexing techniques for multi-input multi-output (MIMO) radar systems. The FMCW radar architecture proposed in this thesis is based on code-division technique using intra-pulse, also called intra-chirp modulation. This advanced scalable and non-complex solution, made possible by the latest achievements on direct digital synthesis for signal generation, guarantees signal integrity and compact size implementation. The proposed architecture is investigated by a thorough system analysis. A transmitter module and a receiver module for a 35 GHz imaging radar prototype are designed, fabricated and fully characterized to validate the feasibility of our novel approach for high-resolution highly-integrated MIMO front-ends.

Contribution to the State-of-the-Art

Code-division multiplexing techniques (CDMA) have been well-known and widely used in communications systems to identify a channel in the case of multiple users environment. This access technique has been recently investigated for radar technology. In this thesis, we aim to prove that it is indeed possible to apply the same principle to millimetre-wave FMCW radars. We propose an advanced intra-pulse-modulation-based MIMO CDMA FMCW radar architecture, and we aim to develop its theory going through all verification steps, that is:

- signal model,
- detailed system analysis and design,
- software implementation using Matlab and Keysight ADS, two acknowledged reference tools for system level simulations,
- hardware development using Keysight ADS and Ansys Electronics, reference tools for circuit design, and hardware characterization with comparison to simulation results for system validation.

To our knowledge, this research work is the only one tackling CDMA-based MIMO FMCW radar using intra-pulse modulation operating at millimetre-wave frequency and developing its full theory. In addition, we propose a solution for highly integrated front-ends which still guarantees a clean spectrum emission and a reliable range detection.

This research work led to the following publications:

(1) M. Mbeutcha and V. Krozer, 'CDMA-based MIMO FMCW radar system performance using intra-pulse phase modulation,' *2019 16th European Radar Conference (EuRAD)*, 2019, pp. 233-236.

(2) M. Mbeutcha, T. K. Johansen, Y. Dong, B. Cimoli and V. Krozer, 'Replicability of a millimeter-wave microstrip bandpass filter using parallel coupled lines,' *2018 IEEE MTT-S Latin America Microwave Conference (LAMC 2018)*, Arequipa, Peru, 2018, pp. 1-3.

(3) M. Mbeutcha, G. Ulisse and V. Krozer, 'Millimeter-wave imaging radar system design based on detailed system radar simulation tool,' *2018 22nd International Microwave and Radar Conference (MIKON)*, Poznan, Poland, 2018, pp. 517-520.

Chapter 1

Introduction

RADAR stands for RAdio Detection And Ranging. It is a wireless detection system that uses electromagnetic waves to determine the range, the angle, or the velocity of an object. The radar transmitter sends an electromagnetic wave towards an object, which is then back-scattered back to the receiver by this very object. By comparing the transmitted waveform to the received waveform, the radar can then estimate range, angle or velocity of the object. The range resolution is then the ability of the radar to separate two target-objects.

An imaging radar operates similarly but needs a very high range resolution not only to separate different targets, but also to be able to discern the different reliefs of the target-object and to pattern its shape. The target can then be recognized, and even classified.

1.1 Selecting FMCW radars systems for imaging applications

1.1.1 Radar, a highly reliable solution for imaging applications

There is a growing demand for high-resolution imaging for applications such as weather forecast, blind landing of space and aircraft, but also medical imaging and body sensing, autonomous driving, or non-destructive structural health monitoring of wind-turbine blades. These applications would commonly use camera imaging or LiDAR (laser Light Detection and Ranging) technology. Table 1-1 shows a comparison between all three technologies.

Camera sensors captures light photons from the electromagnetic spectrum. The light enters an enclosed box through a converging or convex lens and an image is recorded on a light-sensitive medium. Cameras are the cheapest and the most widespread sensors. They can also see colours and recognize texts. They can achieve a very high resolution, the best HD camera providing up to hundreds of millions of pixels nowadays. However, camera technology requires an extremely large amount of data to process the pixels and therefore the image. Moreover, cameras can estimate neither range nor velocity of an object, and they hardly see through materials.

Table 1-1: Comparison of Radar, LiDAR and Camera technologies

Performance	RADAR	LiDAR	Camera
Resolution	Low	Medium	High
Range detection	Yes	Yes	No
Motion detection	Yes	Yes	Yes
Velocity detection	Yes	Yes	No
Material penetration	High	Medium	Low
Color detection	No	No	Yes
Environment robustness	High	Medium	Low
Cost	Medium	High	Low
Data processing	Low	Low	High

Lidar sensors emit an eye-safe laser pulse to illuminate the target object or area. This pulse is back-scattered back to the lidar receiver. The distance to the target is estimated with the measurement of the time of flight. In addition, the intensity of light that is returned can give information on the size and the shape of the object under observation [1]. The main advantage of lidars over cameras, is that they can operate independently of the ambient lighting. Lidars can achieve high-resolution detection with light or in the dark, regardless external disturbances such as shadows or glares. Lidars also allow 3D imaging. Compared to camera, lidar image analysis is simpler and faster. More especially, the distance estimation to the object is straight-forward and does not require much signal post-processing. However, unlike cameras, lidars cannot recognize colours or interpret the text. The amount of data processed by lidars is still relatively large, and the technology is not yet cost-effective.

The operation of camera and lidar sensors can be hindered by snow, rain and fog. More especially, such weather conditions also change the refractive index of the transmission medium and reduce the range of a lidar sensor. Furthermore, it is difficult for cameras and lidars to see through materials, while radio waves can easily penetrate material which allow radars to also see through materials. Radar technology is the only technology which can operate regardless the environment and weather conditions which makes it a highly reliable solutions for high-resolution imaging applications. Radars are also cost-effective as their architecture can become very simple, and they do not require much signal post-processing, nor large amount of data to process the image. However, imaging radar suffers from a poor range or image resolution, in comparison to camera or lidar technologies. Therefore, for safety-critical applications such as autonomous driving, radar technology tends to be associated to camera and lidar sensors in order to guarantee highest image resolution regardless the environmental conditions. It is therefore crucial to improve radar performance, while guaranteeing a cost-effective sensor which is small, low power and efficient.

1.1.2 FMCW, a viable waveform for imaging applications

Radars can either emit continuous waveforms or pulse waveforms.

Pulse radars transmit short and high-power pulses and in silent period receive the echo signals [2]. They are usually implemented for long distance measurements. Pulse radars benefit from a better range resolution as the bandwidth is substantially large. They can provide a high peak-to-sidelobe ratio after pulse integration. Finally, multi-target detection is easily achievable. However, pulse radars have a poor power efficiency as the active components are working continuously while the radar emits on a short period. They also require a strict time control and a delay correction algorithm to correctly estimate the range. They necessitate a protective receiver architecture in the monostatic case, or highly directive antenna in the bistatic case, to prevent the high-power transmitted pulse from leaking into the receiver. Finally, when the object is too close to the radar, the back scattered power becomes too high and it is impossible for the radar to detect anything. This blind spot sets a limit to the minimum range detection that can be achieved.

On the contrary, continuous wave (CW) radar have the advantage of operating well for short and mid-range detection. They feature a simple system architecture and are power efficient. However, simple continuous wave radars cannot determine the range because it lacks the timing mark necessary to allow the system to time accurately the transmit and receive cycle and to convert this into range. CW radars are typically used for velocity or motion detection.

To allow range detection, another degree of freedom is added by modulating in frequency (or in phase) a simple continuous waveform. Thus frequency-modulated continuous wave (FMCW) radars can change its operating frequency during the measurement, which allows real-time detection. FMCW radars also have the ability of measuring simultaneously both target range and velocity and have a very high range estimation accuracy. The range resolution of a radar is inversely proportional to its bandwidth B and is equal: $S_r = c/2B$ where c is the speed of light. FMCW radars having a large bandwidth, there are an excellent candidate for high-resolution radar imaging. Besides, FMCW radars process the signal at low frequency, which simplifies drastically the radar architecture after mixing. Finally, the receiver does not need to be protected from high-power pulse leakage or back-scattering. The hardware simplicity of FMCW radars combined with the quality of both range and velocity estimation makes it a viable candidate for many cost-effective radar applications.

1.2 Decreasing the size of radar front-end at mm-wave frequency: a challenge

For various imaging applications, the size and the weight of radar systems can be critical. For aero-space applications, the heavier the space or aircraft, the more expensive. Thus, it is indispensable to manufacture the lightest radar devices. A future autonomous car is likely to feature hundreds of radars; therefore, the size of the radar system should be reduced to its minimum.

The larger the frequency, the smaller the size of the device. Thus, in the millimetre-wave (mm-wave) frequency range, the size of the components scales down to millimetre and sub-millimetre dimensions. This enables the high integration of radar front-ends, and thereby compact-size and light-weight radar systems. In addition, there is a large spectrum availability at mm-wave frequency. It is then possible to increase the bandwidth of the mm-wave radars systems and therefore improves the range resolution [3]-[5]. This makes mm-wave radar attractive for other high-resolution imaging applications such as medical imaging or non-destructive structural health monitoring.

Heterodyne FMCW radar using direct digital synthesis (DDS) as signal generation is a good candidate for such highly-integrated high-resolution imaging systems due to its good sensitivity, selectivity, calibration and the possibility of processing the chirp signal at low frequency [6]. However, the interferences created by nonlinear elements, especially the image frequency due to mixing, and the harmonics generated by amplifiers with medium to high output power levels, deteriorate the signal integrity and the spectral purity. Their suppression is essential as the spectrum allocation for emission is usually very strict. For radar applications, it is crucial to correctly filter out these interferences, as they would backscatter toward the receiver. More especially, the image frequency coming from the transmitter, but also from other coexisting devices, could be down-converted to the intermediate frequency of interest to the same level as the carrier frequency, which could strongly deter the signal integrity of the radar, and therefore the range detection [7]. These interferences are conventionally suppressed with high-order bandpass filters (BPF). When operating at higher millimetre-wave frequencies, typically larger than 80 GHz, these filters become very large with respect to other InP, GaAS components and can therefore only be built off-chip. It is then necessary to find an advanced architecture which limits the use of high-order bandpass filters to allow fully integrated front-ends, while guaranteeing both signal integrity and spectral purity. The limitation of high-order bandpass filters is all the more critical, as recent studies have proven that components with large group delay, particularly high-order BPF, deteriorate significantly signal integrity and therefore the range estimation in FMCW radar technology [8],[9].

1.3 Increasing the number of radar channels for higher resolution: another challenge

1.3.1 MIMO, an effective solution for resolution improvement

To further improve the performance of radar imaging systems and particularly the resolution, further investigation focusing on multi-input multi-output (MIMO) radars has been carried out [10]-[12]. The virtual aperture of MIMO radars can be enlarged by increasing the number of transmitters (Tx) and receivers (Rx). This could improve angular resolution, interference robustness and probability of detection in comparison to classic single-input single-output radar systems.

Typical MIMO radar systems operate either in time division multiplexing (TDM), frequency division multiplexing (FDM), or code division multiplexing (CDM). Increasing the number of Rx is generally not a problem from the system perspective. However, increasing the number of Tx increases either the acquisition time in TDM or the receiver bandwidth in FDM systems. Therefore, focus has been lately on CDM systems with Tx transmitting orthogonal Tx waveforms in order to identify the Tx signals at each receiver.

1.3.2 CDM, a scalable and noncomplex access technique for MIMO FMCW radars

The analysis of MIMO radar systems in terms of the channel multiplex is best achieved by applying techniques known from communications channel simulations. In these terms, to share the channel between the different Tx units, time-, frequency- and code-division multiple access techniques (respectively TDMA, FDMA and CDMA) have been successfully applied. Orthogonality of MIMO radar waveforms can be achieved using TDMA where each Tx unit transmits in a specific time slot so that there is no overlapping between the transmitted signals. This architecture benefits from the simplicity of its hardware implementation and modulation scheme [10]. However, a strict synchronization of both its Tx and Rx units is required, and TDMA-based radars suffer from poor transmitted power efficiency. In addition, data acquisition is lengthened by N-times the time slot, where N is the number of transmitters. In the FDMA approach, orthogonality is achieved by modulating each Tx signal by a specific baseband frequency. In classic implementations, the total allocated bandwidth is divided by the number of transmitters N. Each Tx sends a chirp in a reduced baseband bandwidth and processing methods are develops to recover the lost bandwidth virtually [11]. This makes the technique inadequate to FMCW where the resolution is directly proportional to the actual bandwidth of the system. In addition, such systems necessitate a consequential hardware implementation. Another idea is to transmit chirp signals with full bandwidth at each Tx, modulated by shifted RF frequencies. This method is prohibitive as this requires a baseband bandwidth of N × baseband frequency at the receiver. In

CDMA technique, unique sequences of a quasi-orthogonal code family modulate the transmitted signals, which are then separated at the Rx. The realization of CDMA-based MIMO radar can also suffer of difficult hardware implementation and the range estimation strongly depends on the correlation properties of the code family [12]. However, recent developments in direct-digital synthesis (DDS) such as in [13],[14] enable very fast phased-control FMCW up- and down-chirp generation. This could simplify drastically CDMA-based radar architecture. Furthermore, this technique could allow scalability to a high number of Rx and Tx and support arbitrary Tx-Rx constellations [15], making it an excellent candidate for high-resolution compact radar systems. Table 1-2 summarizes the performance of the multiplexing techniques used for FMCW radars.

Table 1-2: Comparison of MIMO FMCW radar multiplexing techniques

Access techniques	**TDMA**	**FDMA**	**Novel CDMA**
Authors	Belfiori et al.	Cohen et al.	Our work
HW complexity	low	high	low
Modulation scheme	low	medium	medium
Tx-Rx synchronization	yes	no	no
Resolution	maintained	impacted	maintained
Spectrum efficiency	high	low	high
Time efficiency	low	high	high
Energy efficiency	low	medium	high

1.3.3 Intra-pulse phase modulation, a substantial solution for channel identification

The amplitude of the received signal, after reflection on the target, depends on the channel but also on the target properties (permittivity, cross section…), which are in general unknown and extremely variable across the object and across time. Thus, we focus on phase modulation since additional amplitude modulation may be distorted after reflection on the target. By modulating the chirp in phase using quasi-orthogonal codes for the different transmitters, we expect to recover the range from a given transmitter without additional hardware requirements and time or spectral resources.

1.4 Objectives of this research work

We present an advanced high-resolution imaging radar solution operating at millimetre-wave frequencies. The proposed architecture is depicted in Figure 1-1. The signal generation is based on frequency- and phased- controlled direct digital synthesis (DDS). The architecture limits the use of high-order off-chip bandpass filters to allow future highly integrated front-ends, while guaranteeing signal integrity and spectral purity. The radar design is modular in order to allow

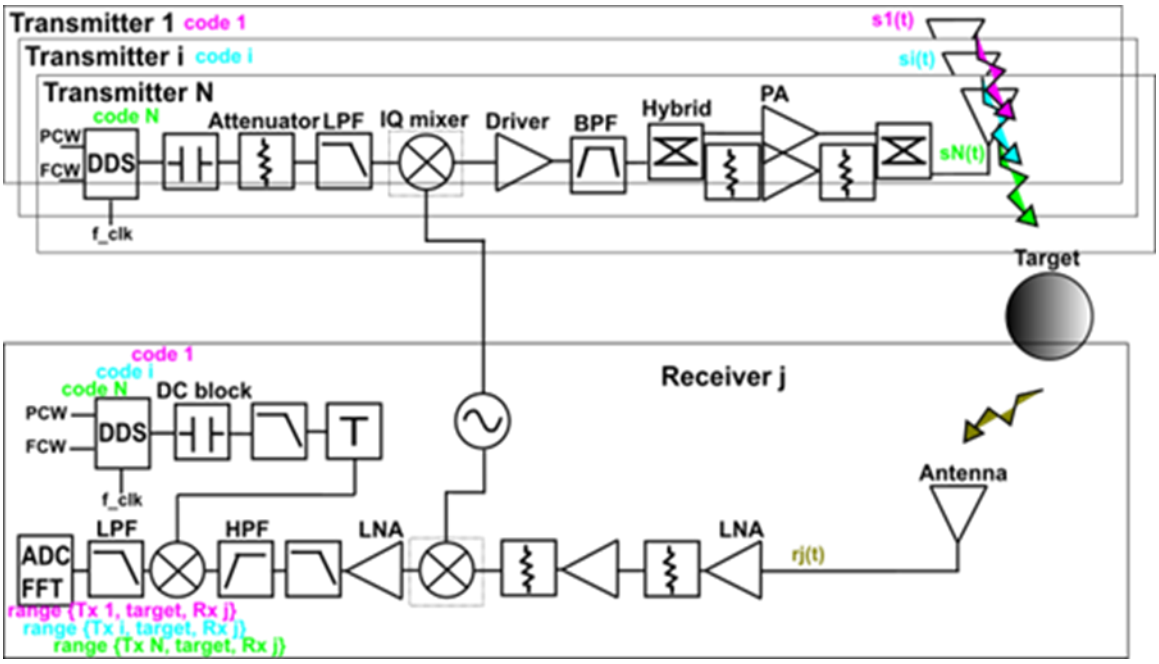

Figure 1-1: Proposed CDMA-based MIMO FMCW radar front-ends architecture

MIMO implementation. We propose a novel multi-channel FMCW radar model based on CDM intra-pulse also called intra-chirp modulation. This system is spectrum-, power-, time- and cost-effective and still guarantees a high-resolution and accurate range detection, and therefore imaging capability. The feasibility demonstration is performed at 35 GHz. It is developed for wind turbine structural health monitoring in the 33.4-36 GHz spectral band allocated by the German Federal Network Agency for this purpose. All the components of the transmitter and receiver modules are commercial devices using surface mount technology (SMT), excepted the bandpass filter and the 180° hybrid which are self-designed on microstrip. This demonstrator serves as feasibility prototype to be scaled up to higher millimetre-wave frequencies, typically in the W-band.

Chapter 2 presents the signal and channel model of the proposed MIMO FMCW radar. Chapter 3 addresses the system design of the SISO radar. The techniques used to enable the integration of the front-ends are demonstrated. An extensive link budget is analysed to anticipate the performance of the radar system. Chapter 4 presents a detailed system simulation method of the SISO architecture. Chapter 5 demonstrates the feasibility of the proposed MIMO model for FMCW radar at baseband frequencies. The demonstration is extended at carrier frequencies in Chapter 6 and carried out step-by-step. Chapter 7 and Chapter 8 presents the circuit design and the measurement results of the transmitter and receiver module respectively, characterized at 35 GHz. Chapter 9 concludes this research work and proposes further solutions.

Chapter 2

Signal model

In this Chapter, we describe the signal model of a CDMA-based bi-static MIMO FMCW radar using intra-pulse phase modulation.

2.1 Principle of FMCW radar technique

Let us consider a single-input single-output (SISO) bi-static FMCW radar, of initial frequency f_0, bandwidth B and ascending chirp duration T. The instantaneous frequency for one chirp can be expressed:

$$v(t) = \frac{1}{2\pi}\frac{d\varphi_s}{dt} = f_0 + \frac{B}{T}t \qquad (2\text{-}1)$$

where $\varphi_s(t)$ is the phase of the transmitted chirp, and $t \in [0, T]$. If $\varphi_0$is the arbitrary initial phase, then:

$$\varphi_s(t) = 2\pi f_0 t + 2\pi\frac{B}{2T}t^2 + \varphi_0 \qquad (2\text{-}2)$$

Thus, the transmitted signal can be written:

$$s(t) = A_s\cos\big(\varphi_s(t)\big) \qquad (2\text{-}3)$$

If the radar and the target are both static, the received signal $r(t)$ is attenuated and delayed by the time τ corresponding to the distance {Tx, target, Rx}. If A_r is the amplitude of the received signal, $r(t) = A_r\cos\big(\varphi_r(t)\big) = A_r\cos\big(\varphi_s(t-\tau)\big)$ with:

$$\tau = \frac{R_{Tx\to target} + R_{target\to Rx}}{c} \qquad (2\text{-}4)$$

c being the speed of light, and $R_{A\to B}$ the distance from point A to point B.

The range detection unfolds in three steps. This process is called de-ramping. In a first step, the received signal is mixed with the transmitted signal to which an offset $\tau_0 < \tau$ is applied. The mixing product is the signal:

$$d_1(t) = s(t)\, r(t) \quad (2\text{-}5)$$

$$d_1(t) = A_s \cos\big(\varphi_s(t-\tau_0)\big)\, A_r \cos\big(\varphi_s(t-\tau)\big) \quad (2\text{-}6)$$

$$d_1(t) = \frac{A_s A_r}{2}\left[\cos\big(\varphi_s(t-\tau_0) + \varphi_s(t-\tau)\big) + \cos\big(\varphi_s(t-\tau_0) - \varphi_s(t-\tau)\big)\right] \quad (2\text{-}7)$$

In a second step, the high frequency component is filtered. The mixing product becomes:

$$d_2(t) = \frac{A_s A_r}{2}\left[\cos\big(\varphi_s(t-\tau_0) - \varphi_s(t-\tau)\big)\right] \quad (2\text{-}8)$$

In the third step, we determine the instantaneous frequency. The phase $\theta(t)$ of $d_2(t)$ is:

$$\theta(t) = \pm|\varphi_s(t-\tau_0) - \varphi_s(t-\tau)| \quad (2\text{-}9)$$

Thus, we set:

$$\theta_+(t) = \varphi_s(t-\tau_0) - \varphi_s(t-\tau) \quad (2\text{-}10)$$

Or,

$$\theta_-(t) = \varphi_s(t-\tau) - \varphi_s(t-\tau_0) \quad (2\text{-}11)$$

If $\theta(t) = \theta_-(t)$ then:

$$\theta(t) = 2\pi f_0(t-\tau) + 2\pi\frac{B}{2T}(t-\tau)^2 - 2\pi f_0(t-\tau_0) - 2\pi\frac{B}{2T}(t-\tau_0)^2 \quad (2\text{-}12)$$

After deriving and simplifying, the received phase reads:

$$\theta(t) = -2\pi f_0\tau - 2\times 2\pi\frac{B}{2T}t\tau + 2\pi\frac{B}{2T}\tau^2 + 2\pi f_0\tau_0 + 2\times 2\pi\frac{B}{2T}t\tau_0 - 2\pi\frac{B}{2T}{\tau_0}^2 \quad (2\text{-}13)$$

Finally, from the received phase can be deducted the instantaneous frequency $f_b{}'$ (see equation (2-1)) which we will call, the measured beat frequency.

$$f_b' = \frac{1}{2\pi}\frac{d\theta}{dt} = \frac{B}{T}(\tau_0 - \tau) \quad (2\text{-}14)$$

If $\theta(t) = \theta_+(t)$, we proceed as before:

$$\theta(t) = 2\pi f_0(t-\tau_0) + 2\pi\frac{B}{2T}(t-\tau_0)^2 - 2\pi f_0(t-\tau) - 2\pi\frac{B}{2T}(t-\tau)^2 \quad (2\text{-}15)$$

After derivation and simplification of the terms, the phase becomes:

$$\theta(t) = -2\pi f_0 \tau_0 - 2 \times 2\pi \frac{B}{2T} t\tau_0 + 2\pi \frac{B}{2T} \tau_0^2 + 2\pi f_0 \tau + 2 \times 2\pi \frac{B}{2T} t\tau - 2\pi \frac{B}{2T} \tau^2 \quad (2\text{-}16)$$

The instantaneous frequency or measured beat frequency is:

$$f_b' = \frac{1}{2\pi} \frac{d\theta}{dt} = \frac{B}{T}(\tau - \tau_0) \quad (2\text{-}17)$$

Considering that $\tau_0 < \tau$ and the case $\tau_0 = 0$, we select $\theta(t) = \theta_+(t)$. Thus, the measured beat frequency is a function of the classic beat frequency $f_b = \frac{B}{T}\tau$ when $\tau_0 = 0$ and the offset beat frequency $f_{b,0} = \frac{B}{T}\tau_0$.

$$f_b' = f_b - f_{b,0} \quad (2\text{-}18)$$

The beat frequency can be measured on the spectrum of the de-ramp signal [16]. From the measured beat frequency, we can estimate the range:

$$f_b' = \frac{B}{T}\left(\frac{R_{Tx \to target} + R_{target \to Rx}}{c} - \tau_0\right) \quad (2\text{-}19)$$

$$R_{Tx \to target} + R_{target \to Rx} = c\left(f_b' \frac{T}{B} + \tau_0\right) \quad (2\text{-}20)$$

Note that the estimation of the range does not depend on the initial phase φ_0, nor the amplitude of the transmitted A_s or received signal A_r.

In the case on mono-static radar of range *R* = $R_{Tx \to target} = R_{target \to Rx}$ and when $\tau_0 = 0$, the range becomes:

$$R = c f_b \frac{T}{B}, \qquad f_b' = f_b \quad (2\text{-}21)$$

For long-range detection, the time of travel τ becomes substantially large and consequently the beat frequency too. Therefore, in practice, the offset τ_0 is increased step-by-step in order to reduce the beat frequency in the kilohertz range. This technique reduces drastically the hardware complexity, as most commercial ADC can achieve this sampling frequency.

For a series of N_P chirps, the signal is transformed into a sum of translated chirps:

$$s(t), t \in [0, T] \to \sum_{k=0}^{N_p - 1} s(t - kT), t \in [kT, (k+1)\,T] \quad (2\text{-}22)$$

and the theory remains unchanged. For a chirp *k*,

$$s_k(t) = A_s \cos\big(\varphi_s(t - kT)\big) \quad (2\text{-}23)$$

$$r_k(t) = A_r \cos\big(\varphi_s(t - kT - \tau)\big) \quad (2\text{-}24)$$

and

$$\theta_k(t) = \varphi_s(t - kT) - \varphi_s(t - kT - \tau) \quad (2\text{-}25)$$

leading to f_B [17].

Finally, a typical cross-correlator receiver consists of three stages: mixing the received signal with a sliding (delayed) reference signal, low-pass filtering and integrating. Likewise, the de-ramping technique of a FMCW radar is similar to cross-correlation [18],[19] i.e. matched filtering.

2.2 Introducing MIMO channel model

For a multi-input multi-output (MIMO) bi-static FMCW radar, of initial frequency f_0, bandwidth B and ascending chirp duration T, the signal transmitted at Tx *i* becomes for N_p pulses:

$$s_i(t) = \sum_{k=0}^{N_p-1} A_{s_i} \cos\Big(\varphi_{s_i}(t - kT)\Big), t \in [kT, (k+1)\,T] \quad (2\text{-}26)$$

Then if:

$$\tau_{ij} = \frac{R_{i\to target} + R_{target\to j}}{c} \quad (2\text{-}27)$$

α_{ij} the attenuation of the path {Tx *i*, target, Rx *j*} that we suppose time-invariant, and $n_j(t)$ is the additive white Gaussian noise, the received signal at Rx *j* becomes:

$$r_{k,j}(t) = \sum_{i=1}^{N} \alpha_{ij} \cdot s_i\big(t - \tau_{ij}\big) + n_j(t) \quad (2\text{-}28)$$

2.3 Introducing code-division technique

We consider a *N*×*M* MIMO radar having *N* Tx and *M* Rx. We consider a *m*-PSK (phase-shift keying) modulation scheme, with $m = 2^n$. In *m*-PSK modulation, one symbol corresponds to *n* chips of codes. We use a family of quasi-orthogonal codes ($c_{i \in [1,N]}$) of length N_c. The symbol duration of the spreading sequence is T_c. The symbol repetition period is T_r.

We set $T_c = T_r = nT/N_c$ so that a whole code sequence modulates a single pulse. Figure 2-1 illustrates the intra-pulse modulation scheme using BPSK and QPSK, respectively binary phase-shift keying and quadrature phase-shift keying. The symbol rate is N_c/nT Hz. The chirp signal transmitted at Tx *i* is expressed:

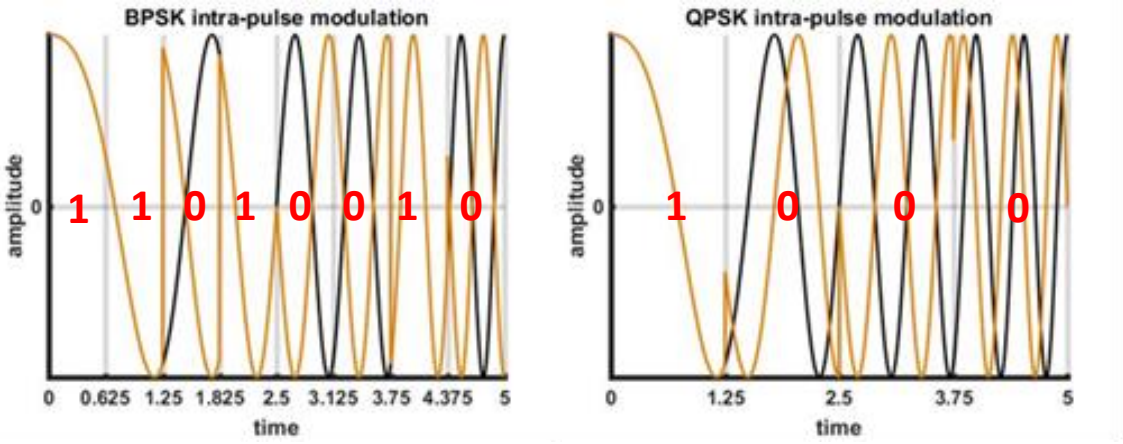

Figure 2-1: Intra-pulse modulation using BPSK (m = 2) and QPSK (m = 4).
Coded chirp is in gold and non-coded chirp is in black (scaled-down parameters for better visibility).

$$s_i(t) = \sum_{l=1}^{N_c/n} \text{rect}(N_c t/nT - (2l-1)/2)\, A_i \cos\left(\varphi_{s_i}(t) - d_{i,l}\right) \qquad (2\text{-}29)$$

Where rect($N_c t/nT - (2l-1)/2$) is the rectangular function centered in $(2l-1)nT/2N_c$, of width nT/N_c, and $d_{i,l} \in \{k\pi/2^{n-1}\}$, $k = [0..m-1]$, $l = [1..N_c/n]$ are the phase shifts corresponding to the coding sequence symbols of length n, of 2^n combinations of 0s and 1s (0000..00, 0000..01, 0000..10, …, 1111..11).

Thus, the received signal at Rx j is:

$$r_j(t) = \sum_{i=1}^{N} \alpha_{ij} \sum_{l=1}^{N_c/n} \text{rect}\left(N_c\left(t-\tau_{ij}\right)/nT - (2l-1)/2\right) A_i \cos\left(\varphi_{s_i}\left(t-\tau_{ij}\right) - d_{i,l}\right) \qquad (2\text{-}30)$$

In the same way, de-ramping that is, multiplying the received signal by $s_i(t)$, filtering and integrating by Fourier transform is enough to decode and recollect the range {Tx i, target, Rx j}.

For BPSK, $m = 2$ and $n = 1$. The phase shifts become $d_{i,l} \in \{0, \pi\}$ which corresponds to a shift of {1,-1} in amplitude respectively. This can be simplified by the coding symbols $c_{i,l} \in \{-1, 1\}$, $l = [1..N_c]$. This leads to the following transmitted and received signal models respectively:

$$s_i(t) = \sum_{l=1}^{N_c} c_{i,l} \text{rect}(N_c t/T - (2l-1)/2)\, A_i \cos\left(\varphi_{s_i}(t)\right) \qquad (2\text{-}31)$$

$$r_j(t) = \sum_{i=1}^{N} \alpha_{ij} \sum_{l=1}^{N_c} c_{i,l} \mathrm{rect}\big(N_c\big(t - \tau_{ij}\big)/T - (2l-1)/2\big) A_i \cos\Big(\varphi_{s_i}\big(t - \tau_{ij}\big)\Big) \quad (2\text{-}32)$$

For QPSK, m = 4 and n = 2. The phase shifts become $d_{i,l} \in \{0, \pi/2, \pi, 3\pi/2\}$ corresponding to the coding sequence symbols {11, -11, -1-1, 1-1} respectively.

2.4 Summary and remarks

We developed and presented the signal model of the proposed MIMO CDMA-based FMCW radar architecture using intra-pulse phase modulation. We use a family of quasi-orthogonal codes and we assign a code to each transmitter. Each transmitter sends a chirp signal modulated in phase by this code. The received signal is the sum of the coded chirps sent by all transmitters and delayed by the time of travel corresponding to the round trip to the target. We can identify the channel to a specific transmitter and recover the range by simply deramping the received signal with the coded chirp from this very transmitter.

Chapter 3

System design and analysis

This Chapter presents an extensive system study of the proposed radar architecture. Without loss of generality, we carry out the system design for a SISO architecture as each module of the MIMO system is similar.

3.1 System requirements and challenges

The first system challenge is to find an alternative architecture limiting the use of high-order bandpass filter for single-chip integration, while still maintaining signal integration and spectral purity. Other challenges for mm-wave large-band receivers are the power and noise. Indeed, the input power is typically very low because the propagation loss is particularly high when the frequency increases. The thermal noise is directly proportional to the bandwidth and will be added to any noise produced by the elements of the receiver chain. Therefore, a correct dimensioning of the receiver is crucial, so that the signal can be amplified enough without adding too much noise. This will guarantee a good output signal-to-noise ratio (SNR), a good sensitivity and the possibility of sampling the signal at the receiver output.

3.2 Block diagram

Figure 3-1 depicts the block diagram of the proposed 35 GHz SISO radar front-end. The radar front-end is modular. The transmitter consists of a DDS-based intermediate frequency (IF) signal generation stage, an up-converter stage, and two amplification stages. The up-conversion from IF frequency to mm-wave frequencies is accomplished using synthesized local oscillator (LO) signals of phase noise -107 dBc/Hz at 100 kHz. To suppress the resulting strong image frequency, a modified Hartley architecture is implemented, featuring a sub-harmonic in-phase and quadrature (IQ) mixer coupled with a 90° hybrid and a single 3rd order BPF filter at the driver output. Finally, to decrease the second harmonic distortion created by the power amplifier operating in saturation, an enhanced push-pull amplifier using 180° hybrid couplers is utilized. The push-pull architecture comprises two attenuators to compensate for the gain balance from

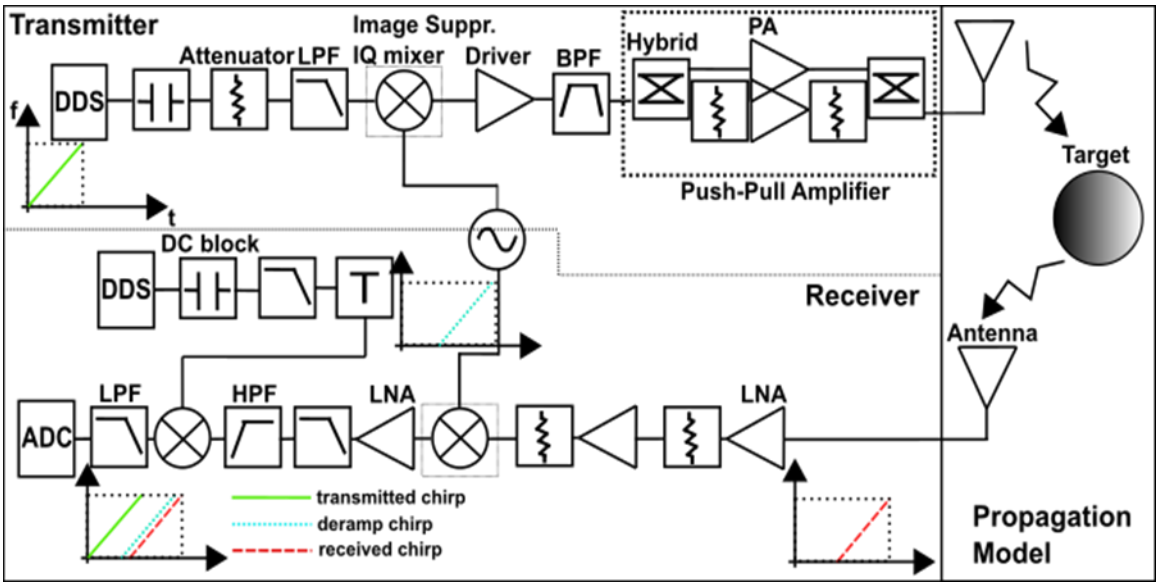

Figure 3-1: Proposed SISO FMCW radar front-ends architecture

the couplers. The receiver is composed of two low-noise amplifier stages at carrier frequencies due to the low power level received from the target and a super-heterodyne down-conversion stage. The down-conversion features an image suppression down-converter in Hartley architecture, followed by a simple down-conversion stage for deramping, where the LO signal is replaced by a delayed chirp signal generated by a DDS and synchronized with the transmitter [20]. The intermediate frequency signal between both down-conversion stages is amplified up to three stages. Each IF amplification stage comprises a low-noise amplifier (LNA) followed by cascaded low-pass filter (LPF) and high-pass filter (HPF). A serial low-pass filter and high-pass filter is preferred instead of a bandpass filter to have a steeper DC cut-off.

3.3 Bill of materials

The selected SMT radiofrequency (RF) components are listed in Table 3-1. The criteria of selection included operational band, availability, and performance according to the data from [21]-[37]. A complete list bill of materials is available in Annex A. At the time of development, no commercial SMT bandpass filter, nor 180° hybrid coupler were available at 35 GHz.

Table 3-1 Bill of Materials (partial).

Description	Manufacturer	Part number
SMA connector	Amphenol	901-10515-1
SMA connector	Southwest	292-07A-6
DC-Block	Dielectric Labs	C04BL121X-5UN-X0B
3 dB-attenuator	Anaren	D10AA3Z4
Lowpass Filter	Mini-Circuits	LFCN-1575
90° hybrid	Innovative Power Products	IPP-7116
Ku-band Upconverter	Qorvo	TGC4546-SM
Driver amplifier	Analog Devices	HMC635LC4
Power amplifier	Analog Devices	HMC7229LS6
Connector 2.4 mm	Southwest	1492-04A-6
LNA (RF)	UMS	CHA2494-QEG
Attenuator	UMS	CHT4694-QAG
I/Q Downconverter	Analog Devices	HMC6789BLC5A
Hybrid 90°	Innovative Power Products	IPP-7116
LPF	Mini-Circuits	LFCN-1575+
LNA (IF)	Analog Devices	HMC8410LP2FE
HPF	Mini-Circuits	RHP-65+
Mixer	Mini-Circuits	ADE-R5LH+

Components required for biasing network (capacitors, inductors and resistors) are not listed.

3.4 Sideband suppression: modified Hartley architecture

Mixers convert an IF signal into an RF signal and its image at same level. The classic Hartley architecture is a well-known architecture which allows the suppression of a sideband signal (or image signal) in up- and down-conversion [38],[39]. In our radar system, we modify the Hartley architecture and adapt it to classic commercial components, namely IQ mixers and 90° hybrid. We show that the modified Hartley architecture can still suppress a given sideband, in either up- or down-conversion. Figure 3-2 recalls the port appellation of the 90° hybrid.

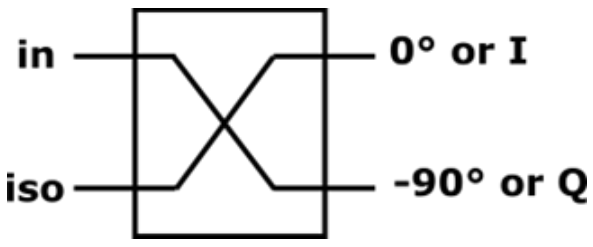

Figure 3-2: 90° hybrid coupler symbol

3.4.1 Sideband suppression in up-conversion

Figure 3-3 shows the modified Hartley architecture for single-sideband (SSB) up-conversion and the spectrum of the signal. In the proposed architecture, the up-conversion block consists of an IQ up-converter i.e. two mixers fed with in-phase LO signals, followed by a 90° RF hybrid coupler. Without loss of generality, the "Q", quadrature port of the 90° hybrid is terminated by a 50 Ohm load. We will demonstrate that single-sideband up-conversion can be achieved by adding a 90° IF hybrid at the input, and by applying the IF signal in the "input" port for upper sideband rejection (see Figure 3-3 a), or "isolated" port for lower sideband rejection (see Figure 3-3 b).

For upper sideband (USB) suppression, the IF signal is inserted in the "input" port of the IF hybrid; the "isolated" port is terminated by a 50 Ohm load. The IF 90° hybrid splits the phase of the incoming IF signal $s_{IF}(t) = A_{IF}\cos(\theta_{IF})$ and mixes it with the local oscillator $s_{LO}(t) = A_{LO}\cos(\theta_{LO})$. The RF signal in the "I", in-phase branch is derived:

$$s_{RF,I}(t) = \frac{A_{IF}A_{LO}}{\sqrt{2}}\cos(\theta_{IF})\cos(\theta_{LO}) \qquad (3\text{-}1)$$

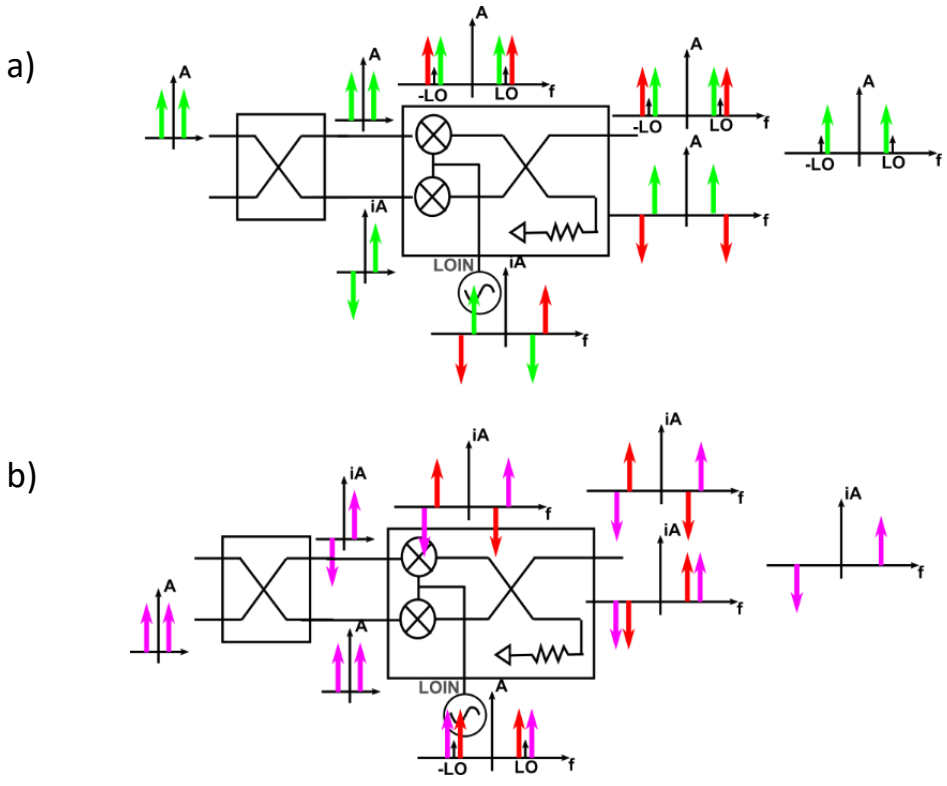

Figure 3-3: Illustration of modified Hartley architecture for a) LSB and b) USB up-conversion.
In the classic Hartley architecture, the phase of the LO and output signal is shifted [38],[39]. In the modified Hartley, the phase of the input and output signal is shifted.

$$s_{RF,I}(t) = \frac{A_{IF}A_{LO}}{2\sqrt{2}}(\cos(\theta_{IF} + \theta_{LO}) + \cos(\theta_{IF} - \theta_{LO})) \quad (3\text{-}2)$$

$$s_{RF,I}(t) = \frac{A_{IF}A_{LO}}{2\sqrt{2}}(\cos(\theta_{USB}) + \cos(\theta_{LSB})) \quad (3\text{-}3)$$

where $\theta_{USB} = \theta_{LO} + \theta_{IF}$ and $\theta_{LSB} = \theta_{LO} - \theta_{IF}$. The RF signal in the "Q" branch is:

$$s_{RF,Q}(t) = \frac{A_{IF}A_{LO}}{\sqrt{2}}\cos(\theta_{IF} - 90°)\cos(\theta_{LO}) \quad (3\text{-}4)$$

$$s_{RF,Q}(t) = \frac{A_{IF}A_{LO}}{\sqrt{2}}\sin(\theta_{IF})\cos(\theta_{LO}) \quad (3\text{-}5)$$

$$s_{RF,Q}(t) = \frac{A_{IF}A_{LO}}{2\sqrt{2}}(\sin(\theta_{IF} + \theta_{LO}) + \sin(\theta_{IF} - \theta_{LO})) \quad (3\text{-}6)$$

$$s_{RF,Q}(t) = \frac{A_{IF}A_{LO}}{2\sqrt{2}}(\sin(\theta_{USB}) - \sin(\theta_{LSB})) \quad (3\text{-}7)$$

The two RF outputs are then combined by the RF 90° hybrid coupler to provide the lower sideband.

$$s_{RF}(t) = \frac{A_{IF}A_{LO}}{2}(\cos(\theta_{USB}) + \cos(\theta_{LSB})) + \frac{A_{IF}A_{LO}}{2}(\sin(\theta_{USB} - 90°) - \sin(\theta_{LSB} - 90°)) \quad (3\text{-}8)$$

$$s_{RF}(t) = \frac{A_{IF}A_{LO}}{2}(\cos(\theta_{USB}) + \cos(\theta_{LSB})) + \frac{A_{IF}A_{LO}}{2}(-\cos(\theta_{USB}) + \cos(\theta_{LSB})) \quad (3\text{-}9)$$

$$s_{RF}(t) = A_{IF}A_{LO}\cos(\theta_{LSB}) \quad (3\text{-}10)$$

For lower sideband (LSB) suppression, the IF signal is inserted in the "isolated" port; the "input" port is terminated by a 50 Ohm load. The signal of the "Q", quadrature branch is now expressed:

$$s_{RF,I}(t) = \frac{A_{IF}A_{LO}}{\sqrt{2}}\cos(\theta_{IF} - 90°)\cos(\theta_{LO}) \quad (3\text{-}11)$$

$$s_{RF,I}(t) = \frac{A_{IF}A_{LO}}{2\sqrt{2}}(\sin(\theta_{USB}) - \sin(\theta_{LSB})) \quad (3\text{-}12)$$

And the signal in the "I", in-phase branch is written:

$$s_{RF,Q}(t) = \frac{A_{IF}A_{LO}}{\sqrt{2}}\cos(\theta_{IF})\cos(\theta_{LO}) \quad (3\text{-}13)$$

$$s_{RF,Q}(t) = \frac{A_{IF}A_{LO}}{2\sqrt{2}}(\cos(\theta_{USB}) + \cos(\theta_{LSB})) \quad (3\text{-}14)$$

The converter output provides the upper sideband as follows:

$$s_{RF}(t) = \frac{A_{IF}A_{LO}}{2}(\sin(\theta_{USB}) - \sin(\theta_{LSB})) + \frac{A_{IF}A_{LO}}{2}(\cos(\theta_{USB} - 90°) + \cos(\theta_{LSB} - 90°)) \quad (3\text{-}15)$$

$$s_{RF}(t) = \frac{A_{IF}A_{LO}}{2}(\sin(\theta_{USB}) - \sin(\theta_{LSB})) + \frac{A_{IF}A_{LO}}{2}(\sin(\theta_{USB}) + \sin(\theta_{LSB})) \quad (3\text{-}16)$$

$$s_{RF}(t) = A_{IF}A_{LO}\sin(\theta_{USB}) \quad (3\text{-}17)$$

In this configuration, either USB or LSB can be suppressed without the need of high-order bandpass filters. Note that by symmetry, if the RF 90° hybrid is terminated at its "I" port, the USB is obtained by applying the signal at the "input" port of the IF hybrid; the LSB is selected by applying the IF signal at the "isolated" port of the IF hybrid coupler.

In our radar prototype, we use the commercial upconverter TGC4546-SM from Qorvo, coupled with a 90° hybrid coupler IPP-7116 from Innovative Power Products and two baluns NCS1-112+ from Mini-Circuits. TGC4546-SM is only specified for its upper sideband conversion. Considering the manufacturer information in [21], the upper sideband is selected when the input signal arrives in phase on pins 9-10 and shifted by 90° on pins 11-12 of the surface-mounted device (SMD). By symmetry, we can select the lower sideband if the IF input signal is in-phase on pins 11-12 and delayed on pins 9-10. We place IPP-7116 [22] so as J3, in-phase, is linked to pins 11-12 and J4, delayed in-quadrature, is linked to 9-10. Thereby, we expect to select the lower sideband by applying the signal to J1 port and terminating J4 port.

3.4.2 Sideband suppression in down-conversion

Figure 3-4 shows the modified Hartley architecture for down-conversion and specifies the ports appellation of the commercial components used in our radar prototype, as described in [22]-[24]. The proposed architecture features an IQ down-converter HMC6789BLC5A from Analog Devices, two low-pass filters LFCN-1575 from Mini-Circuits and the 90° IF hybrid coupler IPP-7116. We want to demonstrate that this architecture can suppress either unwanted USB or LSB signal which would be demodulated into the target signal otherwise. Note that the demonstration is independent of the chosen components.

Let us consider a signal of intermediate frequency f_{IF} and a LO of frequency f_{LO}. Let us consider two input RF signals of frequency $f_{LSB} = f_{LO} - f_{IF}$ and $f_{USB} = f_{LO} + f_{IF}$, representing arbitrarily a carrier and a signal located at its image frequency. Without loss of generality, the RF signal is applied in the "input" port of the hybrid.

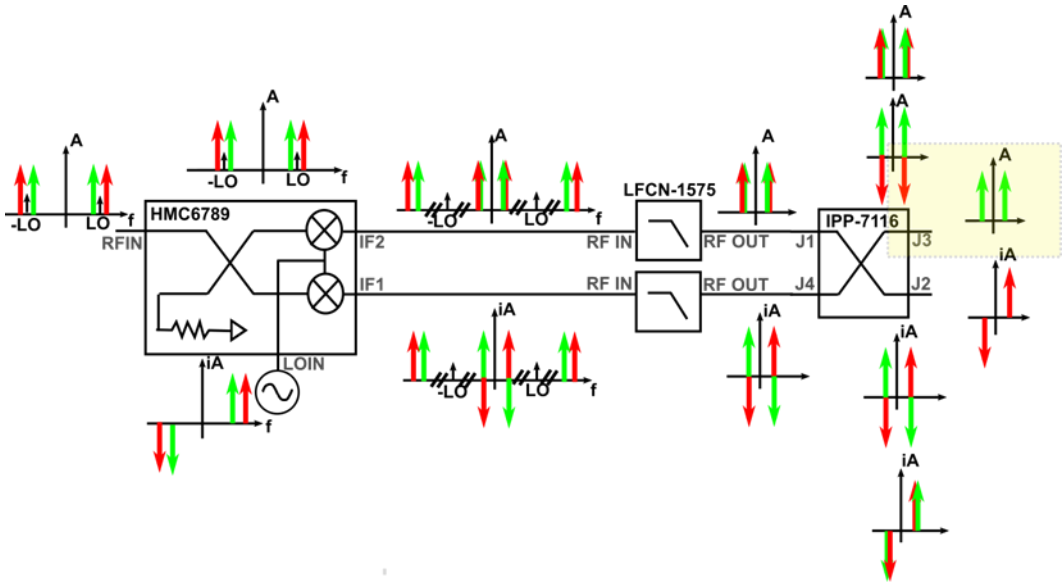

Figure 3-4: Modified Hartley architecture for single sideband down-conversion.
In green the carrier frequency and in red its image.

The RF input, "RFIN" can be written:

$$s(t) = A_{LSB}\cos(2\pi f_{LSB}t) + A_{USB}\cos(2\pi f_{USB}t) \quad (3\text{-}18)$$

$$s(t) = A_{LSB}\cos(\theta_{LSB}) + A_{USB}\cos(\theta_{USB}) \quad (3\text{-}19)$$

The input is divided into two signals of phase difference 90° by a 90° hybrid coupler:

$$s_{RF,I}(t) = \frac{A_{LSB}}{\sqrt{2}}\cos(\theta_{LSB}) + \frac{A_{USB}}{\sqrt{2}}\cos(\theta_{USB}) \quad (3\text{-}20)$$

$$s_{RF,Q}(t) = \frac{A_{LSB}}{\sqrt{2}}\cos(\theta_{LSB} - 90°) + \frac{A_{USB}}{\sqrt{2}}\cos(\theta_{USB} - 90°) \quad (3\text{-}21)$$

$$s_{RF,Q}(t) = \frac{A_{LSB}}{\sqrt{2}}\sin(\theta_{LSB}) + \frac{A_{USB}}{\sqrt{2}}\sin(\theta_{USB}) \quad (3\text{-}22)$$

Both signals on the in-phase and quadrature paths are multiplied by the LO signal "LOIN" for down-conversion. In the in-phase path "IF2" the signal becomes:

$$s_{RF,I}(t) = \frac{A_{LSB}}{\sqrt{2}}\cos(\theta_{LSB})\cos(\theta_{LO}) + \frac{A_{USB}}{\sqrt{2}}\cos(\theta_{USB})\cos(\theta_{LO}) \quad (3\text{-}23)$$

$$s_{RF,I}(t) = \frac{A_{LSB}}{2\sqrt{2}}[\cos(\theta_{LSB} + \theta_{LO}) + \cos(\theta_{LSB} - \theta_{LO})] + \frac{A_{USB}}{2\sqrt{2}}[\cos(\theta_{USB} + \theta_{LO}) + \cos(\theta_{USB} - \theta_{LO})] \quad (3\text{-}24)$$

$$s_{RF,I}(t) = \frac{A_{LSB}}{2\sqrt{2}}[\cos(2\theta_{LO} - \theta_{IF}) + \cos(-\theta_{IF})] + \frac{A_{USB}}{2\sqrt{2}}[\cos(2\theta_{LO} + \theta_{IF}) + \cos(\theta_{IF})] \quad (3\text{-}25)$$

$$s_{RF,I}(t) = \frac{A_{LSB}}{2\sqrt{2}}[\cos(2\theta_{LO} - \theta_{IF}) + \cos(\theta_{IF})] + \frac{A_{USB}}{2\sqrt{2}}[\cos(2\theta_{LO} + \theta_{IF}) + \cos(\theta_{IF})] \quad (3\text{-}26)$$

In the quadrature path "IF1" the signal becomes:

$$s_{RF,Q}(t) = \frac{A_{LSB}}{\sqrt{2}}\sin(\theta_{LSB})\cos(\theta_{LO}) + \frac{A_{USB}}{\sqrt{2}}\sin(\theta_{USB})\cos(\theta_{LO}) \quad (3\text{-}27)$$

$$s_{RF,Q}(t) = \frac{A_{LSB}}{2\sqrt{2}}[\sin(\theta_{LSB} + \theta_{LO}) + \sin(\theta_{LSB} - \theta_{LO})] + \frac{A_{USB}}{2\sqrt{2}}[\sin(\theta_{USB} + \theta_{LO}) + \sin(\theta_{USB} - \theta_{LO})] \quad (3\text{-}28)$$

$$s_{RF,Q}(t) = \frac{A_{LSB}}{2\sqrt{2}}[\sin(2\theta_{LO} - \theta_{IF}) + \sin(-\theta_{IF})] + \frac{A_{USB}}{2\sqrt{2}}[\sin(2\theta_{LO} + \theta_{IF}) + \sin(\theta_{IF})] \quad (3\text{-}29)$$

$$s_{RF,Q}(t) = \frac{A_{LSB}}{2\sqrt{2}}[\sin(2\theta_{LO} - \theta_{IF}) - \sin(\theta_{IF})] + \frac{A_{USB}}{2\sqrt{2}}[\sin(2\theta_{LO} + \theta_{IF}) + \sin(\theta_{IF})] \quad (3\text{-}30)$$

The high-frequency component of the signals is then filtered by a low-pass filter.

$$s_{IF,I}(t) = \frac{A_{LSB}}{2\sqrt{2}}\cos(\theta_{IF}) + \frac{A_{USB}}{2\sqrt{2}}\cos(\theta_{IF}) \quad (3\text{-}31)$$

$$s_{IF,Q}(t) = -\frac{A_{LSB}}{2\sqrt{2}}\sin(\theta_{IF}) + \frac{A_{USB}}{2\sqrt{2}}\sin(\theta_{IF}) \quad (3\text{-}32)$$

Finally, the signals are combined by a 90° hybrid. If the quadrature port of the coupler, in our case "J2" is terminated by 50 Ohm, meaning the in-phase path remains in phase and the quadrature path is delayed then the LSB is selected:

$$s_{IF}(t) = \frac{A_{LSB}}{2}\cos(\theta_{IF}) + \frac{A_{USB}}{2}\cos(\theta_{IF}) - \frac{A_{LSB}}{2}\sin(\theta_{IF} - 90°) + \frac{A_{USB}}{2}\sin(\theta_{IF} - 90°) \quad (3\text{-}33)$$

$$s_{IF}(t) = \frac{A_{LSB}}{2}\cos(\theta_{IF}) + \frac{A_{USB}}{2}\cos(\theta_{IF}) + \frac{A_{LSB}}{2}\cos(\theta_{IF}) - \frac{A_{USB}}{2}\cos(\theta_{IF}) \quad (3\text{-}34)$$

$$s_{IF}(t) = A_{LSB}\cos(\theta_{IF}) \quad (3\text{-}35)$$

If the in-phase port of the coupler, "J3" is terminated by 50 Ohm, meaning the in-phase path is delayed and the quadrature path remains in phase then the USB is selected:

$$s_{IF}(t) = \frac{A_{LSB}}{2}\cos(\theta_{IF} - 90°) + \frac{A_{USB}}{2}\cos(\theta_{IF} - 90°) - \frac{A_{LSB}}{2}\sin(\theta_{IF}) + \frac{A_{USB}}{2}\sin(\theta_{IF}) \quad (3\text{-}36)$$

$$s_{IF}(t) = \frac{A_{LSB}}{2}\sin(\theta_{IF}) + \frac{A_{USB}}{2}\sin(\theta_{IF}) - \frac{A_{LSB}}{2}\sin(\theta_{IF}) + \frac{A_{USB}}{2}\sin(\theta_{IF}) \quad (3\text{-}37)$$

$$s_{IF}(t) = A_{USB}\sin(\theta_{IF}) \quad (3\text{-}38)$$

Using the modified Hartley architecture for down-conversion does not require any high-order bandpass filter for image cancellation. By symmetry, if the RF 90° hybrid was terminated at its "isolated" port, the USB would be obtained terminating the "I" port of the hybrid, and the LSB by terminated the "Q" port of the hybrid.

3.5 Second-order harmonic cancellation: enhanced push-pull architecture

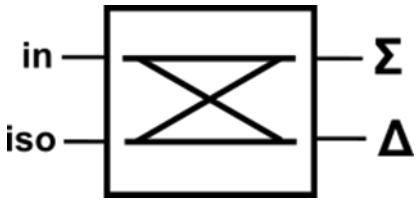

Figure 3-5: 180° hybrid coupler symbol

In this sub-section, we demonstrate the possibility of cancelling the second harmonic distortion with the push-pull amplifier architecture [40],[41]. Figure 3-5 recalls the symbol of a 180° hybrid coupler and Figure 3-6 depicts the push-pull architecture. The architecture comprises two power amplifiers placed in parallel. One of the paths of the push-pull structure is phase shifted by 180° at the input and at the output of the amplifier. Both paths are then combined. The phase shifting between the signals is typically performed by baluns or 180° hybrids. The demonstration is conducted at the system level, using an ideal coupler operating down to DC.

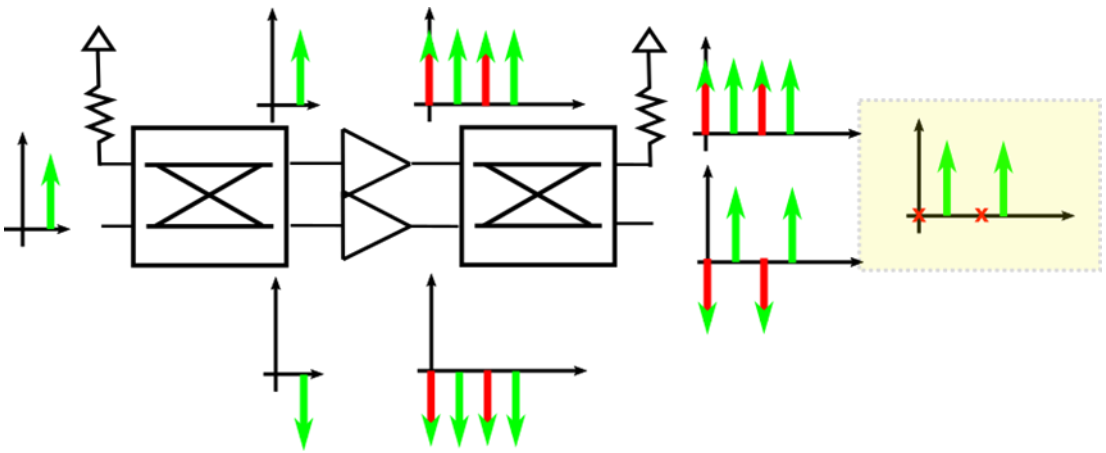

Figure 3-6: Push pull amplifier architecture including harmonic behaviour.

3.5.1 Second-order harmonic cancellation

Considering up to the third order distortion, the output signal of an amplifier $y(t)$ can be written for any input $x(t)$:

$$y(t) = A_1 x(t) + A_2 x^2(t) + A_3 x^3(t) \quad (3\text{-}39)$$

If the input of the hybrid is $s_{in}(t) = A_{in}\cos\big(\theta(t)\big)$, the outputs of a 180° hybrid are:

$$s_{0°,1}(t) = \frac{A_{in}}{\sqrt{2}}\cos\big(\theta(t)\big) \quad (3\text{-}40)$$

$$s_{180°,1}(t) = \frac{A_{in}}{\sqrt{2}}\cos(\theta(t) - 180°) = -\frac{A_{in}}{\sqrt{2}}\cos\big(\theta(t)\big) \quad (3\text{-}41)$$

where $\frac{1}{\sqrt{2}}$ represents the voltage division by the hybrid.

At the output of the amplifiers, the signal in the in-phase path can be expressed:

$$s_{0°,2}(t) = A_1\left(\frac{A_{in}}{\sqrt{2}}\cos\big(\theta(t)\big)\right) + A_2\left(\frac{A_{in}}{\sqrt{2}}\cos\big(\theta(t)\big)\right)^2 + A_3\left(\frac{A_{in}}{\sqrt{2}}\cos\big(\theta(t)\big)\right)^3 \quad (3\text{-}42)$$

$$s_{0°,2}(t) = A_1\frac{A_{in}}{\sqrt{2}}\cos\big(\theta(t)\big) + A_2\frac{{A_{in}}^2}{2}\frac{1+\cos\big(2\theta(t)\big)}{2} + A_3\frac{{A_{in}}^3}{2\sqrt{2}}\frac{3\cos\big(\theta(t)\big)+\cos\big(3\theta(t)\big)}{2} \quad (3\text{-}43)$$

$$s_{0°,2}(t) = A_2\frac{{A_{in}}^2}{4} + \left(A_1\frac{A_{in}}{\sqrt{2}} + A_3\frac{3{A_{in}}^3}{4\sqrt{2}}\right)\cos\big(\theta(t)\big) + A_2\frac{{A_{in}}^2}{4}\cos\big(2\theta(t)\big) + A_3\frac{{A_{in}}^3}{4\sqrt{2}}\cos\big(3\theta(t)\big) \quad (3\text{-}44)$$

The signal is now a function of the first and third harmonic distortion.

Likewise, the signal is the out-of-phase path writes:

$$s_{180°,2}(t) = -A_1\frac{A_{in}}{\sqrt{2}}\cos\big(\theta(t)\big) + A_2\left(\frac{A_{in}}{\sqrt{2}}\cos\big(\theta(t)\big)\right)^2 - A_3\left(\frac{A_{in}}{\sqrt{2}}\cos\big(\theta(t)\big)\right)^3 \quad (3\text{-}45)$$

$$s_{180°,2}(t) = A_2\frac{{A_{in}}^2}{4} - \left(A_1\frac{A_{in}}{\sqrt{2}} + A_3\frac{3{A_{in}}^3}{4\sqrt{2}}\right)\cos\big(\theta(t)\big) + A_2\frac{{A_{in}}^2}{4}\cos\big(2\theta(t)\big) - A_3\frac{{A_{in}}^3}{4\sqrt{2}}\cos\big(3\theta(t)\big) \quad (3\text{-}46)$$

The signal in the out-of-phase path is delayed by 180° again by the hybrid, then both signals are summed up:

$$s_{out}(t) = \frac{1}{\sqrt{2}}s_{0°,2}(t) + \frac{1}{\sqrt{2}}s_{180°,2}(t - \tau_{-180°}) \quad (3\text{-}47)$$

Where the factor $\frac{1}{\sqrt{2}}$ accounts for the 3-dB split.

$$s_{out}(t) = \frac{1}{\sqrt{2}}\left[A_2\frac{{A_{in}}^2}{4} + \left(A_1\frac{A_{in}}{\sqrt{2}} + A_3\frac{3{A_{in}}^3}{4\sqrt{2}}\right)\cos\big(\theta(t)\big) + A_2\frac{{A_{in}}^2}{4}\cos\big(2\theta(t)\big) + A_3\frac{{A_{in}}^3}{4\sqrt{2}}\cos\big(3\theta(t)\big)\right]$$
$$+\frac{1}{\sqrt{2}}\left[A_2\frac{{A_{in}}^2}{4}\cos\left(-180°\right) - \left(A_1\frac{A_{in}}{\sqrt{2}} + A_3\frac{3{A_{in}}^3}{4\sqrt{2}}\right)\cos(\theta(t) - 180°) + A_2\frac{{A_{in}}^2}{4}\cos(2\theta(t) - 180°) - A_3\frac{{A_{in}}^3}{4\sqrt{2}}\cos(3\theta(t) - 180°)\right] \quad (3\text{-}48)$$

This means:

$$s_{out}(t) = \frac{1}{\sqrt{2}}\left[A_2\frac{{A_{in}}^2}{4} + \left(A_1\frac{A_{in}}{\sqrt{2}} + A_3\frac{3{A_{in}}^3}{4\sqrt{2}}\right)\cos\big(\theta(t)\big) + A_2\frac{{A_{in}}^2}{4}\cos\big(2\theta(t)\big) + A_3\frac{{A_{in}}^3}{4\sqrt{2}}\cos\big(3\theta(t)\big)\right]$$
$$+\frac{1}{\sqrt{2}}\left[-A_2\frac{{A_{in}}^2}{4} + \left(A_1\frac{A_{in}}{\sqrt{2}} + A_3\frac{3{A_{in}}^3}{4\sqrt{2}}\right)\cos\big(\theta(t)\big) - A_2\frac{{A_{in}}^2}{4}\cos\big(2\theta(t)\big) + A_3\frac{{A_{in}}^3}{4\sqrt{2}}\cos\big(3\theta(t)\big)\right] \quad (3\text{-}49)$$

$$s_{out}(t) = \frac{2}{\sqrt{2}}\left(A_1\frac{A_{in}}{\sqrt{2}} + A_3\frac{3{A_{in}}^3}{4\sqrt{2}}\right)\cos\big(\theta(t)\big) + \frac{2}{\sqrt{2}}\frac{{A_{in}}^3}{4\sqrt{2}}\cos\big(3\theta(t)\big) \quad (3\text{-}50)$$

Hence:

$$s_{out}(t) = \left(A_1A_{in} + A_3\frac{3{A_{in}}^3}{4}\right)\cos\big(\theta(t)\big) + \frac{{A_{in}}^3}{4}\cos\big(3\theta(t)\big) \quad (3\text{-}51)$$

The signal at the output of the push-pull is a function of odd-order harmonics, here the fundamental and the third-order harmonic.

Note that the second phase shift can occur in the in-phase path or in the out-of-phase path of the push-pull amplifier. The output signal is then shifted by 180°.

A DC signal of amplitude A shifted by 180° becomes a DC signal of amplitude -A, hence the cos(-180°) in Equation (3-48). Note that on a system level, the DC harmonic is suppressed only if the coupler operates down to DC.

The demonstration was conducted for a single-tone input signal. If a multi-tone signal is applied to the push-pull architecture, all second-order harmonic distortion will be cancelled out [40],[41].

3.5.2 Gain of push-pull architecture

The gain of the push-pull amplifier is:

$$\text{Gain} = \frac{A_1 A_{in} + A_3 \frac{3A_{in}{}^3}{4}}{A_{in}} = A_1 + A_3 \frac{3A_{in}{}^2}{4} \quad (3\text{-}52)$$

This gain corresponds to the gain of a single amplifier. The gain depends also on the third harmonic distortion. There is a possibility to double the output power with the push-pull architecture when the amplifiers operate in saturation [41]. The signals in both paths will be amplified to a maximum output power, and then summed by the hybrid which gives a gain of 3 dB in comparison to a single amplifier operating in saturation.

3.5.3 Impact of gain and phase imbalance and insertion loss of the hybrid

The performance of a push-pull amplification strongly depends on the design quality of a phase shifters or 180° hybrids. The signals in the in-phase and out-of-phase paths should be correctly split in order to have the same amplitude and be shifted by 180°. If the signals in the different paths do not feature an exact shift of 180° or are of different amplitude, we can see from the previous derivation that the second-order harmonic will not be entirely cancelled, and the push-pull gain will not be maximal.

Achieving a good amplitude and phase balance at millimetre-wave frequency can be challenging. Some commercial components can propose 180° hybrids with a gain imbalance as large as 2 dB, and a phase imbalance as large a 12°. A way to restore the gain balance between the two paths of the push-pull architecture is to add an attenuator the path with the larger signal. In practice, because power is usually a scarce resource, it is preferable to control the gain of one of the amplifiers so that it is smaller in the larger signal path. It is trickier to add a phase corrector to restore the phase balance between two paths. A solution is to perform the phase shifting in both paths so as to have the same imbalance in both paths. This solution is not ideal as it does not restore the 180° phase difference required at specific positions to allow the good second-order harmonics cancellation.

Another limiting factor is the insertion loss of the output hybrid. The output power can be doubled given that the hybrid is ideal and loss-less. Therefore, the push-pull amplifier architecture can provide an additional gain only if the output hybrid has a loss inferior to 3 dB. The input hybrid loss is less critical, as the power amplifiers will be driven to saturation.

3.6 Link budget and receiver design characterization

The link budget is a design tool which allows to anticipate the receiver system performance such as the receiver gain, noise figure or sensitivity, and to implement its circuit accordingly without over designing it at extra cost. More particularly in our case, the link budget helps to determine the number of IF amplification stages which can safely be added to the receiver

without distortion of the signal (cf. Figure 3-1). We select the adequate and available SMT components at 35 GHz. Based on their specs and power constrains, we evaluate the link quality and determine the expected receiver performance before post-processing.

3.6.1 Link budget

We recall the radar link budget equation for a bi-static radar of transmitted power P_t, transmitting antenna gain G_t, receiving antenna gain G_r, transmitted wavelength λ, and radar cross section σ and F the pattern propagation factor. The received power is [2]:

$$P_r = \frac{P_t G_t G_r \lambda^2 \sigma F^4}{(4\pi)^3 {R_t}^2 {R_r}^2} \quad (3\text{-}53)$$

R_t is the distance between the transmitter and the target, and R_r the distance between the target and the receiver.

The propagation factor F depends on the environment and accounts for multipath and shadowing. F = 1 in vacuum without interference: we will use this assumption for the demonstration. Our radar application for wind turbine structural health monitoring aims to detect defects on a blade, with a typical radar cross section (RCS) of 1 dm² at 10 m, or to detect bats or birds in the vicinity of the turbine, corresponding to a RCS of 1 cm² at 100 m. Table 3-2 shows the derivation of the link budget for a blade at 10 m of RCS 1 dm².

3.6.2 Range equation

The radar equation for a monostatic radar of antenna gain $G = G_t = G_r$ and range $R = R_t = R_r$ can be rewritten:

$$R = \sqrt[4]{\frac{P_t G^2 \lambda^2 \sigma}{P_r (4\pi)^3}} \quad (3\text{-}54)$$

From this equation, can be deducted the minimum and maximum range depending on the maximum and minimum receivable power respectively.

3.6.3 Range resolution

The radar range resolution is inversely proportional to the operating bandwidth B and is:

$$S_r = c/2B \quad (3\text{-}55)$$

c being the celerity of light. For a 1.05 GHz bandwidth radar, the range resolution is therefore 14.3 cm which is appropriate for wind turbine structural health monitoring application.

Table 3-2: Radar link budget

CONSTANTS	Values	Units	Equations
speed of light (c)	3.00E+08	m/s	
Boltzmann constant (k)	1.38E-23	$m^2\ kg\ s^{-2}\ K^{-1}$	
GENERAL PARAMETERS	**Values**	**Units**	**Equations**
power spectral density (PSD)	18.24	dBm/MHz	100W EIRP
DDS (fmin)	2.00E+08	Hz	0.20 GHz
DDS (fmax)	1.25E+09	Hz	1.25 GHz
LO	3.60E+10	Hz	36 GHz
bandwidth (B)	1.05E+09	Hz	fmax-fmin
center frequency (fc)	3.53E+10	Hz	36 - (fmin+fmax)/2
image	3.67E+10	Hz	36 + (fmin+fmax)/2
wavelength (lambda)	8.50E-03	m	c/fc
temperature	2.00E+01	°C	20°C
temperature (T)	2.93E+02	K	T + 273.15
pulse width (Tp)	5.00E-04		500 us
time resolution (Tchip)	9.52E-10		1/B
code length (Nc)	1.27E+02	bits	
symbol rate (Rb)	2.54E+05	bps	Nc/Tp
TX SYSTEM PARAMETERS	**Values**	**Units**	**Equations**
transmitted power (Pt)	35	dBm	
Pt in Watts	3.16227766	W	10^(Pt/10-3)
TX antenna gain (Gt)	15	dBi	
Gt, linear	31.6227766		10^(Gt/10)
TX losses (Lt)	0.00E+00	dB	
Lt, linear	1.00E+00		10^(Lt/10)
effective isotropic radiated power (EIRP)	5.00E+01	dBm	Pt+Gt-Lt
EIRP in Watts	1.00E+02	Watts	10^((EIRP-30)/10)
maximum TX power	1.38E+02	dBm	PSD+10*log10(B in MHz)
PATH PARAMETERS	**Values**	**Units**	**Equations**
path loss exponent (n)	2		
distance TX to target (d1)	10	m	
distance target to RX (d2)	10	m	
path loss @1m (PL0)	6.34E+01	dB	10*n*log10(4*pi*f/c)
path loss @TX-target (PL1)	20	dB	10*n*log10(d1)
RCS	0.01	m^2	1 dm^2
path loss @target-RX (PL2)	20	dB	10*n*log10(d2)
coefficient of reflexivity (alpha)	1737.40633		RCS*(4pi)^(2n-3)*d1^(n-2)*d2^(n-2)/lambda^(2*(n-1))
path loss RCS (PLrcs)	3.24E+01	dB	10*log10(alpha)
lognormal shadowing standard deviation	0	dB	
worse case shadowing loss	0	dB	
total path loss (PL)	1.34E+02	dB	2*PL0+PL1+PL2-PLrcs
RX SYSTEM PARAMETERS	**Values**	**Units**	**Equations**
RX antenna gain (Gr)	15	dBi	
Gr, linear	31.6227766		10^(Gr/10)
RX losses (Lr)	0	dB	
Lr,linear	1.00E+00		10^(Lr/10)
received power (Pr)	**-6.94E+01**	dBm	Pt+Gt+Gr-PL-LR
Pr in Watts	1.15E-10	W	10^(Pr/10-3)
thermal noise (PNth)	-8.37E+01	dBm	10*log10(kBT)+30
input signal-to-noise ratio (SNRi)	1.43E+01	dB	Pr-PNth
RECEIVER SENSITIVITY PARAMETERS	**Values**	**Units**	**Equations**
RX noise factor (F)	4.241741465		Friis
RX noise figure (NF)	6.275441946	dB	10*log10(F)
RX noise floor (PN)	-7.74E+01	dBm	PNth+NF
output signal-to-noise ratio (SNRo)	8.06E+00	dB	SNRi-NF
minimum required output SNR (SNRo,min)	15	dB	
sensitivity (Pr,min)	**-6.24E+01**	dBm	SNRo,min + PNth + NF
Pr,min in Watts	**5.70E-10**	Watts	10^(Pr,min/10-3)
link margin (LM)	**-6.94E+00**	dB	SNRo - SNRo,min
maximum achievable radar range before Gint	**6.71E+00**	m	((Pt*Gt*Gr*lambda^2*RCS)/((4pi)^3*Pr,min*loss))^(1/4)

Table 3-3: Power and Noise Budget

Description	Part Number	Gain (dB)	Noise Figure (dB)	Power Budget (dBm)	Noise Budget (dBm)
2.4 connector	1492-04A-6	-3	+3	P_r-3	N_{in}+3
				(P_r)	(N_{in})
LNA (RF)	CHA2494-QEG	+22	+3.2	P_r +19	N_{in}+6.2
				(P_r +22)	(N_{in}+3.2)
Attenuator	CHT4694-QAG	-5	+5	P_r +14	N_{in}+6.23
				(P_r +17)	(N_{in}+3.23)
LNA (RF)	CHA2494-QEG	+22	+3.2	P_r +36	N_{in}+6.27
				(P_r +39)	(N_{in}+3.27)
Attenuator	CHT4694-QAG	-5	+5	P_r +31	N_{in}+6.27
				(P_r +34)	(N_{in}+3.27)
I/Q D-Conv	HMC6789BLC5A	+8	+3.5	P_r +39	N_{in}+6.28
				(P_r +42)	(N_{in}+3.28)
LPF	LFCN-1575+	-1	+1	P_r +38	N_{in}+6.28
				(P_r +41)	(N_{in}+3.28)
90° hybrid	IPP-7116	-1	+1	P_r +37	N_{in}+6.28
				(P_r +40)	(N_{in}+3.28)
Deramp Mixer	ADE-R5LH+	-9.5	+10.5	**P_r +27.5**	**N_{in}+6.28**
				(P_r +30.5)	**(N_{in}+3.28)**
1-stage IF amplification:					
LNA (IF)	HMC8410LP2FE	+19	+1.6	P_r +56	N_{in}+6.28
				(P_r +59)	(N_{in}+3.28)
LPF	LFCN-1575+	-1	+1	P_r +55	N_{in}+6.28
				(P_r +58)	(N_{in}+3.28)
HPF	RHP-65+	-0.5	+0.5	P_r +54.5	N_{in}+6.28
				(P_r +57.5)	(N_{in}+3.28)
Deramp Mixer	ADE-R5LH+	-9.5	+10.5	**P_r +45**	**N_{in}+6.28**
				(P_r +48)	**(N_{in}+3.28)**
2-stage IF amplification:					
LNA (IF)	HMC8410LP2FE	+19	+1.6	P_r +73.5	N_{in}+6.28
				(P_r +76.5)	(N_{in}+3.28)
LPF	LFCN-1575+	-1	+1	P_r +72.5	N_{in}+6.28
				(P_r +75.5)	(N_{in}+3.28)
HPF	RHP-65+	-0.5	+0.5	P_r +72	N_{in}+6.28
				(P_r +75)	(N_{in}+3.28)
Deramp Mixer	ADE-R5LH+	-9.5	+10.5	**P_r +62.5**	**N_{in}+6.28**
				(P_r +65.5)	**(N_{in}+3.28)**

3-stage IF amplification:					
LNA (IF)	HMC8410LP2FE	+19	+1.6	P_r +91	N_{in}+6.28
				(P_r +94)	(N_{in}+3.28)
LPF	LFCN-1575+	-1	+1	P_r +90	N_{in}+6.28
				(P_r +93)	(N_{in}+3.28)
HPF	RHP-65+	-0.5	+0.5	P_r +89.5	N_{in}+6.28
				(P_r +92.5)	(N_{in}+3.28)
Deramp Mixer	ADE-R5LH+	-9.5	+10.5	**P_r +80**	**N_{in}+6.28**
				(P_r +83)	**(N_{in}+3.28)**

The table displays the expected cumulative power and noise budget for the receiver including the RF connector. In brackets, the expected cumulative power and noise budget for the receiver only, without considering the input connector. Noise figures were calculated according to Friis formula [42]. Including the connector is especially useful to anticipate receiver characterization. The loss generated by the connector can also account for the transition antenna to amplifier input which is generally very lossy.

3.6.4 Power and Noise budget

The power budget and the noise budget are calculated in Table 3-3 in their worst-case scenario, for arbitrary received power P_r and input noise N_{in} respectively, where the minimum gain and maximum noise figure of the components are considered. The worst-case scenario parameters will account for miscellaneous loss such as integration, mismatching, transmit line and receive line losses. The budget table, where P_r is the received power (see equation (3-53)) and $N_{in}=kBT$ the receiver input noise floor proportional to the Boltzmann constant k, the bandwidth B and the temperature T, details the cumulative gain and noise figure at each stage of the receiver chain. Thereby, the maximum receivable power, $P_{r,max}$ can easily be calculated.

The performance of the receiver strongly depends on the first stage. The expected receiver noise figure is 3.28 dB. The expected receiver gain is 30.5 dB, 48 dB, 65.5 dB and 83 dB for zero, one, two and three-stage IF amplification respectively. The RF connector can impact the performance of the receiver during its characterization. If the connector is considered the first stage in its worst-case scenario, then the expected gain of the receiver during measurements becomes 27.5 dB, 45 dB, 62.5 dB and 80 dB respectively. The anticipated noise figure becomes 6.28 dB.

3.6.5 Power constraints

To guarantee the best performance of each component and therefore of the receiver board, the maximum input power of each component in the receiver chain must be carefully considered. Not respecting these power constraints could cause the devices to either saturate and under-

perform, or even break in the worst-case scenario. More specifically, at IF frequency, the signal is significantly amplified. One amplification stage is composed of an IF low-noise amplifier (LNA) followed by a low-pass filter and a high-pass filter (cf. Figure 3-1) and we repeat the amplification up to three times for very low-power input signals: if the received power of the receiver is too high, the power at the input of the deramp mixer can be too high.

The maximum ratings of the RF LNA, the RF attenuators, the downconverter, the IF LNA and the mixer are listed in Table 3-4. Considering the maximum ratings of those devices, the number of IF amplification stages should be adapted in accordance with the received power to avoid the deramp mixer from overloading. The maximum input power before the receiver overloads is called the maximum receivable power, $P_{r,max}$ and depends on the maximum ratings and the receiver gain.

Table 3-4: Maximum ratings.

Description	Part Number	$P_{in,max}$
LNA (RF)	CHA2494-QEG	+10 dBm
Attenuator	CHT4694-QAG	+30 dBm
I/Q Downconverter	HMC6789BLC5A	+8 dBm
LNA (IF)	HMC8410LP2FE	+20 dBm
Mixer	ADE-R5LH+	+16 dBm

Values taken from manufacturers datasheets.

3.6.6 Maximum receivable power

From the power budget and considering the power constraints, we can deduct the maximum input power before the receiver overloads:

$$P_{r,max} = \min_{\text{stage } i}\left\{P_{in,max,i} - G_{cum,i-1}\right\} \quad (3\text{-}56)$$

Where $P_{in,max,i}$ is the maximum input power of stage i and $G_{cum,i}$ is the cumulative gain of stage i. The RF connector is included to anticipate and protect the receiver module during measurements. Without any amplification stage, $P_{r,max}$ is limited by the I/Q down-converter and is -23 dBm. With one amplification stage, it is limited by the deramp mixer and is -38.5 dBm. With two amplification stages it is limited by the deramp mixer and is -56 dBm. Finally, with three amplification stages, the maximum receivable power is limited by the deramp mixer and is -73.5 dBm. For wind turbine structural health monitoring application, the maximum transmitted power is 35 dBm when the antenna gains are 15 dB (100 W EIRP). The radar cross section is 1 dm² when looking at the turbine blades. This corresponds to a minimum achievable range of 0.69 m, 1.69 m, 4.63 m and 12.7 m respectively at 35.3 GHz. The RCS is 1 cm² when looking at bats. This

corresponds to a minimum achievable range of 0.22 m, 0.53 m, 1.46 m and 4.01 m respectively. Below these ranges, the input signal is too strong and the receiver can underperform, or even be damaged. These are plausible values for blade damage monitoring, as the typical distance between the wind turbine tower (on which the radar will be located) and its blade is 10 m, as well as for bats and birds detection as the bat should be detected at even larger distances.

3.6.7 Minimum receivable power or Sensitivity level

We define the receiver sensitivity as the minimum receivable power to detect and process the signal. The receiver sensitivity can be calculated:

$$P_{r,min} = SNR_{o,min} \cdot kBT \cdot NF \quad (3\text{-}57)$$

Where $SNR_{o,min}$ is the minimum receiver output signal-to-noise ratio required to process the signal, k = 1.38×10^{-23} J/K Boltzmann's Constant, T temperature of the receiver input, B the receiver bandwidth and NF the noise figure. $SNR_{o,min}$ depends on the intended use of the system. In radar application, it is typically 15 dB. For a 1.05 GHz-bandwidth, at room temperature 20°C (293 K), $P_{r,min}$ equals -62.4 dBm including the RF connector, and -65.4 dBm when considering the receiver only. Considering the connectors, this corresponds to a maximum range of 6.69 m when RCS is 1 dm², and 2.12 m when RCS is 1cm². Without connector, the maximum range is 7.95 m when RCS 1 dm² or 2.51 m for a RCS of 1 cm², without post-processing for a 100W EIRP emission. Above these ranges, the input signal is too low and the receiver cannot process the signal without post-processing. The maximum ranges can be increased by emitting more power.

In the case of a 3-stage IF amplification, $P_{r,min}$ is larger than $P_{r,max}$ therefore the receiver as it is cannot process the radar signal without post-processing.

3.6.8 Minimum discernible power

The minimum discernible power, sometimes referred as MDS for minimum discernible signal, is the minimum receiver input power required to only detect the signal.

$$MDS = SNR_{o,detection} \cdot kBT \cdot NF \quad (3\text{-}58)$$

Where $SNR_{o,detection}$ is the minimum receiver output signal-to-noise ratio required to detect the signal. In radar applications, it is commonly 3 dB. This corresponds to a MDS of -74.4 dBm or -77.4 dBm with or without connectors, and a range of including the connectors of 13.3 m for a 1dm² RCS, and 4.22 m for a 1 cm² RCS, and without connector of 15.9 m and 5.02 m respectively. Note that MDS is smaller than $P_{r,max}$: the receiver will be able to detect the signal without post-processing for a range between the minimum and maximum range.

3.6.9 Dynamic range

The receiver dynamic range *D* is the ratio between maximum receivable power and the minimum discernible power:

$$D = \frac{P_{r,max}}{MDS} \quad (3\text{-}59)$$

Depending on the increasing amount of IF amplification, the receiver dynamic range is 54.4 dB, 38.9 dB, 21.4 dB, and 3.9 dB, for none up to three stages of IF amplification, considering the receiver only. The dynamic range is 3 dB lower with the connectors.

3.6.10 To go further

3.6.10.1 Post-processing gain

The link budget study shows that the proposed radar will be able to detect but not to process the signal without any post processing. This is typical for high-resolution radar application where the receiver input signal to noise ratio is very low due to the large signal bandwidth leading to large input noise floor. The receiver sensitivity can be improved by performing a pulse integration and obtaining thereby a post processing gain.

3.6.10.2 Variable gain amplification before demodulation

The required input power to operate the analog-to-digital converter (ADC) is also a limitation of the system. Assuming a sinusoidal signal and a reference impedance *R*, it can be expressed:

$$P_{ADC} = VI = \frac{V^2}{R} = \frac{{V_{pp,ADC}}^2}{8R} \quad (3\text{-}60)$$

Where $V_{pp,ADC}$ is the peak-to-peak input voltage required by the ADC and $V = V_p/\sqrt{2} = V_{pp}/2\sqrt{2}$. $V_{pp,ADC}$ is typically 0.8 Vpp, with {$V_{pp,ADC,min}$, $V_{pp,ADC,max}$} = {0.4, 2 Vpp} [43], which means typically P_{ADC} = 2 dBm with a 50-Ohm reference, with {$P_{ADC,min}$, $P_{ADC,max}$ } = {-4, 10 dBm}. We saw in the previous sections that the critical component for system linearity is the deramp mixer which input power cannot be larger than 16 dBm. This means an output power no larger than 6.5 dBm. Therefore, no attenuator will be necessary between the mixer and the ADC to keep the signal below the maximum input power of the ADC. A variable gain amplifier can be of use to level low power signals up to the required P_{ADC} = 2 dBm: according to the link budget, for receiver input power lower than -81 dBm without connector, -78 dBm with connectors for a 3 stage-IF amplification. Note that the VGA being the very last stage will not have a significant impact on the noise figure, and therefore on the receiver sensitivity.

3.7 Summary and remarks

In this Chapter, we designed the radar architecture and presented an extensive system analysis of the proposed architecture.

We proposed a radar architecture based on commercial components to suppress the image sideband without the use of high-order bandpass filters. This architecture is a modified version of the Hartley architecture and features an IQ mixer with a 90° IF hybrid coupler, as well as two low-order LPF in the down-conversion configuration. The architecture is well adapted to radar implementation using either commercial components or self-designed technology. Some components of the radar perform outside the specs of the datasheet because at the time of development, no other components were available within the desired bandwidth. Considering these restrictions, the specs of upconverter TGC4546-SM used in the Tx module and the specs of the LO drive chain, we will choose the lower sideband conversion for our radar development.

We proposed an enhanced push-pull architecture to cancel the second-order harmonics generated by power amplifiers. The architecture features two PAs in parallel and two 180° hybrid couplers. To limit the amplitude and phase imbalance created by the couplers, we control the gain of the amplifier in one of the paths, and we shift the phase by 180° in both paths. We operate the power amplifiers in saturation, to double the output power in comparison to using one single PA. The proposed architecture does not necessitate high-order bandpass filter to cancel the second-order harmonics and is therefore highly integrable. The proposed architecture requires a careful design of the output 180° hybrid to maximise the 3 dB gain. Note that the third harmonic is usually very far from the carrier frequency. Thus, we can expect that it does not require high-order bandpass filters to be suppressed.

Finally, we computed the expected performance of the proposed receiver module before post-processing. A single or no-IF amplification stage is needed for blade damage monitoring and two to three-stage amplification is preferable for bats detection. In this configuration, the receiver should not overload. Table 3-5 summarizes the expected system performance of the proposed receiver architecture. The results before post-processing are satisfactory because the SNR is large enough for a good signal detection. It will be preferable to integrate the signal nevertheless: the generated processing gain will increase the maximum range of the radar and allow an effective signal demodulation. Especially in the case of 3-stage IF amplification, where the receiver cannot process the radar signal without post-processing.

Note that the sensitivity of the receiver can be improved by sending a narrow band signal. However, this means that the receiver noise will be reduced at the cost of range resolution, which

Table 3-5: Summary of expected Rx performance

Parameters	**(0)**	**(1)**	**(2)**	**(3)**
$P_{r\ @10\ m,\ \sigma=1dm^2}$ (dBm)	-69.4	-69.4	-69.4	-69.4
$P_{r\ @100\ m,\ \sigma=1cm^2}$ (dBm)	-129	-129	-129	-129
G (dB)	27.5	45	62.5	80
NF (dB)	6.28	6.28	6.28	6.28
$P_{r,max}$ (dBm)	-23	-38.5	-56	-73.5
$R_{min\ \sigma=\ 1dm^2}$ (m)	0.69	1.69	4.63	12.7
$R_{min\ \sigma=\ 1cm^2}$ (m)	0.22	0.53	1.49	4.01
$P_{r,min}$ (dBm)	-62.4	-62.4	-62.4	-62.4
$R_{max\ \sigma=1dm^2}$ (m)	6.69	6.69	6.69	6.69
$R_{max\ \sigma=1cm^2}$ (m)	2.12	2.12	2.12	2.12
MDS (dBm)	-74.4	-74.4	-74.4	-74.4
$R_{MDS\ \sigma=1dm^2}$ (m)	13.3	13.3	13.3	13.3
$R_{MDS\ \sigma=1cm^2}$ (m)	4.22	4.22	4.22	4.22
D (dB)	51.4	35.9	18.4	0.9
Resolution (m)	0.14	0.14	0.14	0.14

The expected performance is summarized for (0) zero, (1) one, (2) two and (3) three IF amplification stages. The input RF connector is taken into account, since the radar hardware is to be developed and characterized for the purpose of system validation.

is not relevant for imaging application. The link performance will thereby be improved by increasing the transmitted power or performing post-processing integration.

In the next Chapter, we investigate the software implementation of the proposed architecture in the SISO case using computer-aided design (CAD) tool.

Chapter 4

Detailed system simulation of the SISO architecture

In this Chapter, we present the development of a radar simulation environment emulating realistic device performance. The antenna and the wave propagation to the target is based on an innovative 3D electromagnetic propagation model. We implement the system validation of the proposed SISO radar architecture.

4.1 Simulation method

Systems CAD tools such as Keysight ADS are a relevant way to test the feasibility of a system prior to fabrication and necessary. However, they usually use low-level system models which do not take into account system reality. In order to guarantee close-to-reality simulations, we model each component of the radar front-end using performance parameters from existing commercial devices. In addition, we include a realistic and novel propagation model, comprising the antennas and the full 3D EM propagation simulation to and from the scattering object. This approach enables the prediction of realistic signals received by the radar, as well as a more pertinent conjecture of the image quality and resolution.

4.1.1 Front-end model

We can achieve frequency dependent characteristic of the nonlinearity by cascading a nonlinear block between two linear blocks as described by the Wiener-Hammerstein nonlinear system identification model [44]. The linear blocks are represented by filters (cf. Figure 4-1). Figure 4-2 demonstrates that the emulating component for the power amplifier HMC7229LS6 from Analog Devices [25] accounts for harmonic distortion, gives the correct gain in quasi-linear mode and power saturation properties in large signal input.

Figure 4-1: Wiener-Hammerstein model

The DDS output can be modelled as a quasi-perfect sine wave with low-level spurious signals. This is due to the finite precision in digitally generated sine signals. The spurious-free dynamic range (SFDR) is larger than 50 dBc.

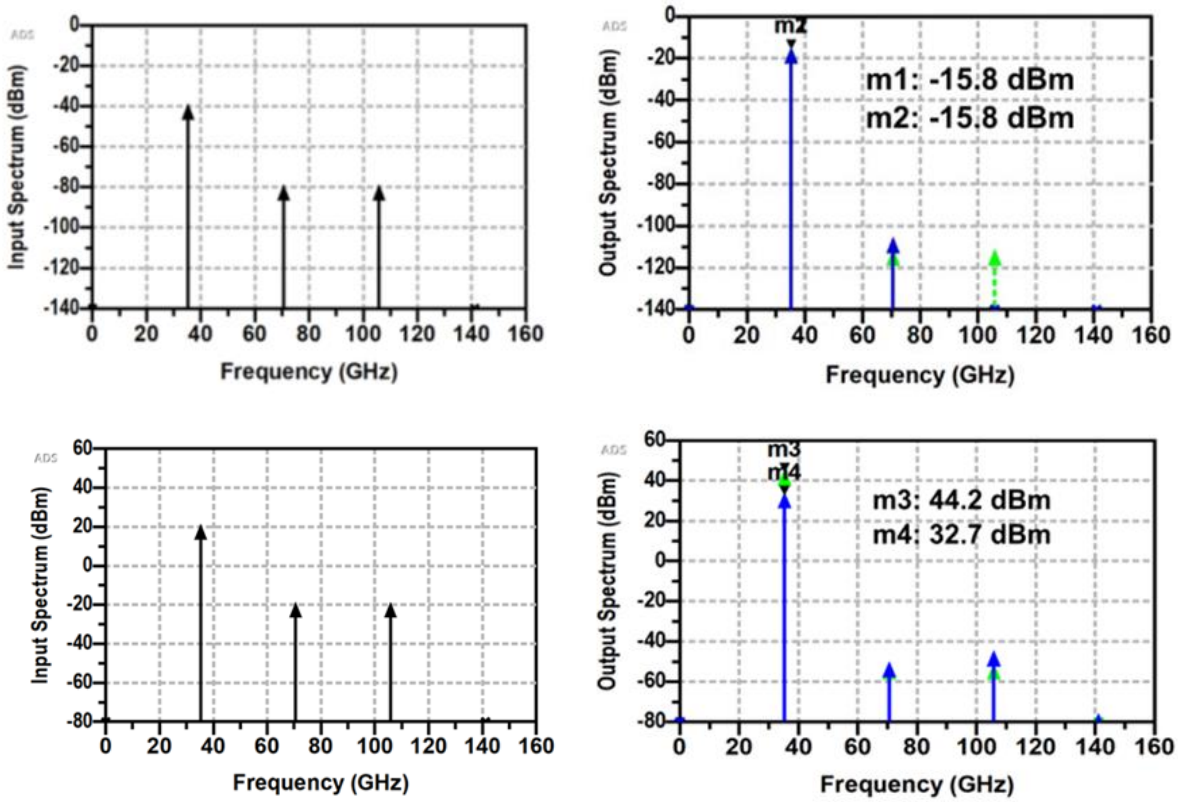

Figure 4-2: Frequency characterization of 2nd - and 3rd -order nonlinearity of PA HMC7229LS6 *(dotted green) and emulating component (solid blue) a) in quasi linear mode and b) in saturation. The emulating component shows a saturation at 32.7 dBm and accounts for harmonic distortion and self-mixing.*

4.1.2 Propagation model

We simulate the antenna, the propagation of the transmitted wave and the received wave scattered from the object with a full 3D electromagnetic (EM) simulation. The 3D EM simulation scheme is shown in Figure 4-3. We subdivide the propagation domain into a scattering volume

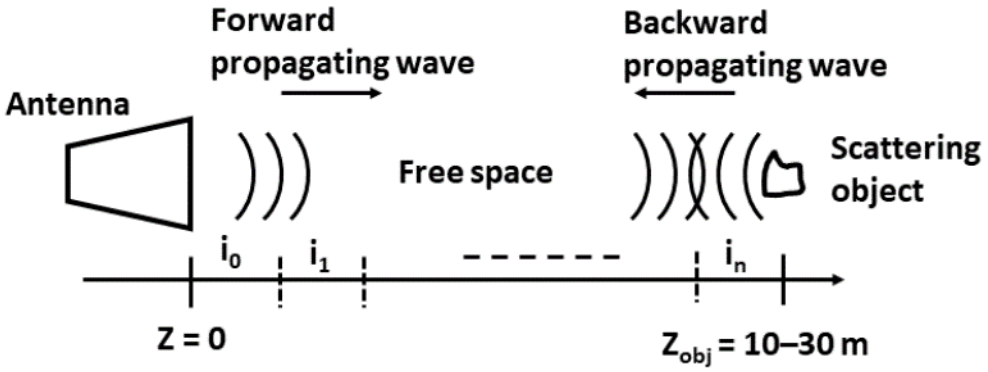

Figure 4-3: Simulation scheme of propagation model

around the Tx and Rx antennas and the object, while the distance to the object is modelled with slabs of pure EM wave propagation. This decomposition results in extremely efficient full-wave simulation of the entire domain and includes consistent simulation of the antenna for the transceiver. We export the electromagnetic field transmitted from the antenna and use it as input in the free space propagation. We divide the free space in N identical sectors as shown in Figure 4-3, and export the E and H fields for each sector on the interface plane between the free space sectors. With this method, it is possible to simulate the propagation in the forward and backward direction. Finally, we import again the EM field after the propagation in the free space in the antenna simulation. This enables the exact calculation of the received signal from the backscattering. We perform the 3D EM simulations with CST Studio using a GPU. This permits to simulate 1 m of free space propagation in about 20 minutes. The full procedure led to the calculation of S-parameters used in transceiver simulations.

Figure 4-4 reports the amplitude of the transmission coefficient from Tx to Rx. The values are calculated for an object with radar cross-section of $\sigma = 0.01$ m² at 10 m from the antenna. We compare the results with the values calculated with the standard radar equation for an object at 10 m and at 20 m. The 3D EM results fluctuate between the simple radar equation values for 10 m and 20 m. With increasing frequencies, the amplitude rises, which might be due to higher object reflectivity at higher frequencies. The EM simulations provide more realistic results and phase information.

The above results for the received and the transmitted signal were included in the global radar simulations as a propagation model.

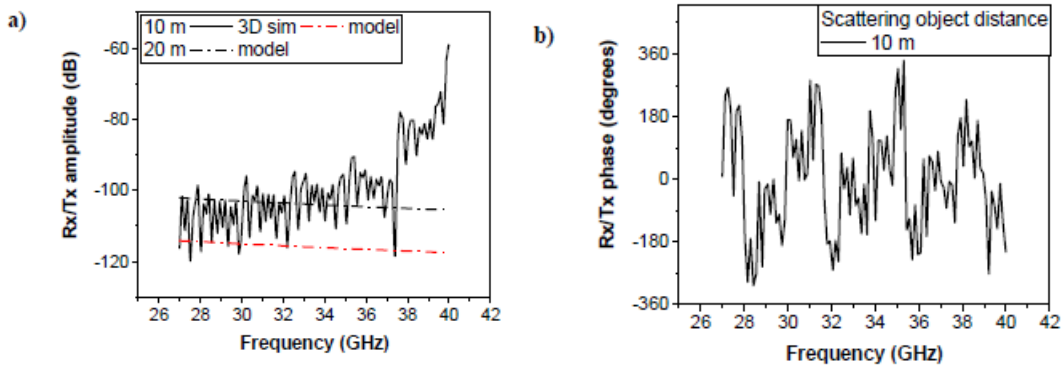

Figure 4-4: Ratio between the received and the transmitted signal
calculated for a scattering object 10 m and 20 m far from the antenna. a) amplitude, b) phase

4.2 Simulation results

We simulated the radar system using Keysight ADS. A Harmonic Balance simulation provided the results for the output spectrum. In addition, we implemented an Envelope simulation to verify the performance of the radar. In each simulation, the propagation model described in Section 4.1.2 was included for an object at 10 m and of radar cross section 0.01 m². The antenna gain is 15 dB.

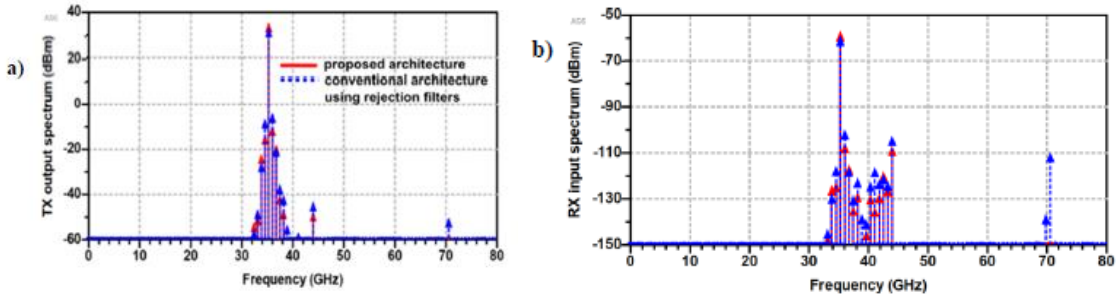

Figure 4-5: Spectrum of a) Tx output and b) Rx input using propagation model.
There is a rich Tx spectrum below -60 dB. The apparition of harmonics around 40 GHz in the Rx dynamic range is due to the high reflexivity of the target with increasing frequency, unpredictable by the classic radar equation

We compared the proposed radar architecture to a conventional radar transceiver using 5th order BPF for image rejection and harmonic cancellation. The results are displayed in Figure 4-5 and Table 4-1. The proposed architecture manages to provide a 34.9 dBm output; this is due to the gain while combining both paths of the enhanced push-pull amplifier. The Hartley and enhanced push-pull architecture combined achieves an in-band SFDR of 45.2 dBc and an out-of-

band SFDR of 107.9 dBc which is better than an architecture using image reject filters and facilitates signal integrity. Figure 4-6 shows the receiver baseband output spectrum, after deramping. The received signal is clearly showing a single strong reflector with close to Lorentzian shape, testifying of good signal integrity.

Table 4-1: Output interference level with respect to the carrier

Frequency	Proposed architecture	Conventional architecture with rejection filters
Carrier (dBm)	34.9	32.7
LO (dBc)	-45.2	-38.4
Image (dBc)	-53.5	-52.7
2xCarrier (dBc)	-126.5	-87.5
3xCarrier (dBc)	-140.5	-79.4
10 GHz (dBc)	-107.9	-104.9

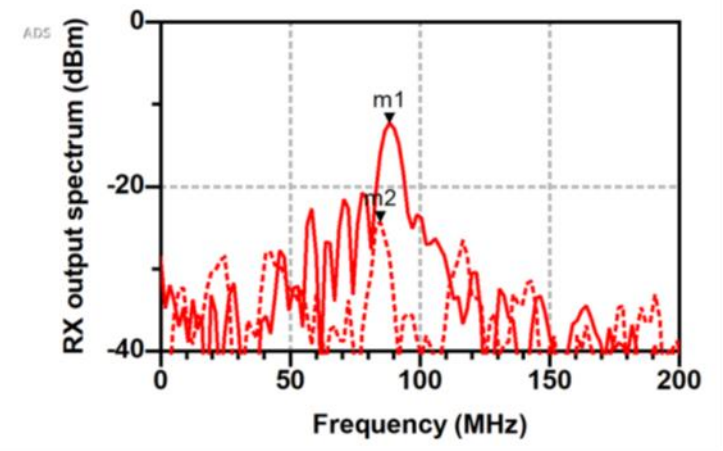

Figure 4-6: Rx baseband output spectrum for proposed architecture with radar equation *(dotted) and propagation model (solid). NB: the path attenuation is smaller with the propagation model than for the radar equation (cf. Section III.B) hence the greater signal output for the propagation model (m1).*

4.3 Summary and remarks

In this Chapter, we have presented the system design of a mm-wave FMCW imaging radar in the scope of full front-end integration. The proposed architecture improves signal integrity and guarantees spectral purity. It includes two Hartley architectures and an enhanced push-pull amplifier for image and harmonic cancellation, which can be easily integrated on silicon. The radar system operating at 35 GHz shows a spectral purity < -45 dBc in band, and < -100 dBc out of band. We carried out the simulations with realistic datasheet-based components and we used

an innovative full 3D electromagnetic simulation to model the antenna and the path loss to and from the scattering object. This guarantees a close-to-reality simulation environment, essential before implementation.

The results of this Chapter were published in the article 'Millimeter-wave imaging radar system design based on detailed system radar simulation tool,' and presented at the 2018 22nd International Microwave and Radar Conference (MIKON) in Poznan, Poland in 2018.

Chapter 5

System simulation of the MIMO architecture at baseband frequency

In this Chapter, we investigate the performance of the proposed MIMO radar architecture based on CDMA. We compare the results using BPSK and QPSK intra-pulse modulation schemes. The investigation is carried out at baseband frequencies.

5.1 Simulation results

Without loss of generality, we simulate a bi-static 8×1 FMCW radar based on BPSK and QPSK intra-pulse modulation using MATLAB. The channel is noiseless. We apply the signal model developed in Chapter 2 and we use the same parameters as in Chapter 4. The baseband signal has an initial frequency of 200 MHz and a 1 GHz bandwidth. The chirp duration is 500 µs. The range resolution for the 1 GHz FMCW radar is: $S_r = \frac{c}{2B}$ = 15 cm.

We consider four cases, where the cumulated ranges {Tx i, target, Rx j}, with $i = 1..8$ are:

1. [20m, 20.3m, 20.6m, …, 22.1m], close-range detection, at the limit of the range ambiguity,
2. [20m, 21m, 22m, …, 27m], close-range detection,
3. [120m, 120.3m, 120.6m, …, 122.1m], mid-range detection, at the limit of range ambiguity,
4. [120m, 121m, 122m, …, 127m], mid-range detection.

The chirps are coded with N_c-chip Gold sequences. To counter the well-known near-far problem, we suppose that the Tx units regulate their output power so that signals reflecting on the target have about a same power level when arriving on the Rx unit. For each scenario, we estimate the different cumulated ranges. The range detection is considered accurate and the signal fully recovered only when the frequency step of the deramp spectrum is greater than the

difference between the estimated beat frequency and the actual beat frequency: only error-free detections are considered.

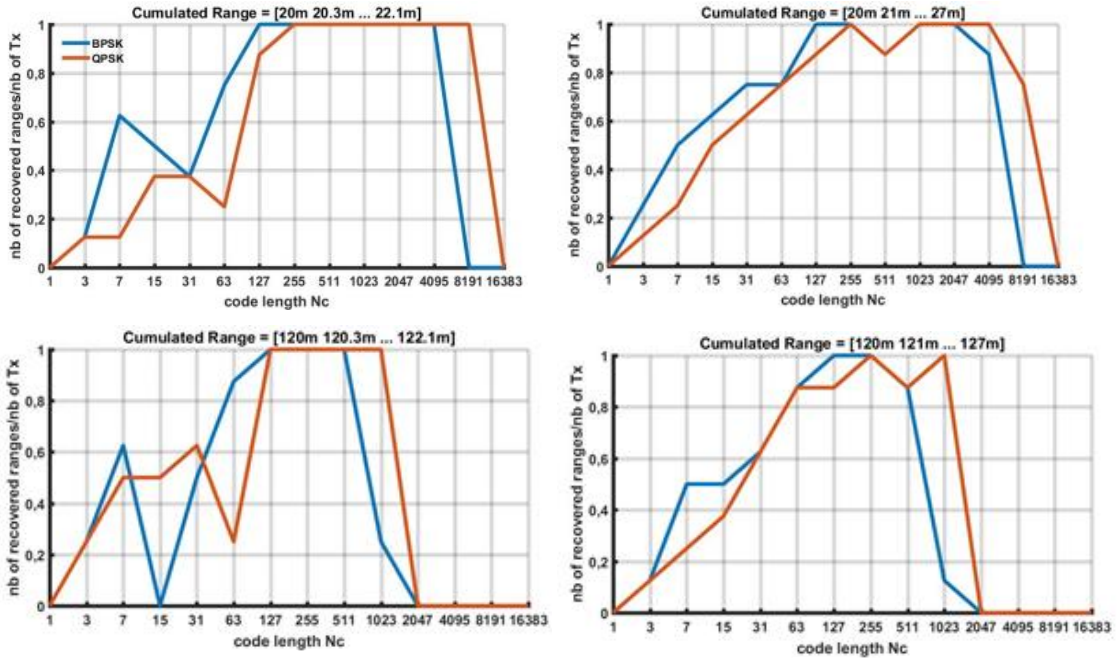

Figure 5-1: Comparison of the modulation schemes in the recovery of the cumulated ranges {Tx i, target, Rx}, i=1..8 with respect of the Gold sequence length in various range scenarios.

Figure 5-1 shows the percentage of accurate detection along the Tx units, with respect to the code length. In other words, it shows the capability of the Rx unit to recover correctly the signals coming from the different Tx units. The results show that a full recovery of the signals coming from every Tx is mostly possible when the code is long enough: 127 chips or longer. When the code becomes too long, the detection reaches a threshold, above which there is no possibility of recollecting any signal. Intra-pulse BPSK modulation cannot recollect any signal above 8.19 MHz for short range, and above 2.046 MHz for long ranges. Intra-pulse QPSK modulation cannot recollect any signal above 8.191 MHz for short range, and 1.023 MHz for long range. BPSK performs better with longer code length because its coding frequency is twice as less than BPSK; but the actual coding rate between QPSK and BPSK remains the same.

In general, BPSK modulation gives more accurate range estimation than QPSK modulation for code lengths shorter than 127 chips. This may be because the Gold sequences have an odd number of chips while two chips are needed to code a symbol. This imbalance on the last chip could deter the orthogonality properties of the Gold sequence for short lengths. Also note that for the same reasons, no detection is possible when a single-chip code is employed, since QPSK works when the length of the code is larger than 2 chips. Another interpretation would be that

intra-pulse coding is optimal regardless the phase shift keying pattern when the code rate is between 254 kHz and 8.19 MHz for short range, and between 126 kHz and 1.022 MHz for mid-range. This would explain why QPSK curve seems to be a translation of BPSK when the code length in increased by a factor 2. Investigating higher-bit PSK schemes is necessary to conclude. For any coding scheme, the detection rate increases almost linearly with the code length when the Tx/Rx are spatially separated above the radar ambiguity. Conversely, the recollection of the signals increases irregulary with the code length when the Tx/Rx units are within the range ambiguity of the radar. Finally, the amount of signals recollected with respect to the code lengths is higher for shorter ranges. This might be due to the fact that the phase change within the pulse artificially cut the pulse duration, hence the decrease the range of the radar. Note that the range – or signal – recovery criteria is chosen to be strict, therefore Figure 5-1 does not distinguish whether the range estimation is completely uncorrect or if the range was estimated within a certain error. This could be investigated in a next study.

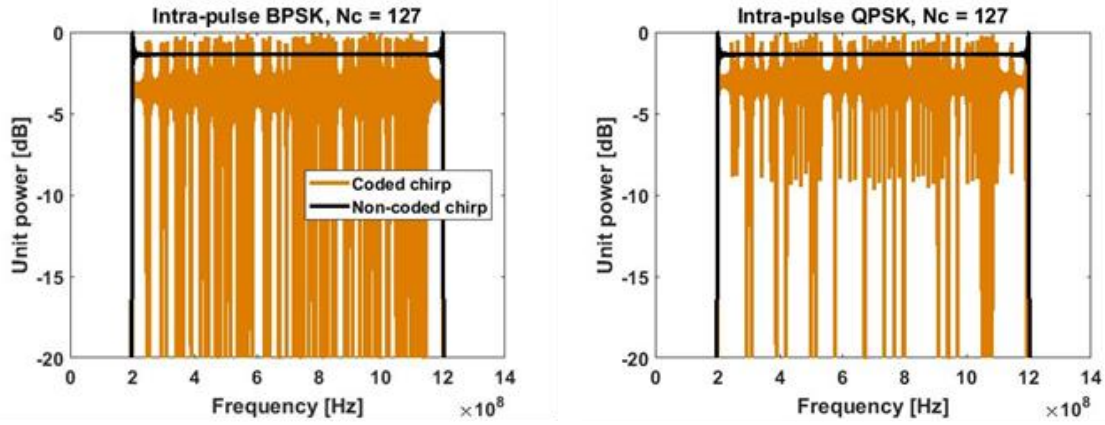

Figure 5-2: Comparison between the spectrum of a non-coded signal and the transmitted spectrum of Tx 1 using intra-pulse BPSK and QPSK

We consider the case when N_c = 127. This is when most of the detections start to be error-free. Figure 5-2 compares the spectrum of an uncoded transmitted signal, and the one of a coded transmitted signal, arbitrarily from Tx 1, for both modulation schemes. The bandwidths for non-coded and coded signal are the same, and this far below 3 dB. The proposed modulation schemes do not deteriorate the spectrum. The spectrum features many nulls, due to the convolution of a Dirac comb by the rectangular function to create the code, which is translated into a multiplication of Dirac comb by a sinc function in the frequency domain. Note that the shift to zeros are twice as less using QPSK because twice less symbols are needed to code the chirp.

Figure 5-3 shows the output spectra of the deramp spectra for BPSK intra-pulse modulation. We compare the deramp spectrum when the transmitted waveforms are not coded, and when

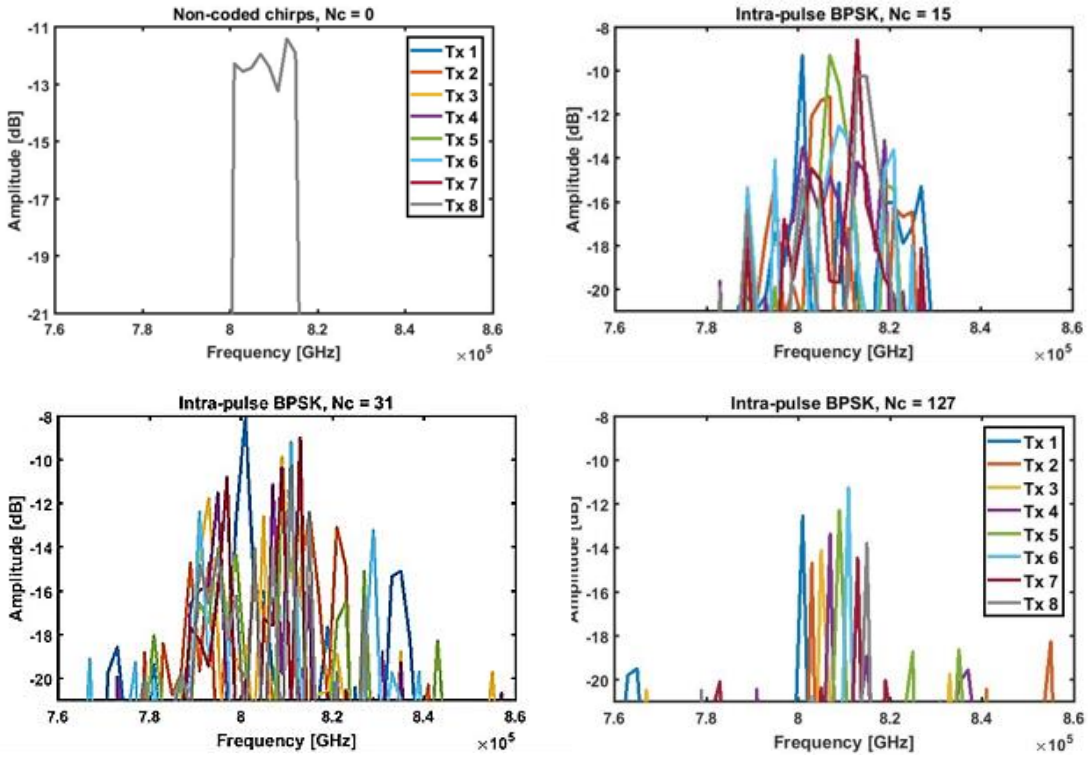

Figure 5-3: Deramp spectra of the received signal at Rx j with the coded signals from Tx 1 to Tx 8, for different Gold sequences lengths

Code lengths are a) 0 bits, b) 15 bits, c) 31 bits and d) 127 bits. Intra-pulse BPSK was used. Range is 120m, 120.3m… 122.1m.

they are coded with increasing Gold sequence length. When the code is 127 chip-long, the range can be recollected with a signal-to-side lobe ratio of at least 6 dB (signal from Tx 5) and more than 10 dB (signal from Tx 6). It is clear that the recollection is becoming more and more blur, with decreasing peak-to-sidelobe ratio when the code is shorter. Figure 5-4 illustrates QPSK-based coding in the same condition. We can see that the deramp spectrum when using QPSK-based coding is richer. The detection is accurate with a peak-to-sidelobe from 1 dB (signal from Tx 2) up to 4 dB (signal from Tx 1), which is much less than BPSK-based detection. This could corroborate the fact that the code correlation might be affected by QPSK coding, since the peak-to-sidelobe ratio depends on the code correlation properties [19].

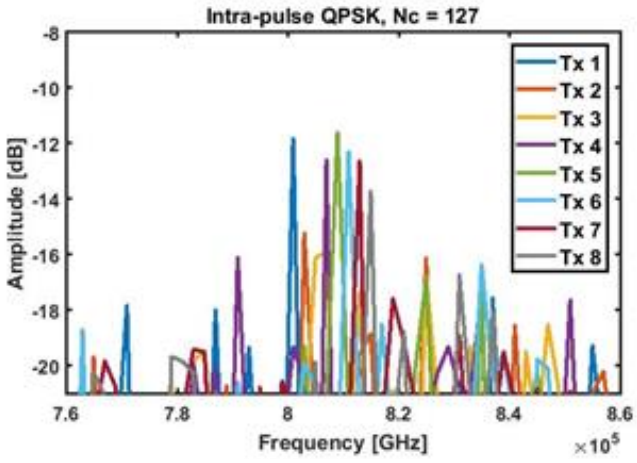

Figure 5-4: Deramp spectra of the received signal at Rx j with coded signals from Tx 1 to Tx 8. *Range is 120m, 120.3m… 122.1m.*

5.2 Summary and remarks

In this Chapter, we presented a FMCW MIMO radar using coding division multiplexing, intended for simultaneous signaling with all Tx and receiving with all Rx. The coded FMCW chirps were directly generated by a frequency- and phase-controlled DDS, which reduces drastically the architecture complexity. We compared BPSK and QPSK intra-pulse modulation techniques in various range scenarios. The results showed that the range estimation with satisfying peak-to-sidelobe ratio is the most accurate within a given code rate range. Furthermore, intra-pulse phase modulation has the advantage of being spectrum-, time- and energy-saving compared to classic pulse modulation. Its high coding rate could be achieved by latest DDS technologies.

Due to substantial memory resource requirements for the simulation of the system, the study was conducted at baseband frequencies. It does not consider the influence of the components of the radar. In the next Chapter, we aim to validate the results at carrier frequency in a more realistic simulation environment.

The results of this Chapter were published in the article ‘CDMA-based MIMO FMCW radar system performance using intra-pulse phase modulation,’ and presented at the 16th European Radar Conference (EuRAD) in 2019 in Paris, France.

Chapter 6

System simulation of the MIMO architecture at carrier frequency

This Chapter presents a step-by-step demonstration of the feasibility of a CDM-based MIMO FMCW radar system using intra-pulse BPSK modulation, at carrier frequencies. The proposed radar system operates in the W-band at 90 GHz. It is developed in the frame of the second MIMIRAWE project (MIMIRAWE II), the goal of which is to investigate compact and modular MIMO radar-based sensor for orbital rendezvous and imaging at millimeter-wave frequencies. The radar architecture proposed in this Chapter upgrades the architecture presented in the first MIMIRAWE project (MIMIRAWE I) (see Figure 6-1), by replacing off-chip components by highly-integrable architectures and by encoding the FMCW chirp using a frequency- and phase-controlled direct digital synthesizer (DDS). The proposed architecture is shown in Figure 6-2. The feasibility study is demonstrated on Keysight ADS 2020 Update 1. We consider a 2×1 MIMO radar. The baseband frequency is 1 to 10.5 GHz. The carrier frequency is [85..94.5 GHz]. The bandwidth is 9.5 GHz for a range resolution of 16 mm. We encode the chirps with 127-bit long Gold sequences. When referring to de-ramping, we will mean multiplying the transmitted signal with the received signal and integrating the product of the signals by a Fourier transform. In ADS, the integration is performed by the generalized discrete Fourier transform: the chirp Z-transform.

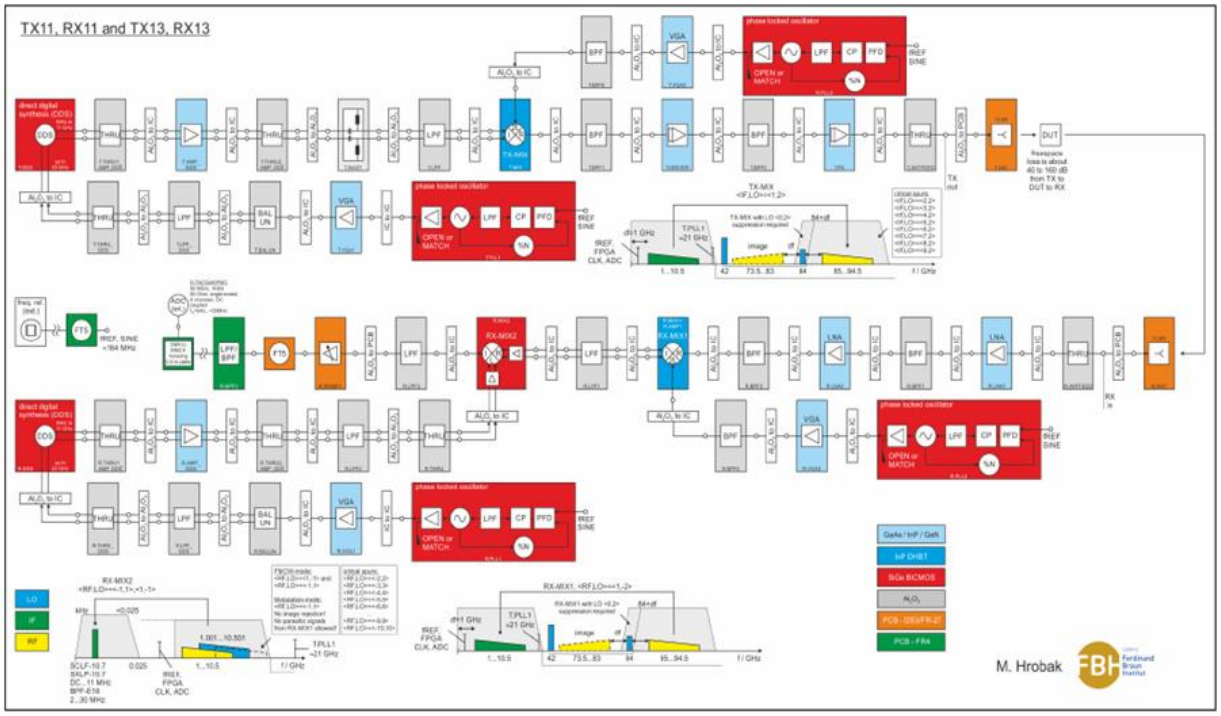

Figure 6-1: Original MIMIRAWE I radar architecture.

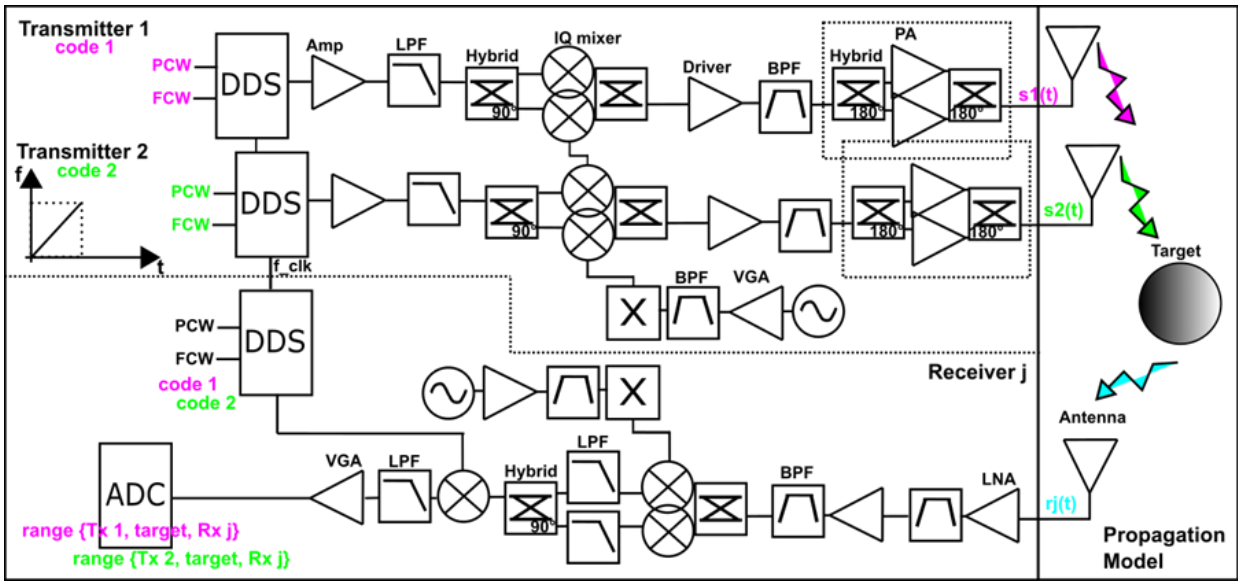

Figure 6-2: Proposed MIMIRAWE II radar architecture.

The new architecture uses a Hartley architecture for image suppression and a push-pull amplifier for second order harmonic cancellation.

6.1 DDS model

We want to emulate the creation of the intra-pulse BPSK-modulated ascending chirp by the DDS using ADS system blocks. The proposed model is shown in Figure 6-3.

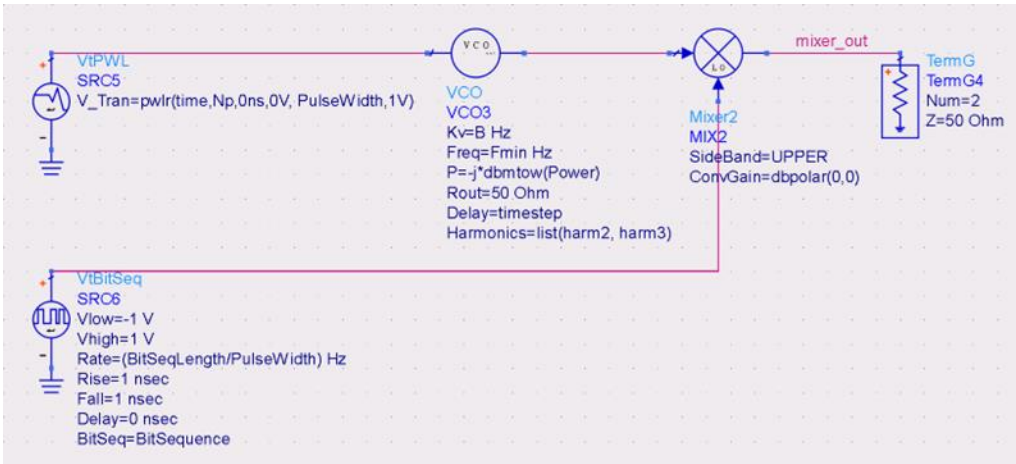

Figure 6-3: Proposed DDS model (ADS system blocks).

6.1.1 Creation of the ascending chirp

The ascending chirp is normally – hardware-wise – created and controlled digitally by the DDS which can modulate both frequency and phase of the chirp by frequency and phase control words [13],[14]. For the sake of simplification, we create – software-wise – the chirp in a full analogue approach using a voltage-controlled oscillator (VCO). An ascending voltage ramp tunes the VCO, so that the instantaneous frequency is an ascending ramp. For this we use the piecewise linear voltage source block **VtPWL** and the **VCO**.

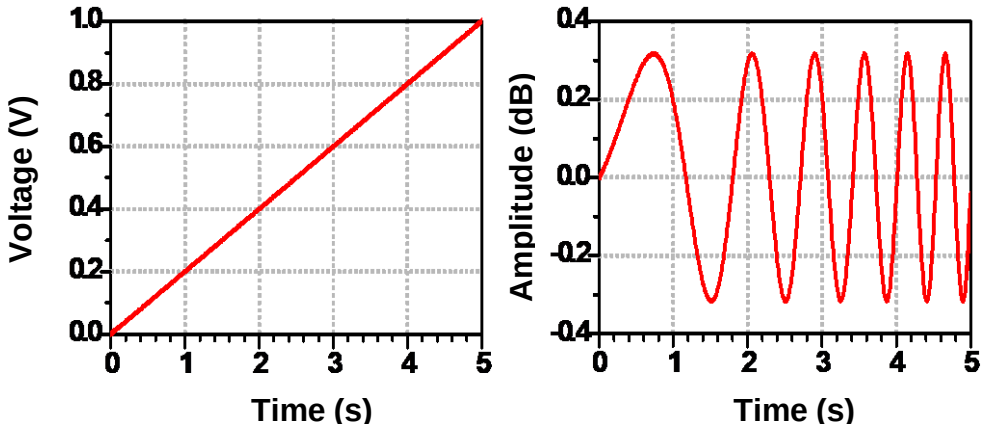

Figure 6-4: Voltage ramp and ascending chirp.
Scale: Fmin = 0.2 Hz, Fmax = 2.2 Hz, PulseWidth = 5 s.

The voltage ramp spans from 0 to *PulseWidth*, the output voltage is from 0V to 1V. The number of pulses *Np* is 1. Figure 6-4 shows the output voltage ramp. The VCO fundamental frequency is the minimum frequency *Fmin*. The frequency tuning sensitivity Kv is *B*. Thereby we should obtain a frequency span from *Fmin* to *Fmin+B*.

Figure 6-4 also shows the VCO output for the proposed alternative model. The ascending chirp is correctly generated. It corresponds to $s(t) = A_S\cos(\varphi_S(t))$ in the theory developed in Chapter 2.

6.1.2 Creation of the modulating encoding signal

We create a modulating encoding signal which will be multiplied in the time domain by the chirp. The modulating signal is a train of rectangular functions of values -1 and 1, corresponding to code bits 0 and 1 respectively. It corresponds to the train of rectangular function $\text{rect}(N_c t/nT - (2l-1)/2)$ in the theory developed in Chapter 2. Thereby, the phase of the chirp signal will be shifted by 180° when the code bit is 0 and by 0° when the code bit is 1.

We use the voltage source, pseudo random pulse train defined at continuous time by bit sequence **VtBitSeq** block. Each code symbol has a duration of *PulseWidth/BitSeqLength*.

Modelling the encoding signal with ADS has the considerable advantage of including a rise and fall time between each pulse of the encoding signal, which is done with difficulty by hand. In simulation, we chose a rise and fall of 1 ns.

6.1.3 Creation of the coded chirp

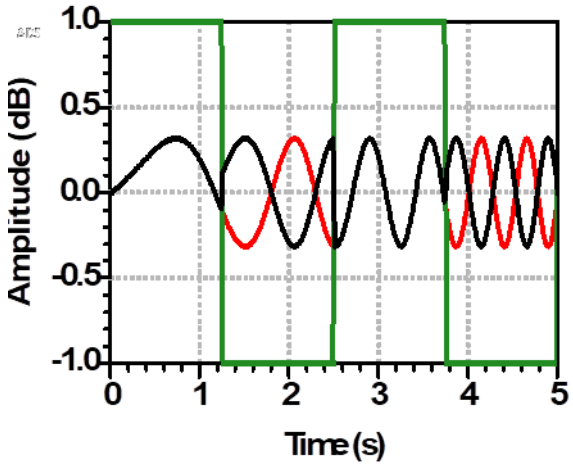

Figure 6-5: Creation of the coded chirp (black) from the multiplication of the encoding signal (green) with the non-coded ascending chirp (red).
Scale: Fmin = 0.2 Hz, Fmax = 2.2 Hz, PulseWidth = 5 s, BitSeqLength = 4, BitSequence = 0101.

We want to create the coded chirp which is modelled by the multiplication in the time domain of the chirp signal with the coding signal. We use the RF system block **Mixer2**. To avoid the split

of power on both sidebands, we use the upper-sideband conversion of the mixer. Figure 6-5 shows the coded chirp together with the encoding signal and the non-coded chirp. We see that the phase modulation within the FMCW is accurately performed and that the power of the chirp is conserved.

6.2 Baseband simulation results

As a pre-validation step, we investigate the feasibility of the method at baseband frequency, that is without frequency conversion. Due to computation limits, we simulate one pulse only, N_p = 1.

6.2.1 1×1 Radar

In a first step, we consider a simplified baseband model of a 1×1 FMCW radar front-end. Figure 6-6 depicts the 1×1 baseband model. The Tx unit comprises the DDS only. The Rx unit is composed of a DDS and a mixer for the de-ramping. A single time delay block represents the propagation. The de-ramping consists in the multiplication of the received delayed signal with a non-delayed CDMA-modulated reference signal. We will compare the deramp output when: 1) the transmitted code and the reference code for the de-ramping are similar, 2) the transmitted code and the reference code for the de-ramping are different, i.e. quasi-orthogonal.

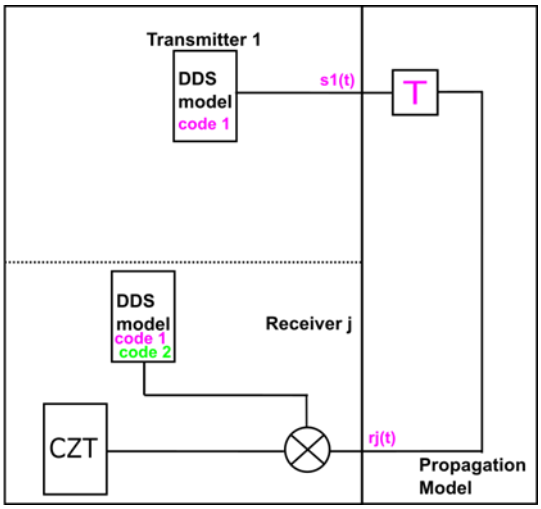

Figure 6-6: Baseband model and output spectrum for 1×1 radar.

Following the investigation made in Chapter Chapter 5, we use 127-bit long Gold sequences and a pulse width of 500 µs. The radar range is 10 m. This should guarantee that the code rate is high enough to allow a high detection probability. We expect a clear deramp spectrum with high

signal integrity when transmitted signal and reference signal are the same and no detection when transmitted signal and reference signal are different.

Figure 6-7 compares the deramp spectra when the transmitted code and the reference de-ramping code are similar, and when they are different. The results show a good recovery of the signal when the codes are similar: the output spectrum shows a clear Dirac impulse at 1.267 MHz with about 35 dB spurious-free dynamic range (SFDR). This testifies of high signal integrity. The measured range is calculated $R=cTf_B/2B$. It equals 10.003 m; the range is accurately determined with 3 mm off, corresponding to an error 0.03%.

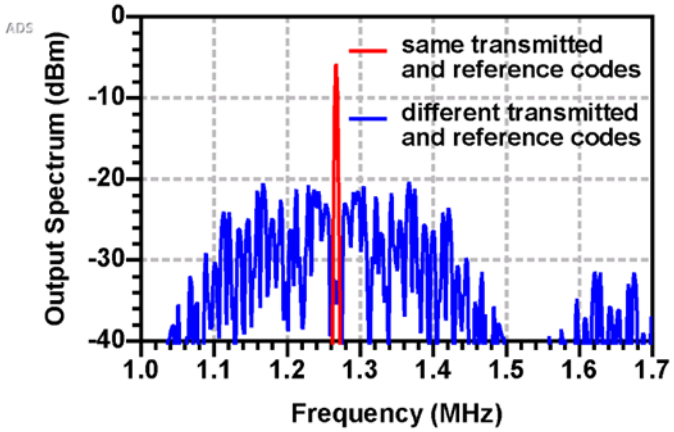

Figure 6-7: Output spectrum for 1×1 radar detection when transmitted code and reference code for deramping are the same

fb = 1.267 MHz, SFDR = 35 dBc; different (orthogonal): fb = 1.367 MHz, SFDR = 20 dBc.

When using a reference signal modulated by a Gold code which is quasi-orthogonal to the transmitted code, the output spectrum is not clear. Instead of a Dirac impulse, we see a window about 400 kHz-wide. The signal when the codes are orthogonal is 13 dB lower than the signal when the codes are similar. If we take the maximum, we calculate that the detection is accurate with 80 cm-off which corresponds to a large 7.9% error. There is no signal integrity even though the simulation environment is almost ideal.

6.2.2 2×1 Radar

We simulate a two-channel 2×1 radar. Figure 6-8 shows the baseband 2×1 FMCW radar architecture. The ranges of transmitter unit 1 and transmitter unit 2 to the receiver are 10 and 11 m respectively. Both transmitted signals are delayed with respective corresponding times of travel. The delayed signals are then added. A single receiver unit identifies the signal coming from transmitter 1 or transmitter 2 by de-ramping the received signal with code 1 or code 2 respectively. We keep the same codes and the pulse width remains 500 µs.

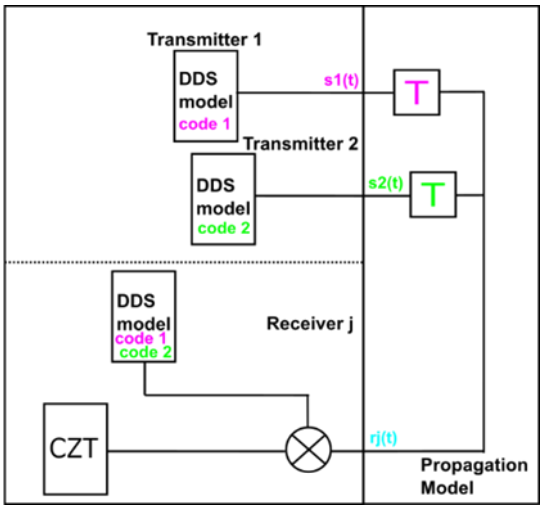

Figure 6-8: Baseband model for 2×1 radar detection.

Figure 6-9a shows the deramp spectrum when the receiver unit multiplies the received signal with the transmitted signal from Tx 1. We see a clear Dirac impulse at 1.268 MHz and the first sidelobes are 13 dB lower. The range when identifying channel 1 is 10 m with 11 mm off, which corresponds to an error of 0.1%. This is slightly more than when a single signal is sent (cf. Figure 6-7).

Figure 6-9b shows the deramp spectrum when the receiver unit multiplies the received signal with the transmitted signal from Tx 2. Likewise, we see a clear Dirac impulse but shifted to 1.394 MHz and the first sidelobes stay about 13 dB lower. The range when identifying channel 2 is 11 m with 5 mm off, which corresponds to an error of 0.05%.

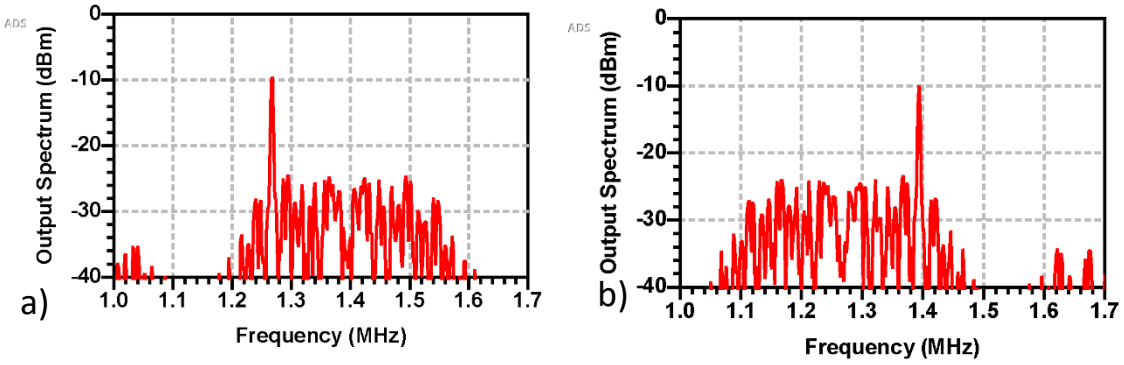

Figure 6-9: Output spectrum for 2×1 radar baseband detection of a) channel 1 *fb = 1.268 MHz, SSLR = 13 dBc; b) channel 2: fb = 1.394 MHz, SSLR = 13 dBc.*

We recognize in Figure 6-9a the contribution of the detection when the transmitted code and the reference de-ramping code are similar: the Dirac impulse matches the one of Figure 6-7.

Likewise, the contribution of the (non-)detection when the transmitted code and the reference de-ramping code are different can be seen in Figure 6-9b: the 400 kHz-wide window matches perfectly the one of Figure 6-7.The sidelobes are therefore inherent to CDMA-based MIMO system, as the result of unperfect orthogonality. They can be reduced by using more orthogonal codes.

The Envelop simulation results show that the different ranges can be both recollected with a maximum of 0.1% error. This confirms the good performance of 2×1 FMCW radar using CDMA-based intra-pulse modulation at baseband frequency.

6.3 Carrier simulation results

In this Section, we verify if the good performance still holds when considering carrier modulation and a full but ideal radar system comprising classic elements such as mixer for up-conversion, amplifiers and filters. The investigation is still carried using Keysight ADS and we proceed step by step. We simulate a two-channel 2×1 radar. The radar range Tx1-Rx is 10 m and the radar range Tx 2-Rx is 11 m. Both transmitted signals are delayed with corresponding time of travel. The delayed signals are then added. A single receiver unit identifies the signal coming from transmitter 1 or transmitter 2 by de-ramping the received signal with code 1 or code 2 respectively.

It is essential to carry the investigation step by step to easily identify the impact of a specific stage on the radar performance when using intra-pulse BPSK modulation.

6.3.1 Step-by-step simulation protocol

6.3.1.1 Step 1: Consider frequency conversion

a) Using embedded single sideband mixer

Figure 6-10 shows the 2×1 radar architecture when adding an up-conversion stage to each transmitter unit, and a down-conversion stage to the receiver unit. The up- and down-conversion stages are composed of a single mixer block using embedded single sideband conversion (here the upper sideband). The LO is generated by a 42 GHz PPL, where the output signal is amplified, bandpass-filtered and then ×2 multiplied.

Figure 6-11 compares the deramp spectra when identifying channel 1 and channel 2. We see two clear Dirac impulses at 1.268 MHz and 1.394 MHz with a peak-to-sidelobe ratio (PSR) around 13 dBc. Other than the output power, there is no major difference between the output spectrum from the baseband simulation and the spectrum from frequency conversion simulation. The difference in power results in the loss brought by the mixer.

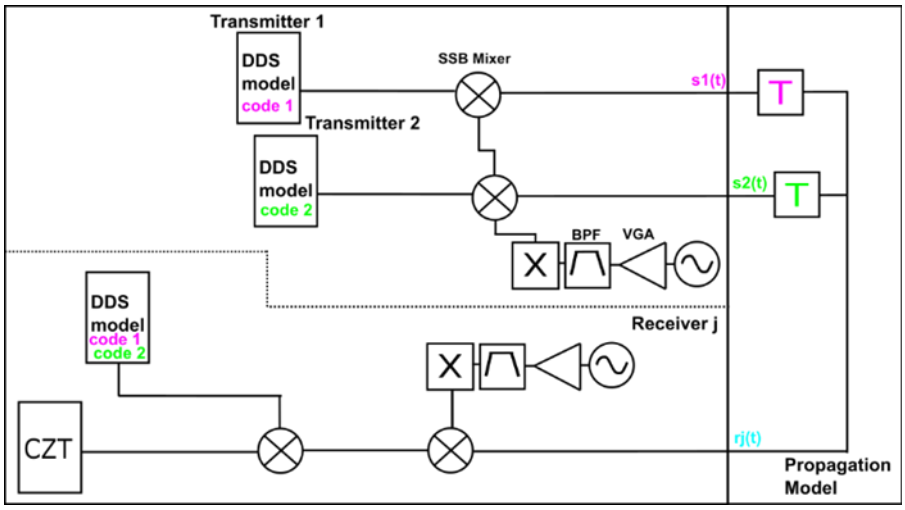

Figure 6-10: Step 1a: Block diagram of 2×1 radar architecture including baseband and frequency conversion stage based on embedded single sideband mixer.

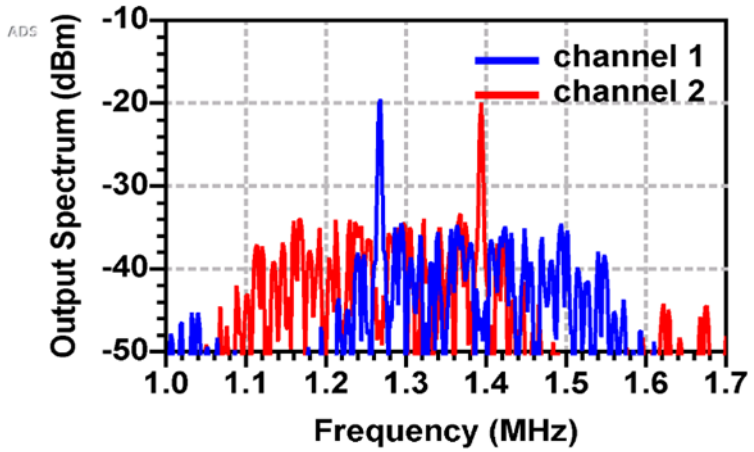

Figure 6-11: Step 1a: Output spectra of 2×1 radar architecture including baseband and frequency conversion stage based on embedded single sideband mixer.
fb,ch1 = 1.268 MHz, fb,ch2 = 1.394 MHz

The range when identifying channel 1 is 10 m with 11 mm off, which corresponds to an error of 0.11%. The range for channel 2 is correctly recovered at 5 mm off, representing an error of 0.05%. The results of the detection are the same as the results from the baseband simulation.

The results show that an ideal mixer does not impact the radar performance.

b) Using Hartley architecture

We want to evaluate the impact of the Hartley architecture on the detection. We investigate whether the phase shift affects the detection. Figure 6-12 shows the new simulated architecture featuring the Hartley architecture and the driver amplification.

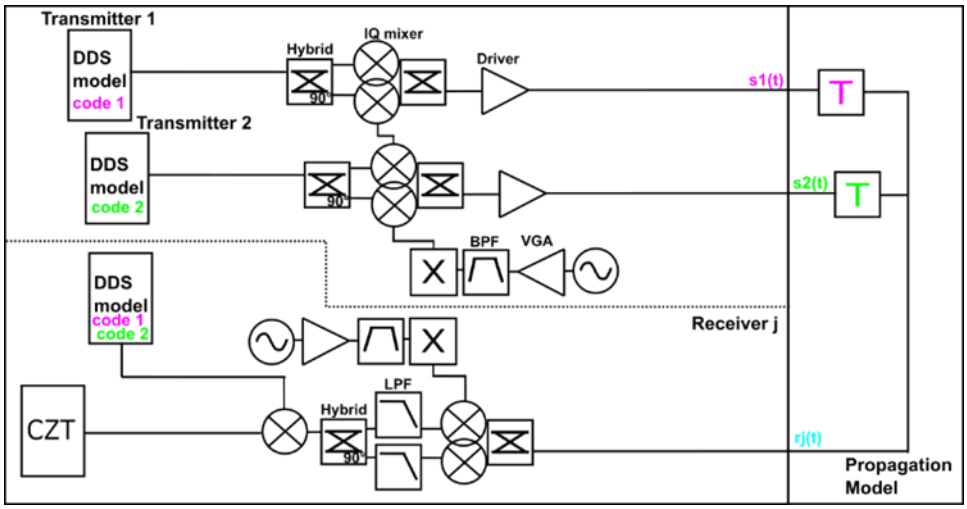

Figure 6-12: Step 1b: Block diagram of 2×1 radar architecture including baseband and frequency conversion stage based on Hartley architecture.

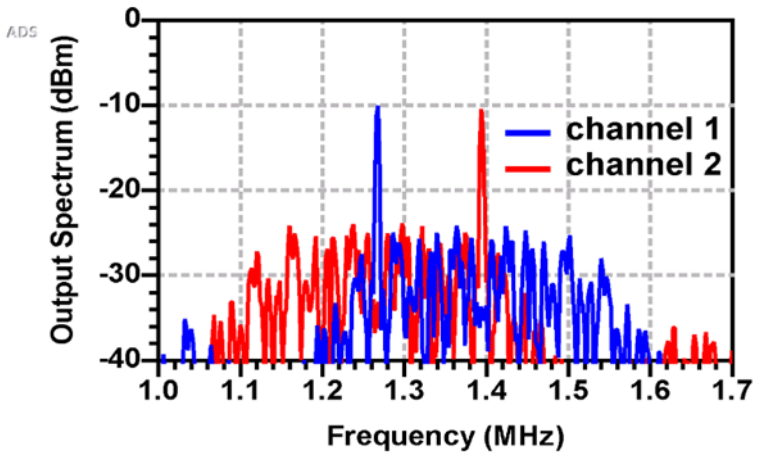

Figure 6-13: Step 1b: Output spectrum of 2×1 radar architecture including baseband and frequency conversion stage based on Hartley architecture.
fb,ch1 = 1.268 MHz, fb,ch2 = 1.394 MHz

Figure 6-13 shows that the range is still recollected with the same performance. The only difference remains the output power level, the increase being due to the amplification. This

proves that the phase shift necessary to perform the SSB conversion using the Hartley architecture does not affect CDMA-based intra-pulse phase modulation and therefore the detection capability of corresponding multi-channel architectures.

6.3.1.2 Step 2: Consider the Tx IF stages

We add the intermediate frequency stages of the Tx module. As seen in Figure 6-14, it is composed of an IF amplifier to sufficiently drive the up-converter and a low-pass filter to further lower the harmonics created by the DDS and the eventual imtermodulation products generated by the amplifier (although it should operate in the linear mode at such low power levels).

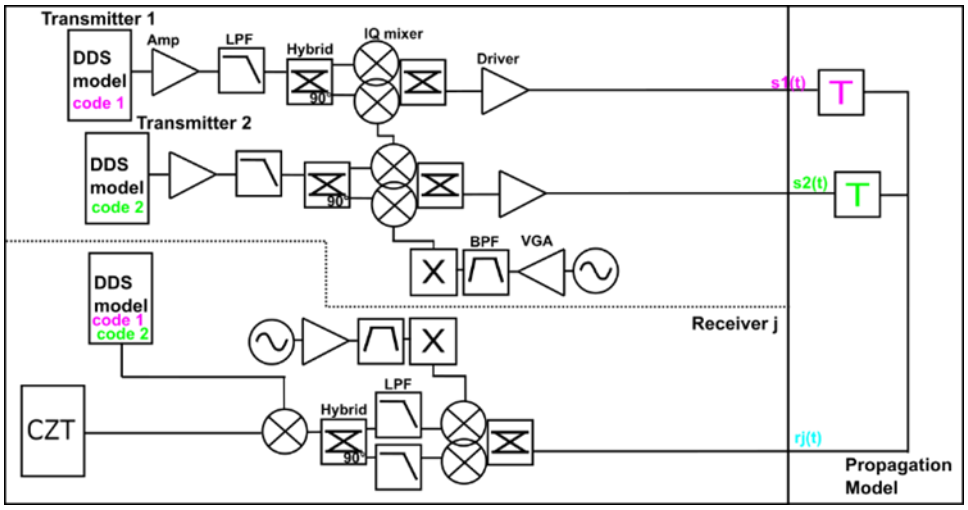

Figure 6-14: Step 2: Block diagram of 2×1 radar architecture including baseband, frequency conversion stage based on Hartley architecture and Tx IF stages.

Figure 6-15 shows that the ranges to both Tx units are still correctly estimated with the same performance. This means that the different channel can be identified, despite the addition of an amplifier and a LPF in both Tx modules. As before, the output power level differs due to gain/loss brought by amplification/filter.

This shows that the addition of a linear amplifier and a lowpass filter does not have an impact on the modulated signal and thereby, on the detection.

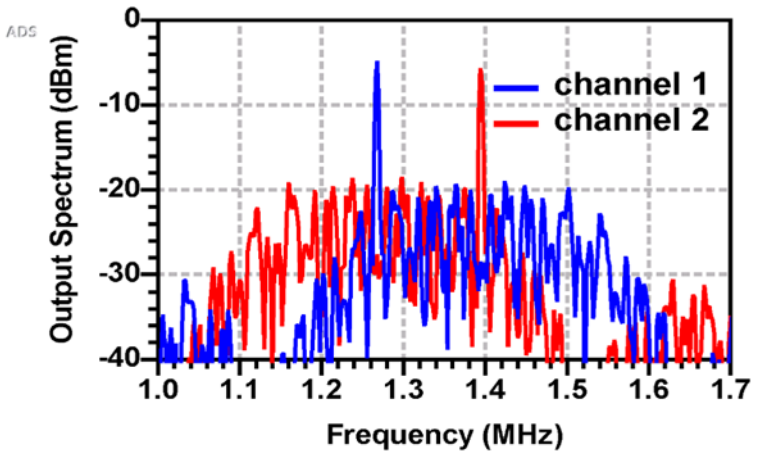

Figure 6-15: Step 2: Output spectrum of 2×1 radar architecture including baseband, frequency conversion stage based on Hartley architecture and Tx IF stages.
fb,ch1 = 1.268 MHz, fb,ch2 = 1.394 MHz

6.3.1.3 Step 3: Consider the Tx push-pull amplification stage

We investigate the impact of the push-pull architecture. In the simulation, we add a low-order (3rd-order) BPF and we use purposely linear amplifiers to better analyze the output signal. In case the detection is impacted by the simulated push-pull, it will be thereby clear that it will be caused by the addition of two 180° phase shift or by the addition of the bandpass filter. Previous simulations showed that the use of hybrid-couplers (although of different phase shift) and amplifiers did not have an impact on the detection performance of CDMA-based FMCW radar. The simulated architecture is shown in Figure 6-16.

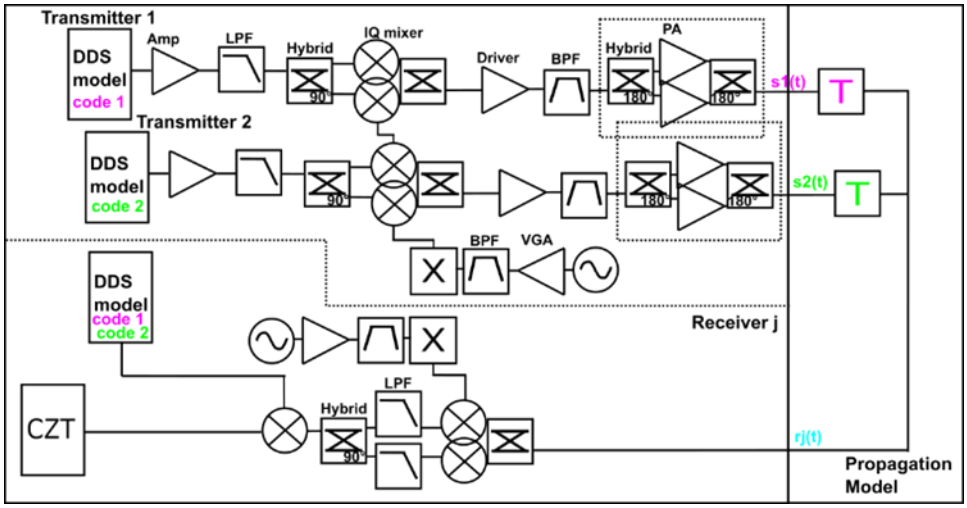

Figure 6-16: Step 3: Block diagram of 2×1 radar architecture including baseband, frequency conversion stage based on Hartley architecture, Tx IF stages and Tx push-pull architecture

An analyze of the output spectra displayed in Figure 6-17 shows that the output spectra still present a clear Dirac impulse with a SSLR around 13 dB, but the peaks have shifted to 1.270 MHz for the identification of channel 1 and to 1.396 MHz for channel 2. This time, the range to Tx 1 is recovered at 26 mm off, representing an error of 0.26%, and the range to Tx 2 is recovered at 21 mm off, representing an error of 0.19%.

This is the first decrease of the radar performance due to the addition of a stage. This shows that either the 3rd order bandpass filter or the push-pull architecture is very likely to deteriorate the signal and therefore the detection when using CDMA-based RADAR. However, since previous use of hybrid-couplers and amplifiers did not have an impact on the detection performance of CDM-based FMCW radar, it is more likely that bandpass filters cause the distortion of the modulated signal. Although the distortion is slight, it is important to note it to trace the evolution of the performance of CDM-based multi-channel RADAR block by block.

Note that once again, the change of power is due to the filtering/amplification.

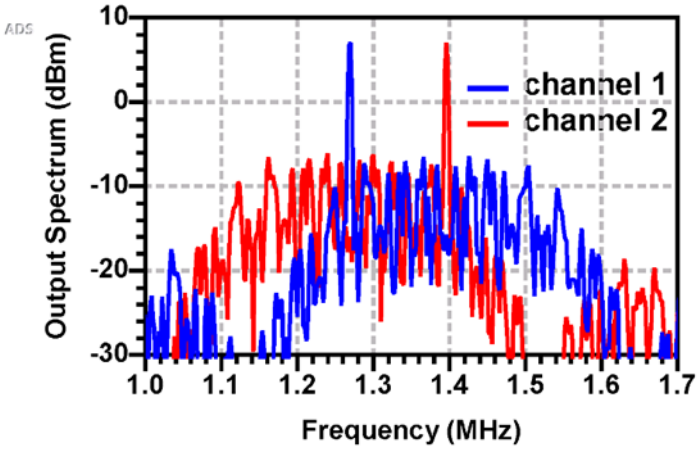

Figure 6-17: Step 3: Output spectrum of 2×1 radar architecture including baseband, frequency conversion stage based on Hartley architecture, Tx IF stages and Tx push-pull architecture.
fb,ch1 = 1.270 MHz, fb,ch2 = 1.396 MHz

6.3.1.4 Step 4: Consider the Rx RF low-noise amplification stages

The receiver of MIMIRAWE II features two stages of low-noise amplifications at RF frequency. Each stage is composed of a LNA followed by low-order (3rd) bandpass filter (Figure 6-18).

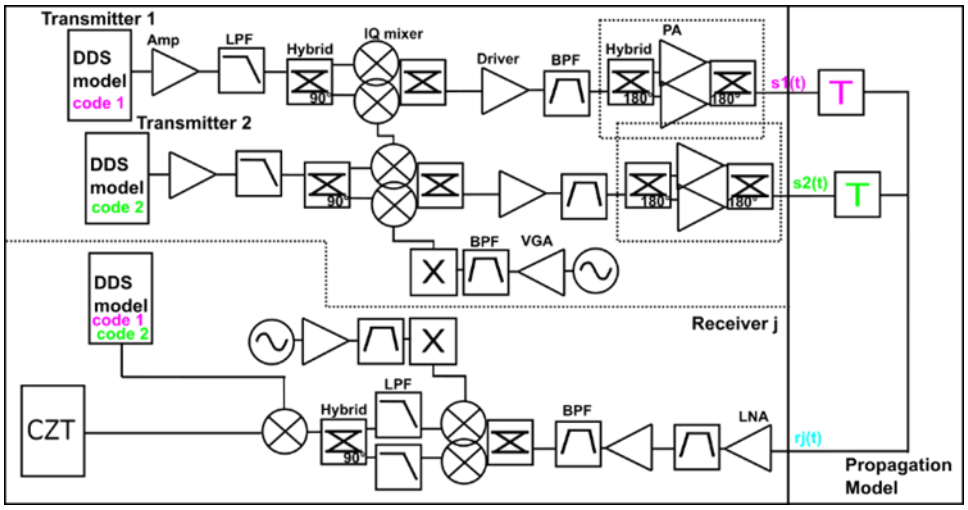

Figure 6-18: Step 4: Block diagram of 2×1 radar architecture including baseband, frequency conversion stage based on Hartley architecture, Tx IF stages, Tx push-pull architecture and Rx RF LNA stages.

The comparison of the output spectra on Figure 6-19 for channel identification shows both output spectra still present a clear Dirac impulse with a SSB ratio around 13 dB, but the peaks are further shifted to 1.272 MHz and to 1.398 MHz for the channel 1 and for the channel 2 respectively. The ranges are therefore recovered with 42 mm off, representing an error of 0.42%, and with 37 mm off, corresponding of an error of 0.34%.

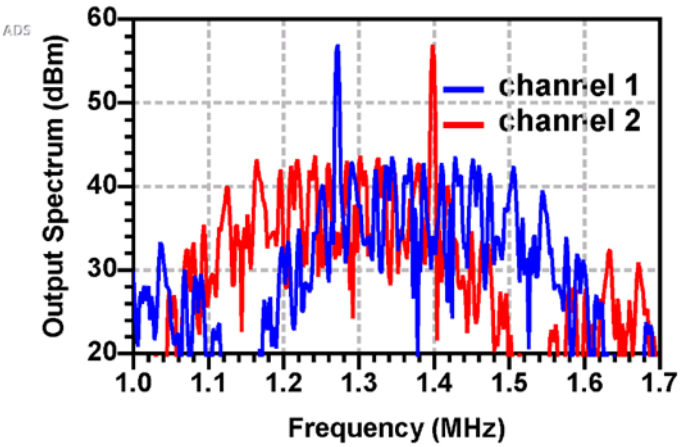

Figure 6-19: Step 4: Output spectrum of 2×1 radar architecture including baseband, frequency conversion stage based on Hartley architecture, Tx IF stages, Tx push-pull architecture and Rx RF LNA stages.
fb,ch1 = 1.272 MHz, fb,ch2 = 1.398 MHz.

The detection performance is further diminished by the addition of the two low-noise amplification stages. Even though the detection error is still very low, this shows that bandpass filters have a strong impact on the signal integrity, unlike lowpass filters which does not seem to impact the detection (cf. Step 2). Note that the output power is very high because the channel attenuation has not been included yet.

6.3.1.5 Step 5: Consider the Rx IF low-noise amplification stages

The last Rx stage comprises a low-pass filter to eventually suppress the remaining spurious signals such as the image frequency triggered by the second-stage down-conversion, as well as a low-frequency LNA to bring the signal power level to required sensitivity (Figure 6-20).

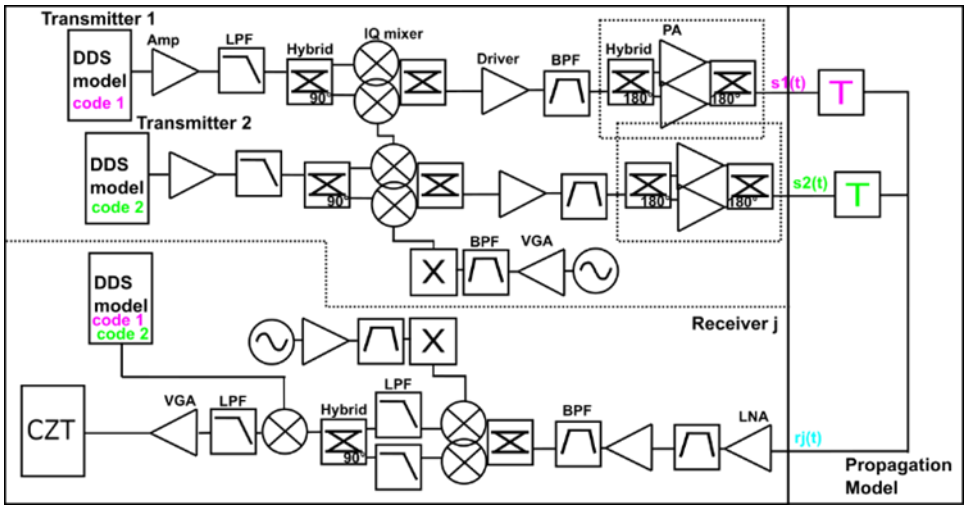

Figure 6-20: Step 5: Block diagram of 2×1 radar architecture including baseband, frequency conversion stage based on Hartley architecture, Tx IF stages, Tx push-pull architecture, Rx RF LNA stages and Rx IF LNA.

Figure 6-21 shows that including an IF low-noise amplification stage comprising an ideal LNA and an ideal lowpass filter does not affect the quality of the detection: both spectra present a clear Dirac impulse with the same beat frequency as in the previous stage. This gives us more confidence that bandpass filters are the major limiting factor for CDM-based intra-pulse phase-modulated FMCW radar architecture.

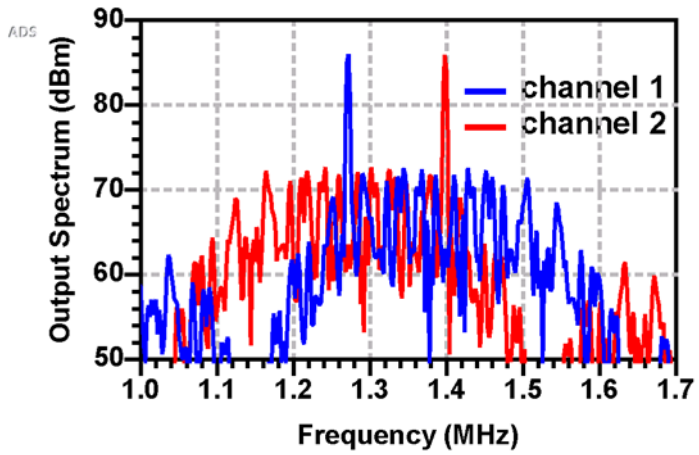

Figure 6-21: Step 5: Output spectrum of 2×1 radar architecture including baseband, frequency conversion stage based on Hartley architecture, Tx IF stages, Tx push-pull architecture, Rx RF LNA stages and Rx IF LNA.
fb,ch1 = 1.272 MHz, fb,ch2 = 1.398 MHz.

6.3.1.6 Step 6: Consider the complete ideal propagation model

The previous simulations used until now simple time delay blocks to model the propagation. These delay blocks accounted for the time of travel to and from the target. In this last simulation step, we use a detailed modelling for an ideal radar propagation model (Figure 6-22). It features:

- Antenna model including the antenna gain, the loss triggered by the transition PCB to waveguide and the change of impedance from 50 Ohm, characteristic impedance of the system to 377 Ohm, characteristic impedance of air
- Pathloss in vacuum
- Time of travel in vacuum
- Reflection on the target

This investigation will show whether the propagation has an impact on the modulation and thereby, the detection ability of the proposed radar architecture. From the previous simulations, we expect that the propagation model should not impair the detection since all models have already been simulated: the antenna model consists in an attenuator and a linear 2-port network, the pathloss is modelled by an attenuator and the time of travel by a delay block.

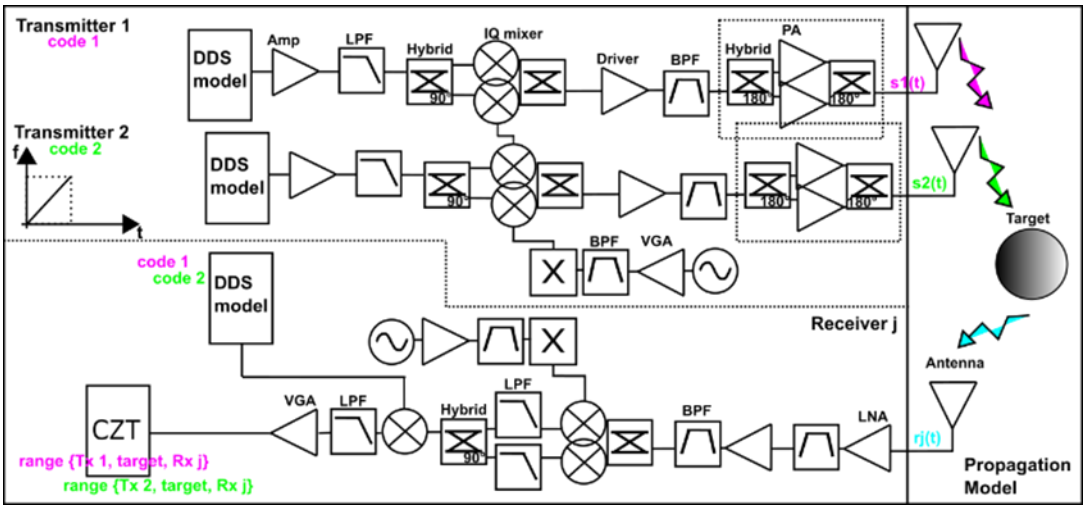

Figure 6-22: Step 6: Block diagram of 2×1 radar full architecture including ideal propagation model.

From Figure 6-23, we see that the ideal radar propagation model does not affect the signal integrity and the range can still be estimated with a 0.42% and 0.34% error for Tx 1 and Tx2 respectively.

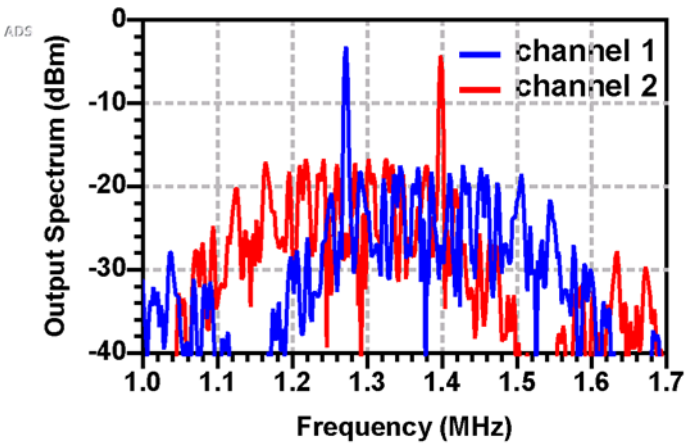

Figure 6-23: Step 6: Output spectrum of 2×1 radar full architecture including ideal propagation model.
fb,ch1 = 1.272 MHz, fb,ch2 = 1.398 MHz.

From this detailed and complete simulation, we also see that the output power falls within the specifications of an eventual ADC for a 10 m range. MIMIRAWE II radar receiver will however need further IF amplification stages in order to image object at longer ranges.

6.3.2 Impact of low-order bandpass filters

We ran one simulation of a partial MIMIRAWE II architecture and disabled the bandpass filters (Figure 6-24). We compare the simulation results to the architecture including the bandpass filters to see if they impact the detection performance. The bandpass filters are of type Butterworth.

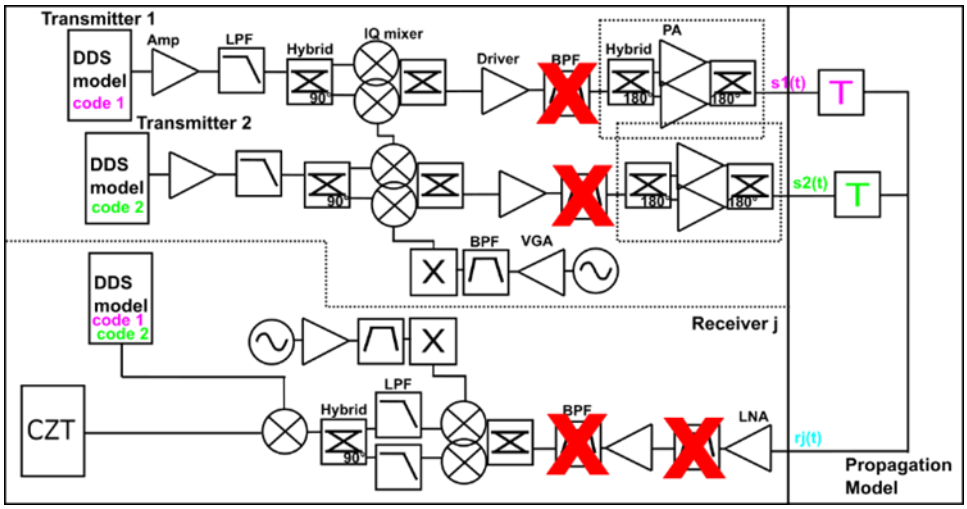

Figure 6-24: Block diagram of Step 3 with disabled BPF.

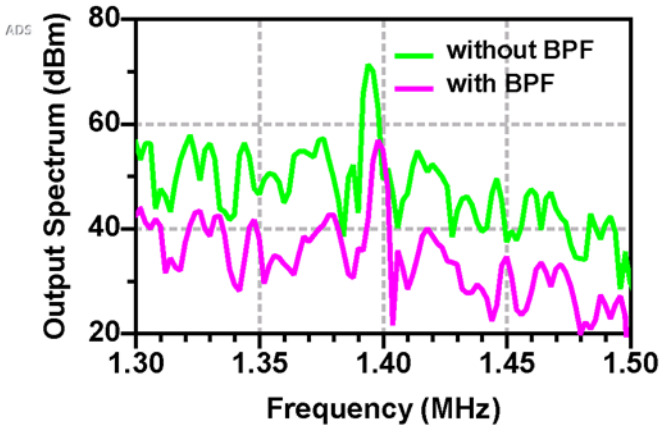

Figure 6-25: Comparison of spectrum with and without BPF when identifying channel 2.
fb,without BPF = 1.394 MHz, fb,BPF = 1.398 MHz.

Figure 6-25 shows that without bandpass filters, the detection performance is at their best. Indeed, it is possible to recover the target range from Tx 1 and from Tx 2 with an error of 0.11% and 0.05% respectively which correspond to the same performance of baseband detection. When adding the bandpass filters, the error becomes 0.42% and 0.34% respectively. The difference of power level is due to the loss of the bandpass filters.

The degradation of the range detection due to bandpass filters of types Butterworth or Chebychev is typically common to FMCW radar architecture: recent studies prove that group delay plays an important role on the quality of the range estimation [8],[9].

Figure 6-26 shows the output spectrum of MIMIRAWE I architecture as SISO radar without phase modulation (cf. Figure 6-2). The beat frequency is 1.271 MHz. This means that the range detection of CDM-based FMCW radars using intra-pulse modulation is not further impacted than classic FMCW. This also means that if a SISO FMCW radar prototype is validated, the exact same prototype can be used for our proposed MIMO FMCW radar architecture.

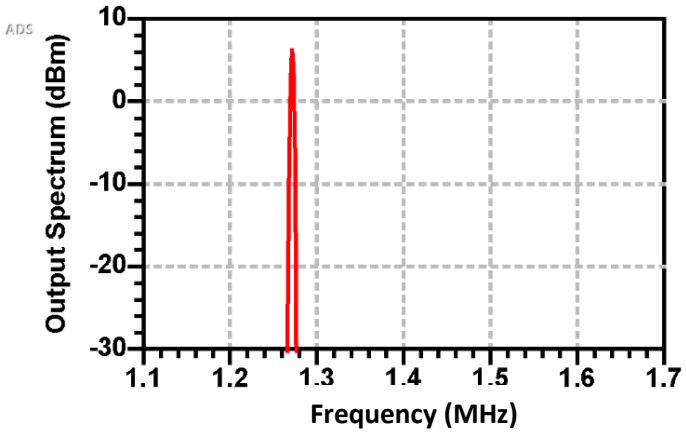

Figure 6-26: Output spectrum of MIMIRAWE I architecture.
fb = 1.271 MHz. We recognize the spectrum of the detection when the transmitted code and the reference de-ramping code are similar

An alternative architecture would be to replace the bandpass filters of the RF low-noise amplification at the receiver by attenuators. This is conceivable for MIMIRAWE II application, if we make the hypothesis that few or no other interferences will come from other instruments in space, outside of the one produced by the radar itself. And because we can guarantee a good spectral purity (low LO leakages, low second-order harmonics and suppressed sideband), we do not need to further filter the received signal. Attenuators remain necessary in order to decrease the reflections between the LNAs. They take less space than circulators and can be better integrated as bandpass filters. The power which will be loss due to the attenuation can be

accounted for the power which would have been loss by the bandpass filters due to insertion loss.

6.4 Summary and remarks

In this Chapter, we proceeded step by step in order to further demonstrate the feasibility of CDM-based intra-pulse phase-modulation applied to MIMIRAWE II radar system, a 90 GHz 8×8 FMCW radar architecture of 16 mm-range resolution. For computation reasons, we limited the investigation to a 2×1 MIMIRAWE II channel subset. We used ideal components but realistic frequency parameters: the baseband is [1..10.5 GHz], the carrier is [85..94.5 GHz], the bandwidth is 9.5 GHz and the pulse duration is 500 µs. For the sake of simplification, the transmitted chirps were coded in a pure analog approach.

We simulated on ADS the radar architecture under ideal conditions. We demonstrated that it was possible to recollect the ranges from the different transmitters, by modulating the phase of the different transmitted chirps by Gold codes, then proceeding to the classic de-ramping using coded chirp from Tx 1 to identify the channel 1, and from Tx 2 to identify channel 2. The results were particularly promising as the channel identification could be successfully performed with minor range estimation error. Both channels could we identified with a maximum of 0.42% on the range, and a 13 dBc peak-to-sidelobe ratio, which testifies of an excellent signal integrity. The integrity can further be decreased by choosing codes with better orthogonality. The results are easily scalable to a 8×8 radar as each Tx will have different quasi-orthogonal codes and each Rx will follow the same behaviour.

We saw that the only limiting factor of CDM-based intra-pulse phase-modulated FMCW radar architectures were the bandpass filters which deteriorate the detection. This is typical for FMCW radars and the proposed CDMA-based MIMO architecture is not more impacted than classic FMCW architectures. Without the use of bandpass filters, the range can be estimated with an error less than 0.11%.

We saw that high-pass filters and lowpass filters did not impair the detection, although of same type because the group delay accounts for the impairment of the performance. Such as classic FMCW architectures, real devices which also have a group delay will also strongly impair the detection performance of the multi-channel radar.

The general results show that the proposed MIMO architecture is a good radar candidate for space application.

6.5 To go further

A future work could evaluate the impact of the nonlinearity of amplifiers. It is expected that it should not impair the detection as the addition of mixers which are by definition nonlinear did not impact the detection.

It is crucial to simulate a close-to-reality simulation campaign with components modelled with the Wiener-Hammerstein model. This investigation was carried out at lower frequency and narrower bandwidth, on a 2×1 35 GHz FMCW radar of 1 GHz-bandwidth but unrealisable due to computation limitation at the time of development.

Another way of coding the FMCW signal is using classic pulse modulation, where $T_c = T_r = T$ reducing the code rate to $1/T$ Hz. Detection using intra-pulse modulation should need only one coded chirp of 500 µs to be able to recollect the signal, unlike pulse modulation which requires N_c×500 µs to be effective, which uses a considerable time- and energy-resource. However, classic pulse-modulation benefits from its simplicity, as the coding rate is much lower than for intra-pulse modulation – here 2 kHz, and can be achieved more easily. Due to substantial memory resource requirements for the simulation of the system, the results for pulse modulation could not be completed.

Chapter 7

Transmitter circuit design and measurements

This Chapter presents the development and testing of a low-cost 35 GHz transmitter modular prototype based on our proposed architecture for validation. The proposed transmitter architecture is recalled on Figure 7-1. From detailed simulated system results (cf. Chapter 4), the transmitter module (Tx) is expected to deliver a high-power output up to 34 dBm at 35 GHz with a high SFDR – conversion image rejection of 53.5 dBc, a spectral purity less than -45 dBc in band, and less than -100 dBc out-of-band.

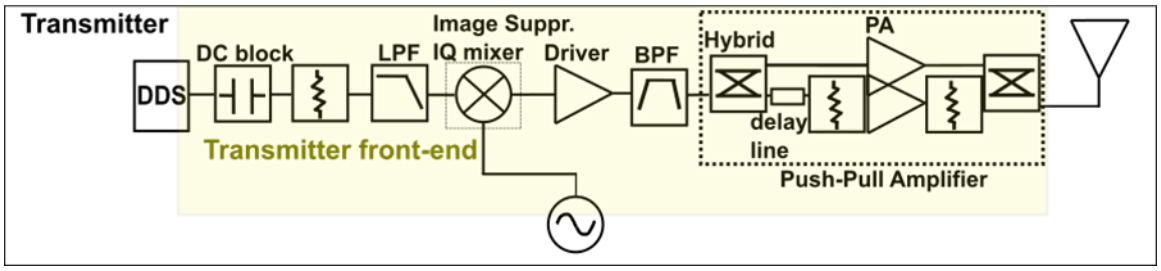

Figure 7-1: Proposed transmitter, highlighted the implemented front end.
All the components of the front end are commercial SMD, excepted the filter and the 180° hybrid which are designed in-house in microstrip. The delay line accounts for the artificial compensation of the phase balance on-board (cf.Section 3.5.3.)

7.1 Design rules and fabrication

The Tx module is designed on Rogers RO4350B substrate, of dielectric constant 3.48 and loss tangent 0.0037, both measured at 10 GHz [45]. The substrate is 0.254 mm (10 mil)-thick. The thickness of the copper conductor layers is 35 µm (1 Oz). Both top and bottom copper layers are covered with 0.8 µm-thick Electroless-Palladium-Immersion-Gold (EPIG) finish. The printed circuit boards (PCB) are milled to the edge, and copper burrs are removed to ensure the electrical contact of the connectors. The plated through holes (vias) have a diameter of 254 µm with a 75 µm-thick annual ring. The Tx module utilizes commercial components in surface mount technologies, excepted for the RF bandpass filter and the 180° hybrid which we designed on

microstrip. Solder mask is commonly placed on top of DC and RF lines to prevent solder paste from flowing arbitrarily into the lines, and to guarantee the repeatability of results. However, solder mask can trigger significant distortion at high frequencies. We surround the component landing footprints by a thin band of solder mask of 200 microns, which is significantly smaller than the operational wavelength 8.5 mm so as not to affect the overall operational frequency (cf Figure 7-2). Thereby we guarantee result repeatability while avoiding potential frequency distortion.

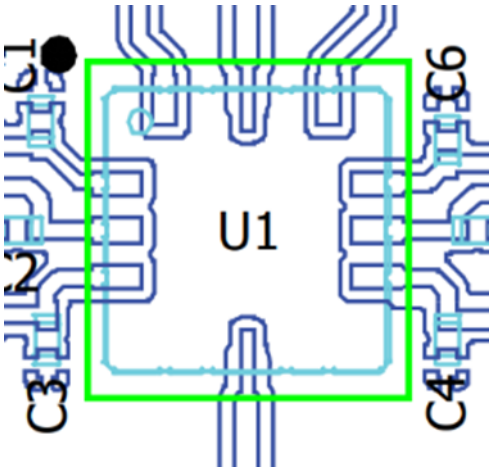

Figure 7-2: Example of solder mask (green) on PA HMC7229L6.
A 200 µm-thick band of solder mask is placed 20 µm away from the landing pads. Drawing was taking from datasheet [23].

The transmitter prototype is fabricated externally. The manufacturer guarantees a design tolerance of ± 17.5 µm for the conductor line width, and a tolerance of ± 17.5 µm for the conductor spacing. The drilling tolerance is between -50 µm and +100 µm.

Two single transmitter modules with SMT drivers HMC635LC4 from Analog Devices were fabricated. Several components of each board were defective and could not be safely replaced. Therefore, we characterized instead a modular transmitter as shown in Figure 7-3.

The layout was designed on Keysight ADS. We drew on the recommended footprints from the manufacturers [21]-[23],[25]-[31] and optimized the footprints to integrate them on the proposed PCB layout, considering spatial constraints. The circuit design analysis is presented for the single transmitter module and similar for the modular transmitter. We inspect four critical points particularly. Firstly, we symmetrize the Hartley architecture used in the up-conversion to allow either upper-sideband or lower-sideband suppression. Secondly, two baluns are needed to satisfy the unbalanced input requirements of the upconverter; it is fundamental to verify that the lines at the converter input do not trigger extra unbalance at the risk of deteriorating its

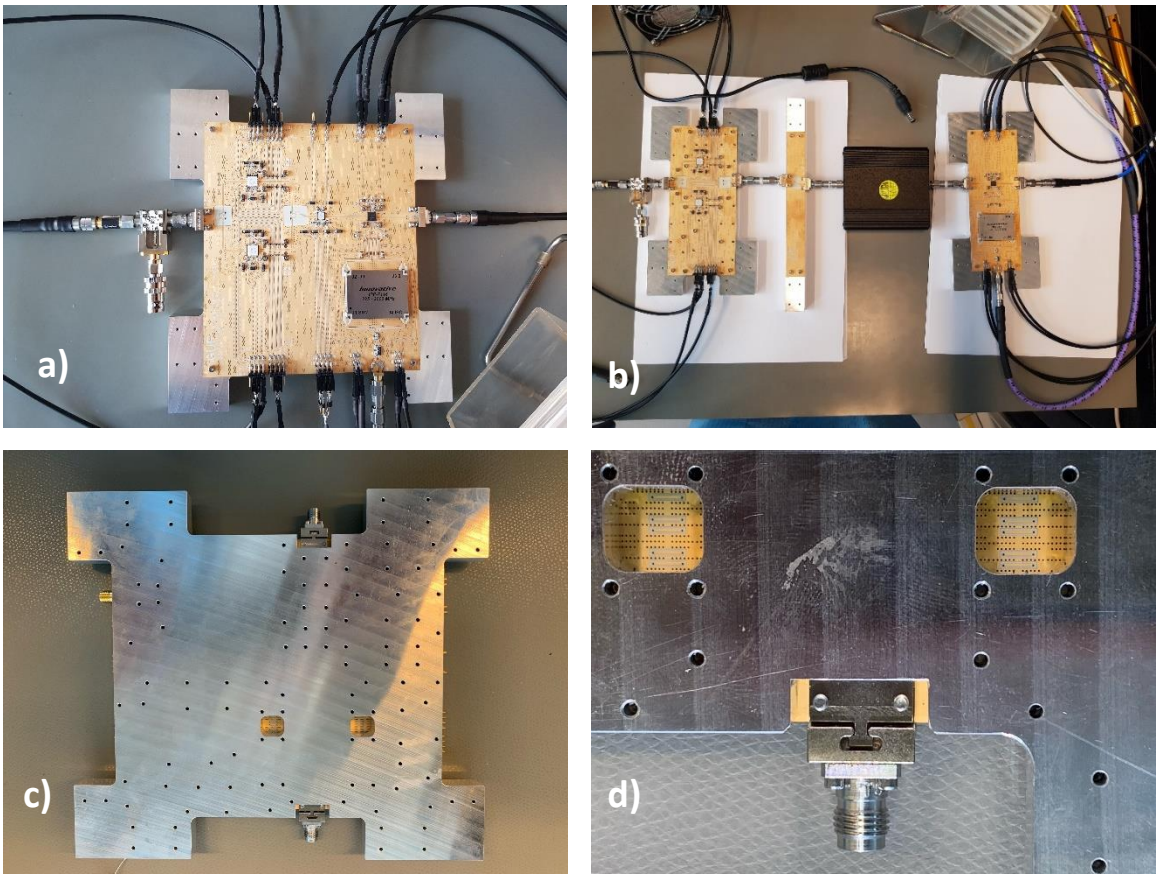

Figure 7-3: Transmitter: a) defective single module was replaced by b) an assembly of sub-systems modules; c) Tx backside; d) Zoomed backside

The chain includes an up-converter, a driver, a BPF and a push-pull amplifier from right to left. The aluminium plate is open under the DC tunnels of the push-pull. The measurements of the modular transmitter should give a close expectation of the characterization of the single transmitter module.

performance. Thirdly, the microstrip design of the 180° hybrid and the BPF necessitates several transitions microstrip to ground coplanar waveguide (GCPW) and we make sure to optimize their loss. Finally, in our design, the power amplifier (PA) HMC7229LS6 from Analog Devices used for the push-pull architecture needs a DC biasing on both side of the chip [25]. Since two 180° hybrids and two PAs are imperative for the push-pull architecture, the DC lines are tunnelled under the RF lines in order to have all the DC biasing at the edge of the PCB as displayed in Figure 7-3.

At the time of development, few SMT components were available in the 33-36 GHz range of the Ka-band. Therefore, the selected up-converter and the amplifier featured in the transmitter perform outside their specs. In addition, we need the transmitter to operate in the lower sideband because of constraints due to the LO and the receiver chains of the radar. Because the lower sideband performance was not specified by the manufacturer [21], it will be crucial to characterize it.

7.2 Circuit design and simulation

The transmitter board is fully designed using Keysight ADS. We use GCPW as required in [21]-[23],[25]-[31] and microstrip for the filter and the 180°hybrid. Thus, the EM simulation considers the top and bottom copper layers, the RO4350B substrate and the via layer. The surrounding dielectric is air (see Figure 7-4). A way to emulate a GCWG excitation during EM-simulation is to proceed as follows: we add a piece of ground 20 µm away from the edge of the line laterally; we place a via very close to the edge, we position one port on the ground and one port on the signal line; we couple the ports and apply a negative polarity to the ground port and a positive polarity to the signal port (see Figure 7-5). The resulting port is a port with reference to top ground layer. We use this method to EM-simulate the essential parts of the transmitter module.

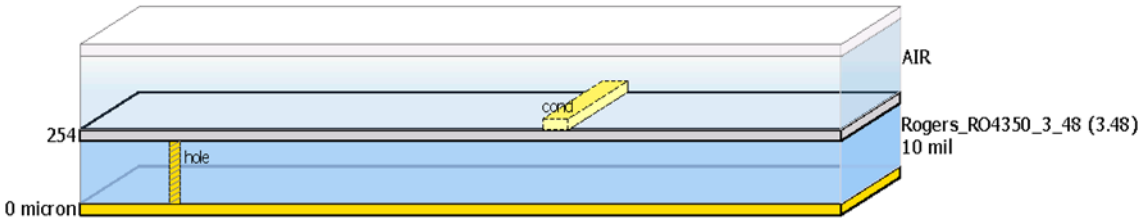

Figure 7-4: Layout structure of the simulated circuits

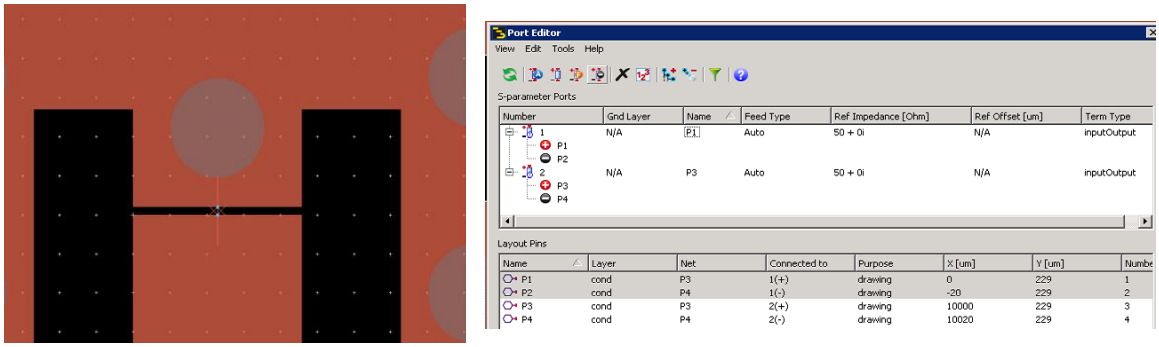

Figure 7-5: CGWG excitation of transmission lines: layout and port settings

7.2.1 Single sideband up-conversion

The up-conversion, based on Hartley architecture for image suppression, uses a sub-harmonic mixer TGC4546-SM from Qorvo, coupled with a 90° hybrid coupler IPP-7116 from Innovative Power Products and two baluns NCS1-112+ from Mini-Circuits. In order to use the full capability of the chip, we symmetrize the 90° hybrid input. Figure 7-6 shows the symmetrizing of hybrid and recalls the components connection.

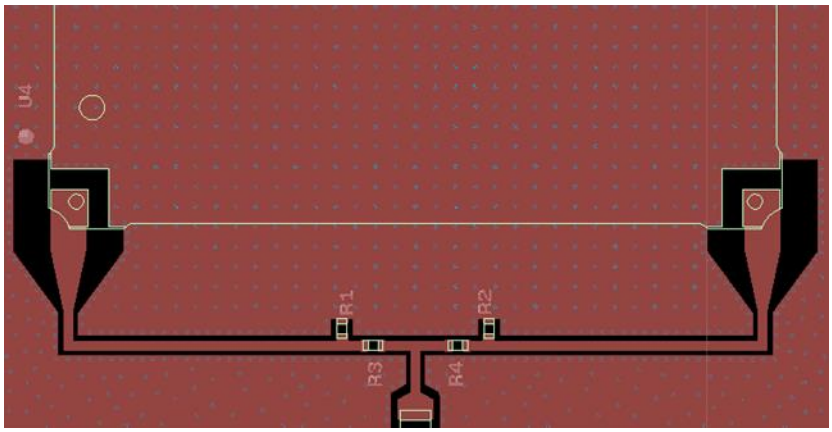

Figure 7-6: Symmetrizing of the 90° hybrid input.
Port J3 of IPP7116 is linked to pins 11-12 of TGC4546 and J4 is linked to 9-10. LSB conversion when R2 is 50Ω, R3 0Ω and R1, R4 unmounted. USB conversion when R1 is 50Ω, R4 0Ω and R2, R3 unmounted (cf. Section 3.4). We connect the balun as recommended in [21]

To validate the feasibility of the symmetrizing, the balun input is EM simulated from DC to 2 GHz. We replace R4 by a piece of signal line, we leave R2 and R3 open, and like in Figure 7-5 (right), we create a non-calibrated clustered port of reference impedance 50 Ω for R1 (Figure 7-6). The EM simulation results are then exported to schematic and simulated using an ideal 50 Ohm resistor. The results show that the signal is actually transmitted to the hybrid input port, and that the isolated port is correctly terminated by 50 Ω (Figure 7-7).

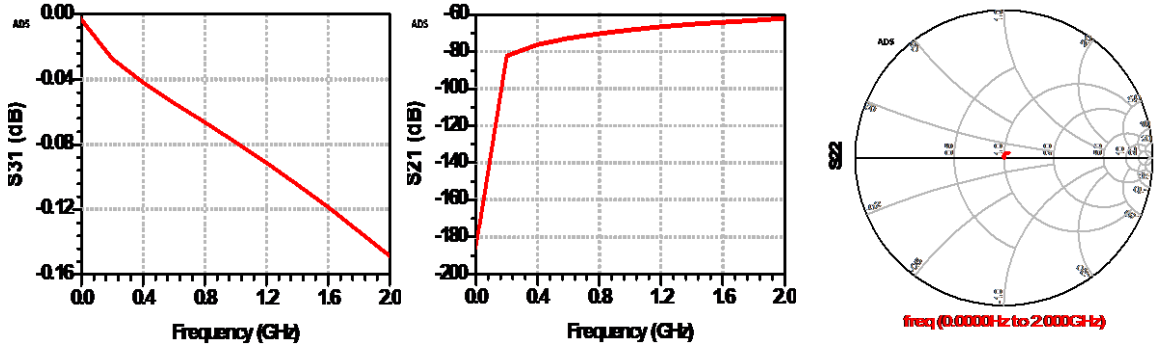

Figure 7-7: Simulation results of the hybrid-input.
We see that one port of the coupler is correctly connected to the IF signal line, the loss is less than 0.2 dB (S21). The other port is correctly isolated from the IF signal line with an isolation is >60 dB (S31),), and terminated by 50 Ohm (Smith Chart of S22).

7.2.2 Upconverter input

The TGC4546-SM component requires the IF input to be unbalanced [21]. Because the phase balance is particularly critical to the performance of the single-sideband conversion, we verify

that the signals transmitted from the baluns outputs to the up-converter inputs do not undergo significant phase unbalance between the different IF paths. The structure is EM simulated from DC to 3.5 GHz using ADS. The simulation includes the DC biasing environment from TCG4546-SM chip located in the close vicinity. Due to limited computation performance, some vias of the DC path are replaced by a line of 'hole' (via) layer. Thereby the whole structure can be fully simulated. The simulation results are exported to schematic (cf Figure 7-8), and resimulated using ideal capacitors and inductors as specified on the component datasheet [21].

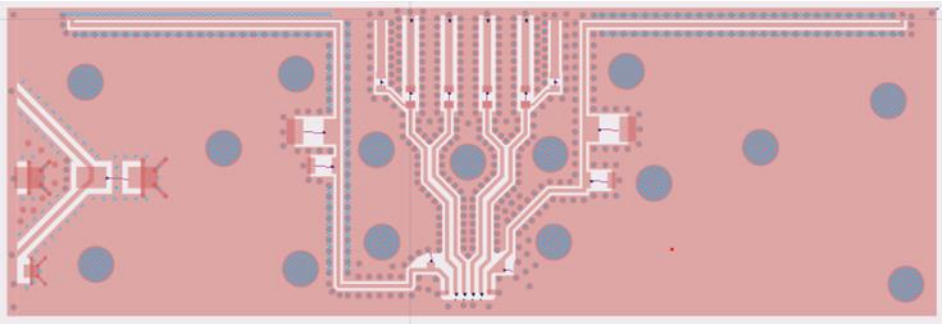

Figure 7-8: Simulation of IQ mixer input signal after export of EM simulation results to schematic when the DC lines necessary for LO nulling are connected to the IF signals.

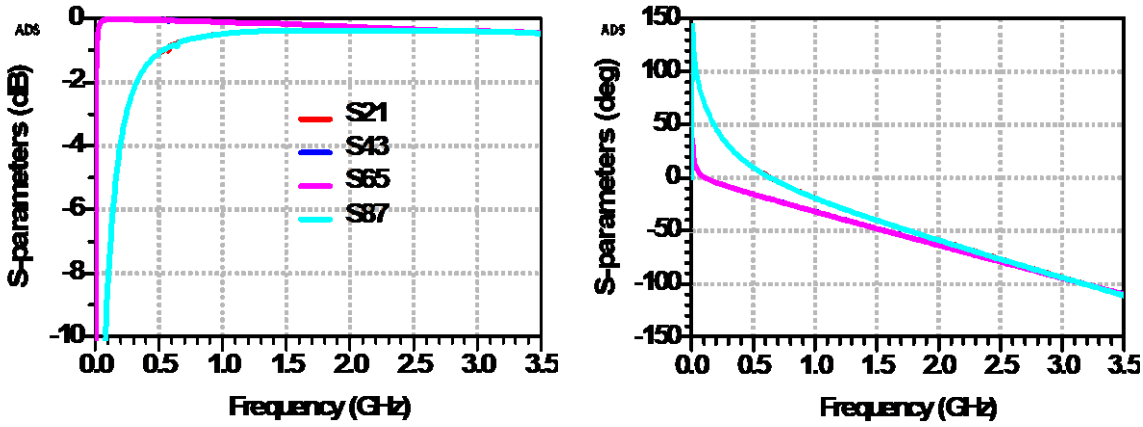

Figure 7-9: Simulation results of the IQ mixer input, when the DC lines are connected to the IF signal lines.
Some unbalance is triggered by the outside branches.

The results displayed in Figure 7-9 show that the proposed layout does not bring additional unbalance between the difference IF signal paths. Please note that the two branches linking DC sources to two IF paths will bring a slight amplitude and phase unbalance at the lower frequencies. However, these branches are necessary for LO nulling technique [21] and the induced unbalance is probably counterbalanced inside the chip. Figure 7-10 and Figure 7-11

illustrate the simulation results when the DC lines are not connected to the IF lines. All lines are perfectly balanced in amplitude and phase.

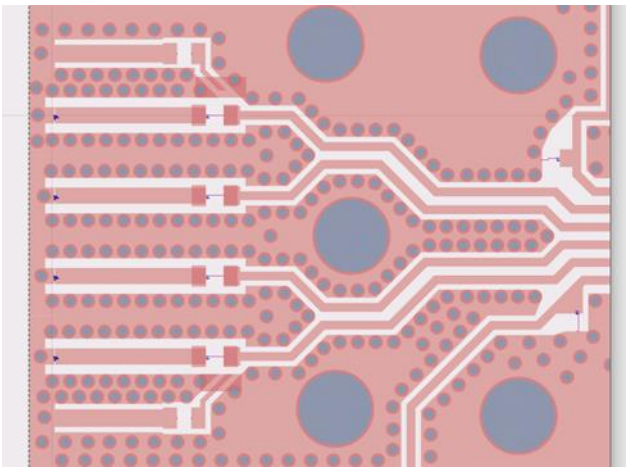

Figure 7-10: Simulation of IQ mixer input signal after export of EM simulation results to schematic when the DC lines necessary for LO nulling are disconnected to the IF signal lines (zoomed).

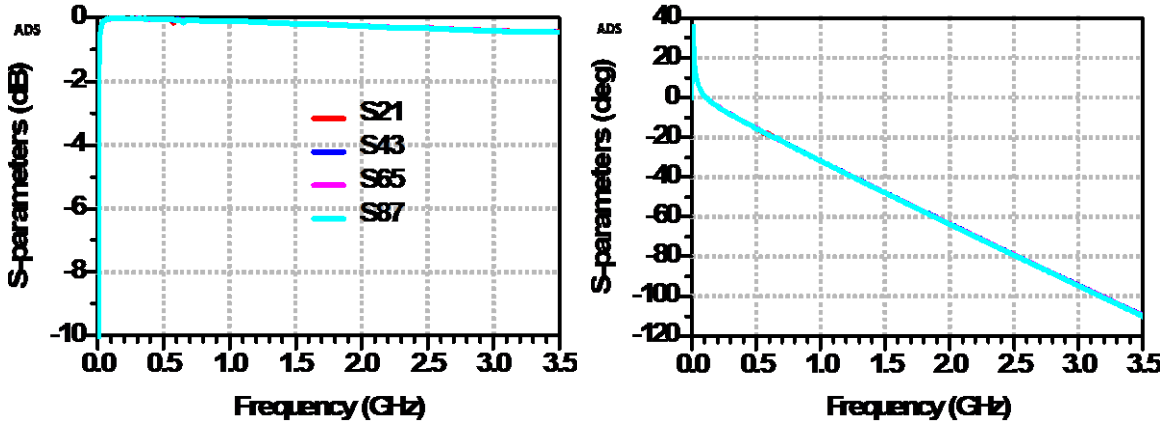

Figure 7-11: Simulation results of the IQ mixer input, when the DC lines are disconnected to the IF signal lines.
No extra unbalance is triggered.

7.2.3 Replicability of millimeter-wave microstrip filters using parallel coupled-lines

The proposed radar architecture comprises one single 3rd order bandpass filter (BPF) to decrease the level of spurious signals such as local oscillator leakages, image frequency or unwanted harmonics. The BPF also helps reducing the amount of reflection between the driver

and the push-pull. We investigate the replicability of microstrip bandpass filters before implementing them in our radar system.

7.2.3.1 Context

Microstrip BPFs have the advantage of being compact, lightweight and are compatible with SMD components, but the design becomes challenging at mm-wave frequencies. Low insertion loss (IL) necessitates thin and low-loss substrates such as those based on LTCC technologies [46] or Rogers RT 5880 [47],[48]. Mm-wave coupled line filter dimensions decrease to sub-millimetre dimensions, which makes it difficult to implement via holes necessary for short-circuited lines [46]. Furthermore, the spacing between the lines reduces greatly with respect to increasing fractional bandwidth. In [47], the authors propose a wideband BPF design solution with minimum 100 µm spacing which is realizable. However, the architecture including the matching network is relatively complex, especially that mm-wave BPF design is sensitive to length variations (Figure 7-12).

As an alternative, we propose a simple bandpass filter design using parallel open-circuited coupled lines on Rogers RO4350B substrate. The dielectric constant is 3.48 and the loss tangent is 0.0037, both measured at 10 GHz. The thickness of the substrate is 0.254 mm with 35 µm-thick copper conductor layers. To investigate the manufacturing robustness of the filter, seven replicas have been fabricated externally and characterized. All replicas are built on the same substrate lot. The manufacturer guarantees a design tolerance of 80% of the filter dimension, the conductor spacing tolerance is 30%. We want to show that the proposed and conventional parallel coupled-line filter is realizable and replicable at mm-wave frequencies. This study is essential to ensure that the filter works as expected once integrated in the radar transmitter.

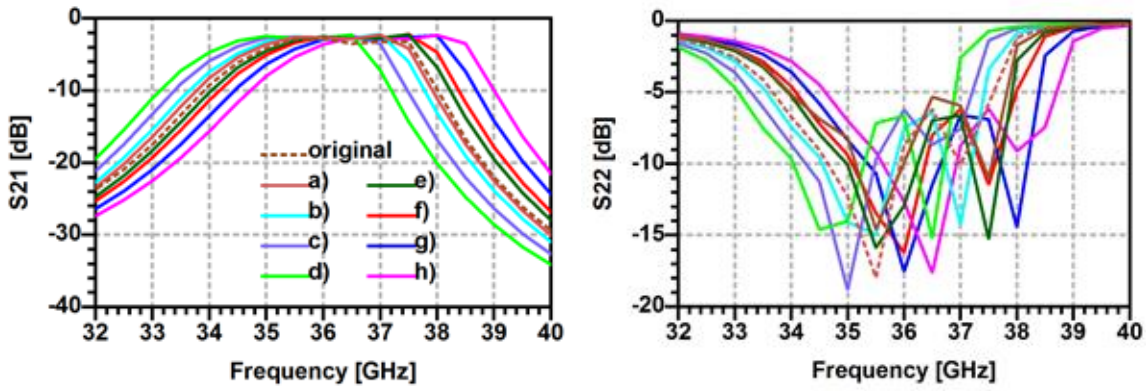

Figure 7-12: Frequency response shift due to length modification for S21 and S22.
The length of each coupled line has been increased by a) 5 µm, b) 10 µm, c) 20 µm, d) 30 µm, and decreased by e) 5 µm, f) 10 µm, g) 20 µm, h) 30 µm from the original. A shift of 50 µm is typical error when manufacturing.

7.2.3.2 Filter design

Let us consider a BPF of order N, of geometric center frequency $f_0 = \sqrt{f_1 f_2}$ and passband frequencies f_1 and f_2. The dimensions of the coupled-line BPF are determined using the classic two-step design equations derived in [49].

First the products of the $J_i Z_0$ the admittance of the i^{th} inverter ($i = 1..N+1$) are calculated for the 1st coupling $J_1 Z_0 = \sqrt{\Delta\pi/2g_1}$, for the n^{th} coupling $J_n Z_0 = \Delta\pi/2\sqrt{g_{n-1}g_n}$ and for the last coupling $J_{n+1} Z_0 = \sqrt{\Delta\pi/2\, g_n g_{n+1}}$. These products are function of the fractional bandwidth $\Delta = (f_2 - f_1)/f_0$ and the filter prototypes g_i. Then are derived the even mode Z_{0e}^i and the odd mode Z_{0o}^i characteristic impedances for each coupled line i: $Z_{0e}^i = Z_0(1 + J_i Z_0 + (J_i Z_0)^2)$ and $Z_{0o}^i = Z_0(1 - J_i Z_0 + (J_i Z_0)^2)$ respectively.

The physical dimensions of the coupled lines can be approximated and optimized using CAD software.

7.2.3.3 Filter simulations

The methodology presented above is applied to design a 3rd order Chebyshev BPF using parallel open-circuited coupled lines with 0.5 dB passband ripples. Given a fixed order, Chebyshev filter has the advantage of having the sharpest cutoff among the classic filters [49].

The characteristic impedance is 50 Ohm. The centre frequency is 36.3 GHz; the fractional bandwidth is 10%. The filter is overdesigned to 40 GHz to compensate the frequency shift due the fringing fields at the open-circuited stubs.

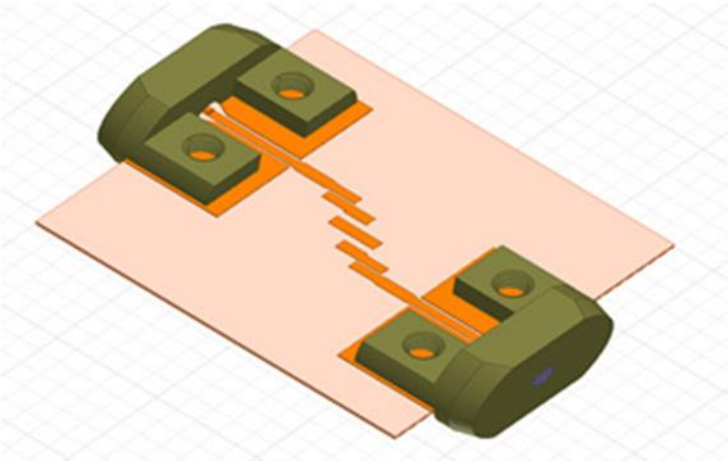

Figure 7-13: Coupled-line bsand-pass filter.
The outer coupled lines have a width of 417 µm, a spacing of 109 µm and a length of 1173 µm. The inner coupled lines have a width of 509 µm, a spacing of 359 µm and a length of 1136 µm. The filter is connected to the pads of the Hirose HK-LR-SR2 connectors.

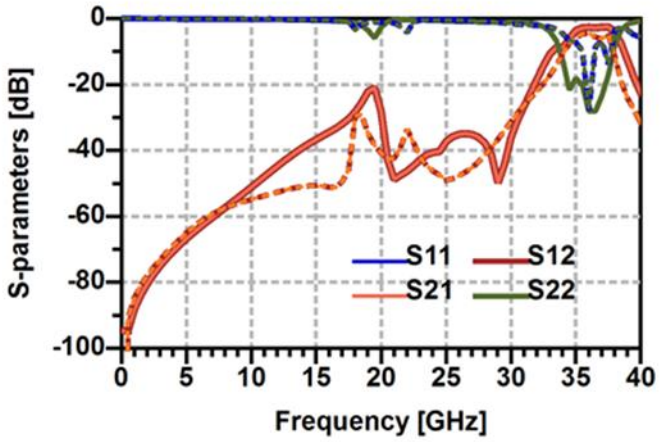

Figure 7-14: Proposed filter simulations
using Ansys Electronics (solid lines) and Keysight ADS (dotted lines)

The layout including the filter, 50 Ohm transmission lines and the landing pads of 2.9 mm SMA connectors is pre-designed and simulated using Keysight ADS. A 3D EM simulation comprising the above-mentioned filter layout as well as 3D-drawing of the connectors is performed with ANSYS Electronics. In this simulation, the length of the 50 Ohm line and the tapered transition between the filter and the transmission line, as well as between the transmission line and the coplanar waveguide (CPW) structure of the connector footprint are optimized.

Figure 7-13 exhibits the complete design of the filter. The smallest spacing is 109 µm, and the smallest line width is 330 µm, which are reasonable for manufacturing. The SMA connectors are Hirose HK-LR-SR2. Because they are defined from DC to 40 GHz, the analysis is operated within this frequency range.

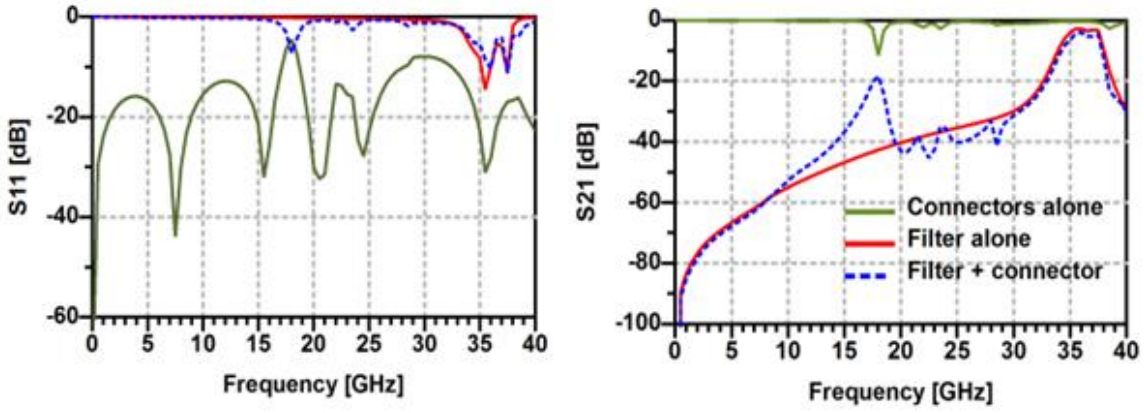

Figure 7-15: ADS simulation of S11 (left) and S21 (right) comparison between a thru-line (connector landing pads and tapered 50 Ohm transmission line), the filter alone and the full layout comprising the filter with the connectors pads

Figure 7-14 displays the performance of the filter simulated on ADS and Ansys Electronics. For the whole filter, the IL = 2.5 dB with a 9.9% fractional bandwidth 34.5 - 38.1 GHz, and a return loss > 8 dB. The simulation results are satisfactory for our application where the reflections are more critical than the insertion loss as the filter is integrated between two amplifiers operating in nonlinear regime.

Note that the ripples present in the stopband are due to the connector landing pads, as highlighted in Figure 7-15. This frequency corresponds to the main notch. The plot result indicates that there is radiation at the transition CPW to microstrip.

7.2.3.4 Filter measurements

Seven replicas of the microstrip filter are fabricated on the same substrate lot (see Figure 7-16). For filters 1, 2, 3 and 6, the connectors landing pads are chosen to be placed at the very edge of the board. Thereby the tight design distance from the edge of PCB to the connectors via holes, recommended by the manufacturer is respected and the connectors are sure to be fixed correctly. However, dicing the PCB can generate copper burrs. In order to investigate the potential consequences of dicing process, the board is cut 200 microns away from the connector landing pads edge for filters 4, 5 and 7 (Figure 7-17).

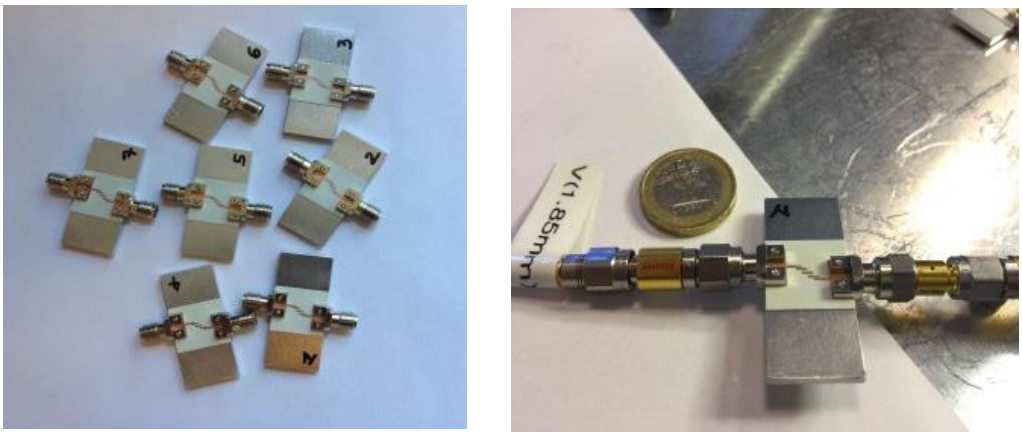

Figure 7-16: a) Filter replicas b) Filter measurement setup

The seven filter replicas have been measured with vector network analyser Anritsu ME7808B under the same calibration of the instrument, using calibration kit model 3652. We compare the seven replicas to each other and to the simulation results (Figure 7-18). There is no substantial distortion of the frequency response as seen in Figure 7-12. To investigate further the feasibility and replicability of the filter, for each filter replica the centre frequency, the fractional bandwidth, the insertion loss and the return loss are determined, respectively. Then, for each of these parameters the average (AVG) and the standard deviation (SD) are calculated and summarized in Figure 7-19.

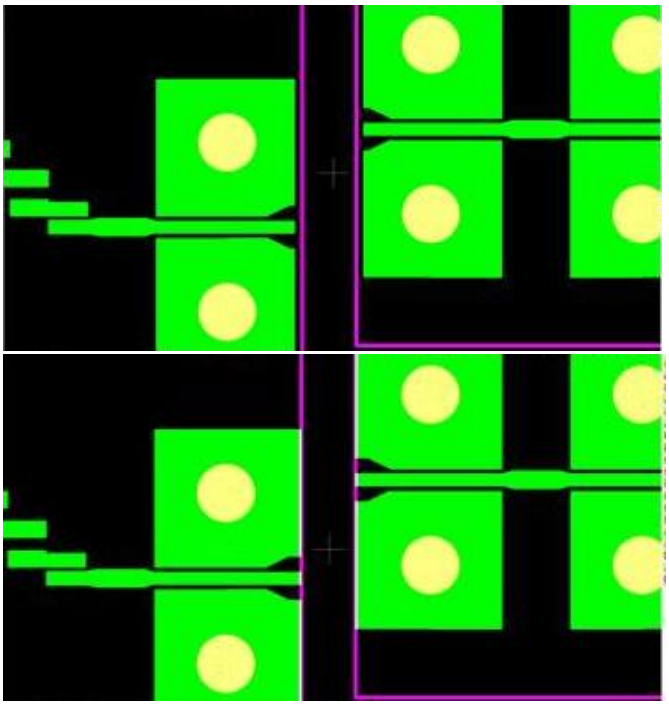

Figure 7-17: In purple the PCB outline, in green the copper: (top) outline at the border of the connectors landing pads, (bottom) outline 200 microns away from the connectors landing pads

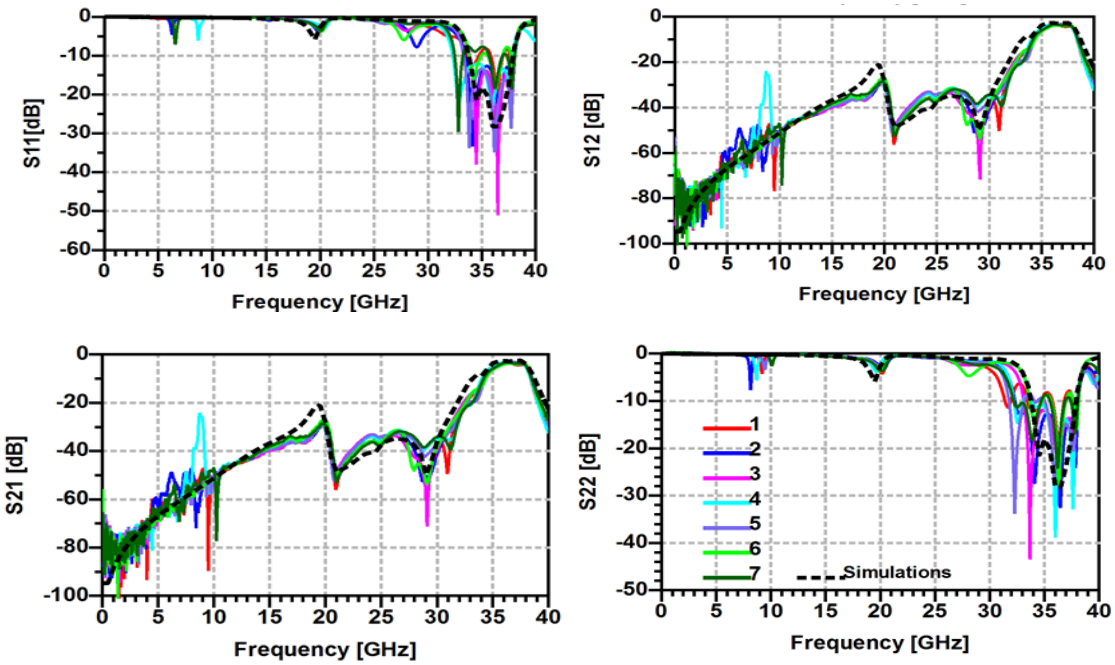

Figure 7-18: Simulation and measurements results.

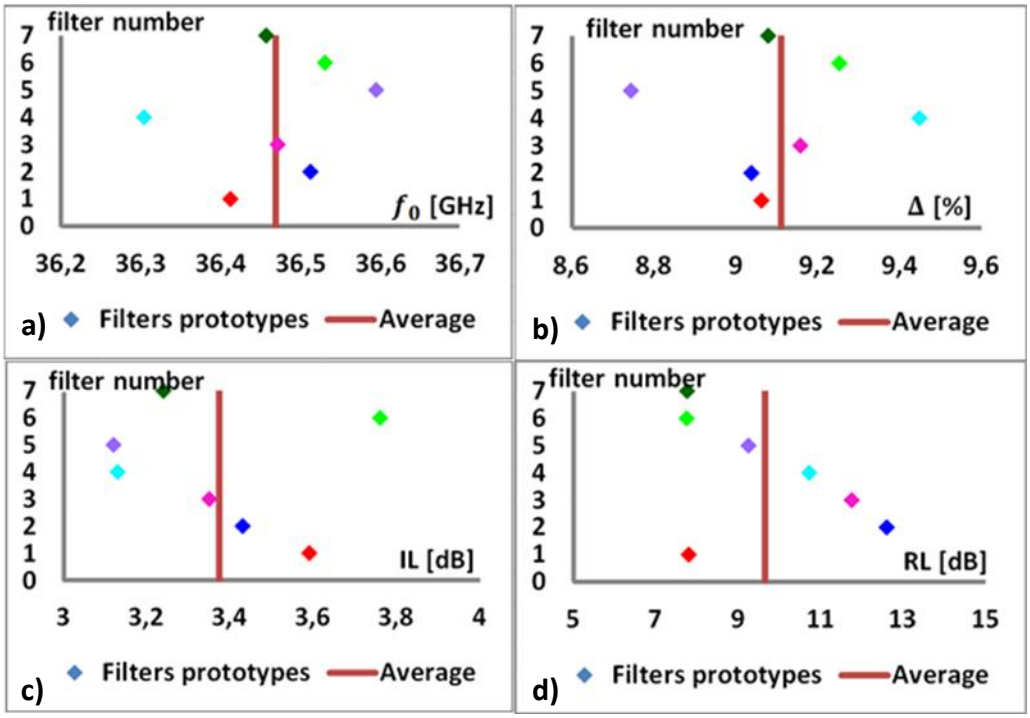

Figure 7-19: Measurements results: Statistical comparison of the seven filters

a) the AVG center frequency is 36.51 GHz with SD = 0.09 GHz; b) the AVG fractional bandwidth is 9.1% with SD = 0.2%; c) the AVG insertion loss is 3.37 dB with SD = 0.24 dB; d) the AVG return loss is 9.66 dB with SD = 2.04 dB. For transmission parameters, filters 2, 3 and 7 are robust. There is no pattern with respect to reflection parameters. This demonstrates that the RL is sensitive to manufacturing. There is no conclusive impact regarding copper burrs

In Figure 7-19, filters 4 and 5 (with 200 µm extra spacing at the PCB edge) are deviating with respect to centre frequency, passband and insertion loss, unlike filters 1, 2 ,3. This could be due to a defect on the connectors contact to the PCB. However, it is difficult to conclude on this phenomenon, as filters 6 and 7 do not follow the trend of their fellow filters.

In Figure 7-18, in the stopband, a notch appears for filter 4. This is due to a poor electrical contact of the connector and disappeared during measurements when the connector is pressed towards the signal line. It may be due to a manufacturing error, as neither filter 5 nor 7 presents the same notches.

These general results are satisfactory and confirm the fine replicability for mm-wave coupled-line bandpass filters. which can now be safely included in our system.

7.2.4 Bandpass filter, 180° hybrid coupler and system integration

To the authors' knowledge, no SMT bandpass filter or 180° hybrid is available at 35 GHz at the time of development. Therefore, both components are designed on microstrip. Using this

technology, the components are low-cost, compact, lightweight and compatible with SMT devices.

7.2.4.1 Filter redesign

The replicability of millimetre-wave microstrip bandpass filters using parallel open-stub coupled lines is guaranteed. Therefore, we redesign a 3rd order 0.5 dB equal-ripple Chebyshev filter using parallel coupled lines on a 10 mil-thick RO4350B substrate within the specifications of the 35 GHz radar transmitter. The filter is over-designed at 38.5 GHz so that the characteristic impedance is 50 Ohm, the centre frequency is 35.5 GHz and the fractional bandwidth remains 10%. Figure 7-20 exhibits the filter dimensions. The filter alone is EM-simulated on ADS. The results show a passband from 34 GHz to 37 GHz. The fractional bandwidth is 8.5%. The insertion loss is less than 1.9 dB and the return loss is typically 8.5 dB (cf. Figure 7-21).

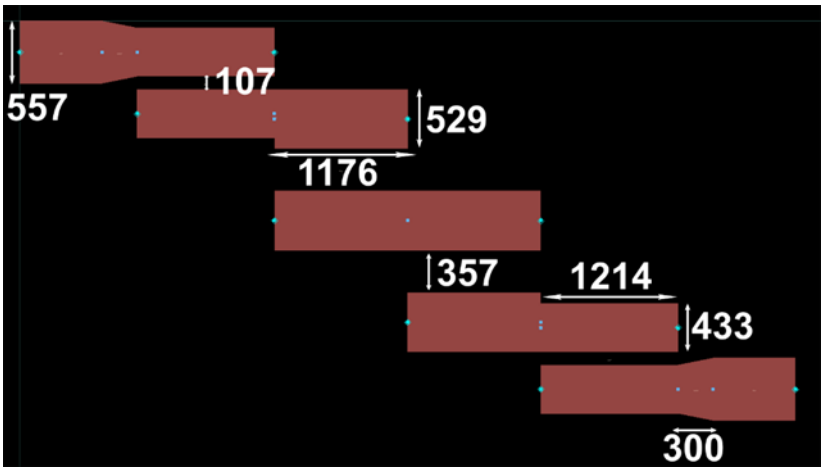

Figure 7-20: Bandpass filters dimensions in micrometres

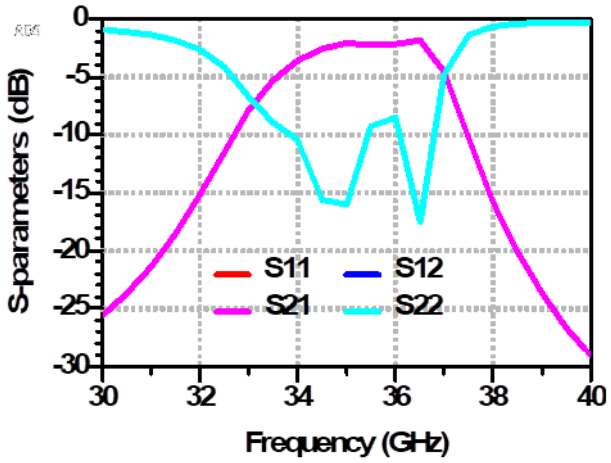

Figure 7-21: Simulation results of filter alone

7.2.4.2 180° hybrid

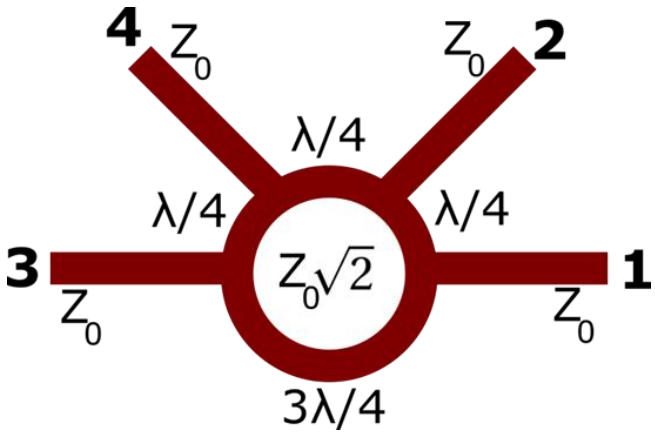

Figure 7-22: Rat race design formulas.

Two 180° hybrids are necessary for the push-pull amplifier architecture. A rat-race coupler has the advantage of being broadband, easy to design and has a good isolation between the input ports. The design formulas presented in [49] are recalled in Figure 7-22 and applied. The bended arms of the coupler are smoothened to guarantee broadband frequency. The isolated port (port 4) is terminated by 2 shunt 100Ω-resistors instead of a single 50Ω-resistor, so that the port is more likely to be terminated by 50 Ohm in case of poor resistor tolerance. The 50Ω-line is transformed into two parallel 100Ω-lines before the resistors footprint layout to improve the isolation. The width of the 100 Ohm lines is 118 µm, which complies with the design rules of the manufacturer. Figure 7-23 shows the rat-race layout after being EM simulated then exported to schematic. Figure 7-24 depicts the simulation results. The insertion loss on S_{21} is 1.4 dB. The isolation is 22 dB. The gain unbalance is less than 0.2 dB and the phase unbalance is around 3°.

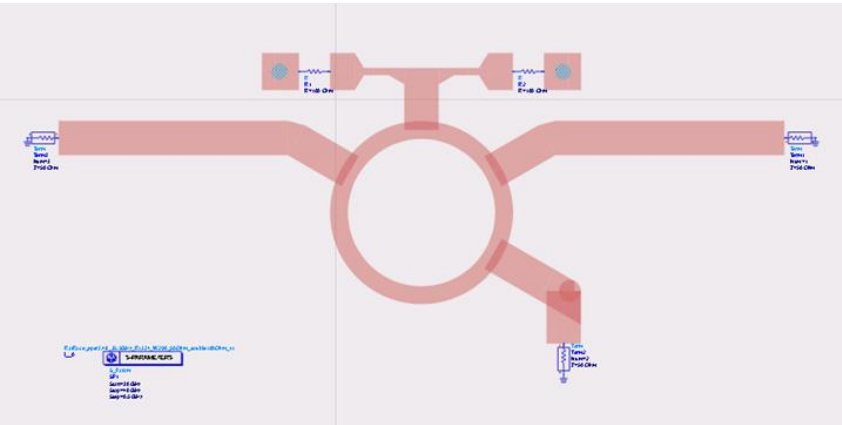

Figure 7-23: Rat race layout after export to schematic.
The ring thickness is 290 µm and the radius is 1271 µm.

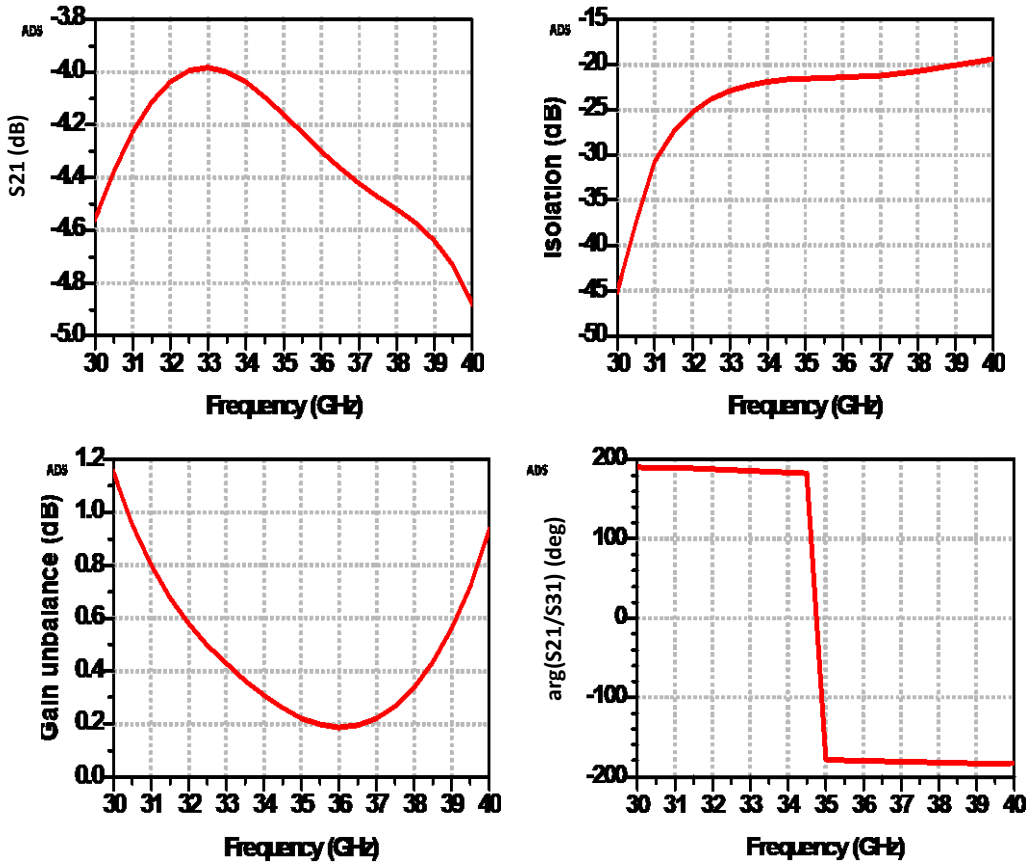

Figure 7-24: Simulation results of rate race alone.
In the 35-36 GHz band, the insertion loss |S21|+3dB is 1.4 dB, isolation (S23) 22 dB, gain unbalance dB(S21/S31) is 0.2 dB and phase unbalance arg(S21/S31)-180° is <3°.

7.2.4.3 Design integration

The microstrip input of the filter is connected to the GCPW output of the driver as seen in Figure 7-25. The transition includes a 50Ω GCPW line to a 50Ω microstrip. The signal line has 300 µm-taper. The GND is smoothened and a via is placed the closest possible to the transition. The microstrip output of the filter is connected to the microstrip input of the rat-race coupler (port 1) by a 1700 µm-long 50Ω line and a 300 µm-long taper. The arms of the rat-race coupler (ports 3 and 4) are also tapered to GCPW. To ensure that the surrounding ground of the GCPW Tx layout does not interfere with both microstrip filter and 180° hybrid, the ground is shifted approximately 5 times the filter largest dimension away from the rat-race coupler center.

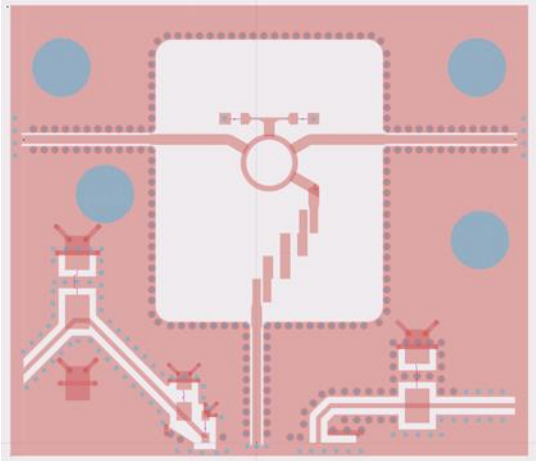

Figure 7-25: Filter and rat race layout after export to schematic.

The ensemble is EM-simulated including a part of the surrounding ground, as well as the capacitors of the drivers located in the vicinity (cf Figure 7-25). To reduce the calculation time, some small vias are replaced by larger vias. The EM-simulation results are exported to schematic and re-simulated with ideal resistors for the rat-race coupler, and capacitors are suggested on the datasheet of the driver [28]. The results are displayed in Figure 7-26. They show a 3 dB-passband from 34.5 GHz to 37.5 GHz with 8.4% bandwidth. The insertion loss is less than 3.2 dB. The gain unbalance remains less than 0.2 dB from 35 GHz to 36 GHz. The phase imbalance between the two out-of-phase ports is less than 3° throughout the band.

The insertion loss is consequent but expected as the filter has a 1.6 dB loss and the rat race 1.4 dB loss. The output power was divided by 2. This means that 0.2 dB is lost in the transitions. Note that the arms of the rat-race are significantly long due to the space needed for decoupling at the PA surrounding. The results, although partial, are therefore below the specs of the system simulations, as an insertion loss of maximum 1 dB was predicted for the rat-race. We expect a larger insertion loss at measurement because the arms of the rat-race to the PAs input are much longer.

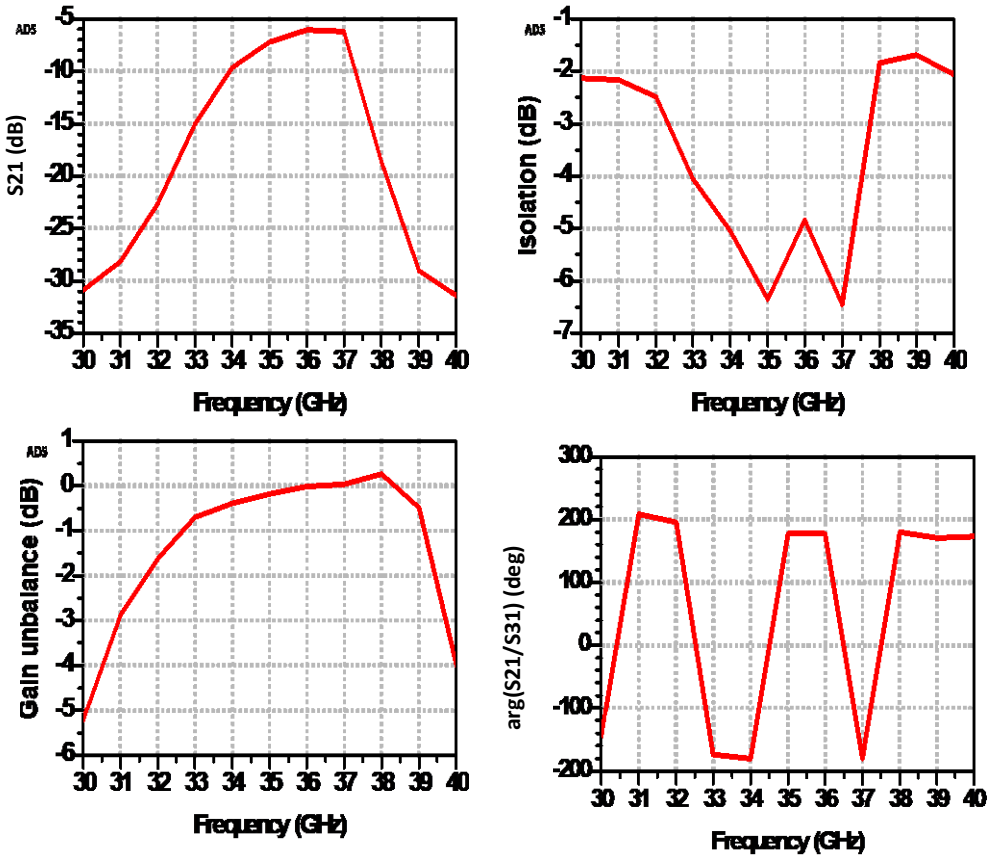

Figure 7-26: Simulation results of filter + rat race.
In the 35-36 GHz band, the insertion loss |S21|+3dB is 3.2. dB, isolation (S32) 5 dB, gain unbalance dB(S21/S31) is 0.2 dB and phase unbalance arg(S21/S31)-180° is <3°.

7.2.5 DC tunnelling

The push-pull amplifier required for second order harmonic distortion suppression needs two power amplifiers and two 180° hybrids. We use power amplifier from Analog Devices part number HMC7229LS6 in this purpose. The SMT component requires DC biasing on either of its sides and full ground under the chip. The option of tunneling the DC lines under the device is therefore not feasible. To avoid biasing in the middle of the board nevertheless, the DC lines are tunneled under the arms of the rat-race coupler at the PA input where the power levels are still relatively low (see Figure 7-27). To this extend, the bottom ground of the PCB is cut four vias away from the signal line on each side. The DC lines are extended under the RF lines with the same GCPW dimensions. The area is filled with vias to ensure that the common top and bottom layer ground area are correctly grounded. A single plated thru hole suffices to guide the DC signal between the top and bottom conductor layers. The DC tunnels are surrounded by shunt capacitors with high capacitance for decoupling.

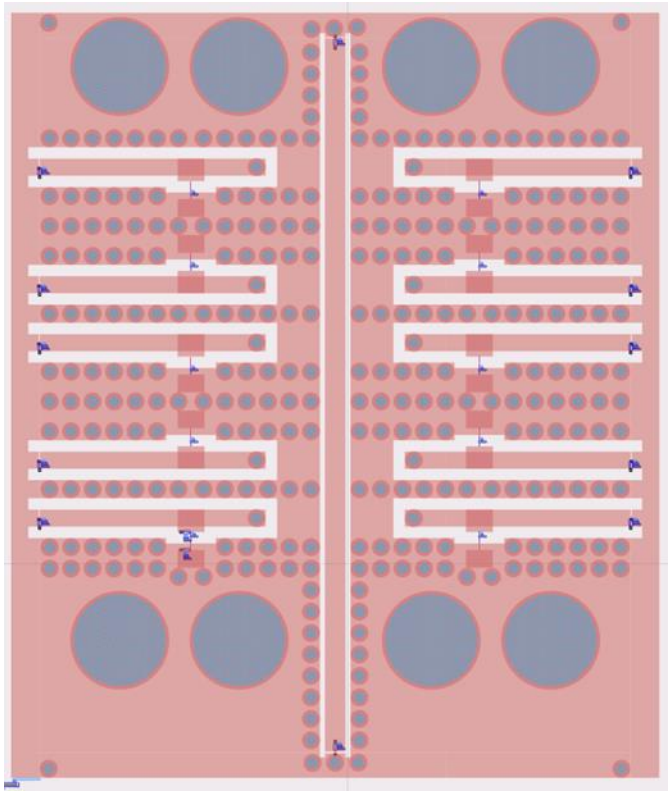

Figure 7-27: DC tunnels layout after export to schematic

On the capacitors footprints are placed clustered non-calibrated ports with reference to ground. All ports have a reference impedance of 50 Ohm. We EM-simulate the layout and export it into S-parameters schematic. We re-simulate it with ideal capacitors of capacitance 1 nF. The simulation results are gathered in Figure 7-28. The results show that there are few leakages between the DC and the RF signal lines. This demonstrates a satisfactory feasibility of the DC tunneling for the push-pull amplifier technique.

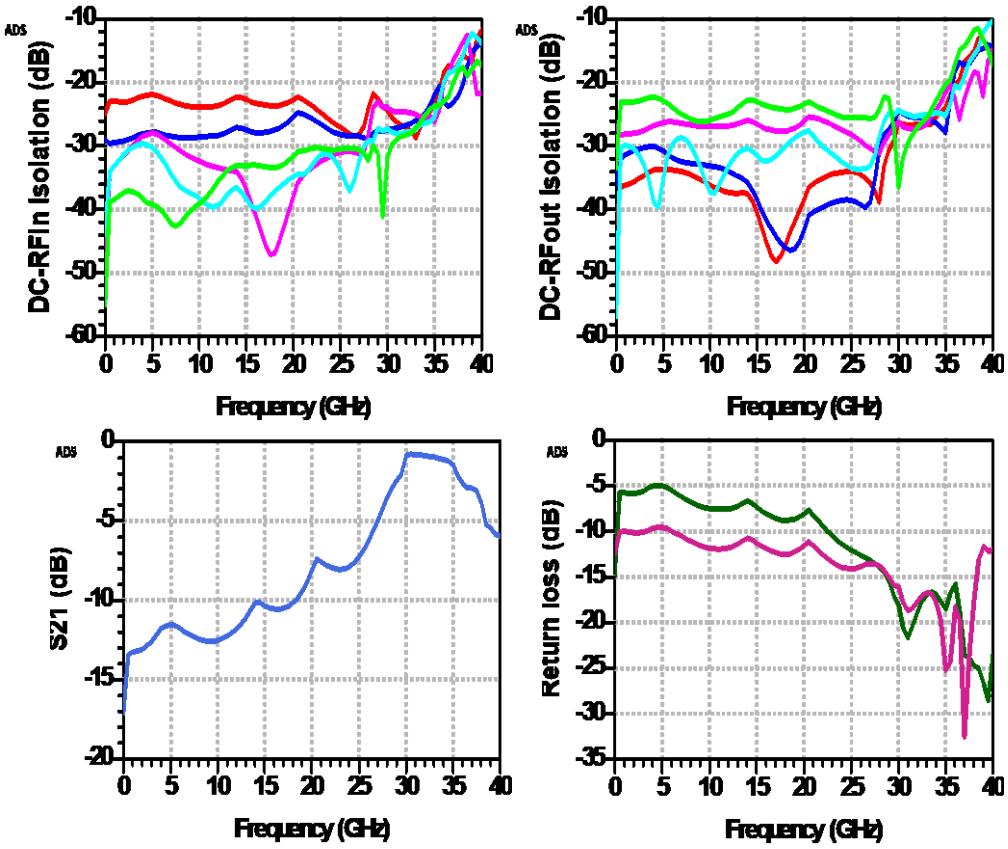

Figure 7-28: Simulation results of DC tunnels.
DC leakages from the different DC biasing lines is <20 dB to input and output RF line. The loss of the RF line is <2 dB in 35-36 GHz band. Both input and output are well matched to 35 GHz.

7.3 Measurement plan

The transmitter module and its four subsystems are fabricated and measured. First, we test the upconverter determine the performance of the lower sideband conversion as it is not specified by the manufacturer. We also optimize the LO suppression with the LO nulling technique which depends on the temperature, the LO power, but which also depends on the LO frequency, and consequently our substrate [21]. Second, we test the driver amplifier, a packaged commercial component from Centellax. Third, we verify the passband, the insertion loss and the return loss of the filter. Tests conducted on a single filter is sufficient, as the filter is guaranteed to be replicable. Finally, we characterize the performance of the push-pull amplifier. This test is also critical as the power amplifier will operate slightly under the specification of the datasheet. This was due to a lack of components in the desired band at the time of the development. We

will tune each PA to compensate an eventual amplitude unbalance, as part of the architecture enhancement.

7.4 Upconverter measurement

Figure 7-29 shows the up-converter module. It is composed of a DC-block C04BL121X-5UN-X0B from Knowles Capacitors to limit the mixing with DC leakages, a 3 dB-attenuator D10AA3Z4 from Anaren to level down the IF power to recommended -10 dBm IF input power and decrease eventual reflections, and low-pass filter LFCN-1575 from Mini-Circuits. Follows the Hartley architecture consisting in the 90° hybrid IPP-7116, the baluns NCS1-112+ and the up-converter TGC4645-SM for single sideband conversion. The decoupling capacitors are chosen from different manufacturers and are placed as suggested in [21]. R2 is a 50-Ohm resistor, R3 is a 0-Ohm resistor and R1, R4 are unmounted for lower-sideband conversion.

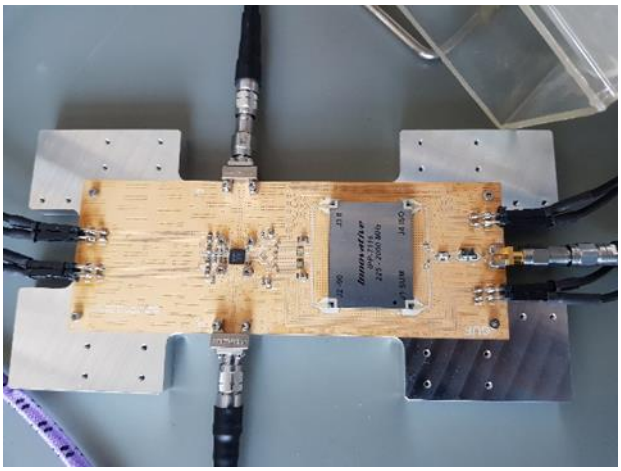

Figure 7-29: Up-converter module for lower sideband conversion.

7.4.1 Measurement setups

We would like to read the output harmonics to verify the upper sideband suppression and perform the LO nulling. We also need to determine the conversion gain and the passband.

7.4.1.1 Output spectrum measurement setup

We use the 67 GHz 4-port PNA-X network analyzer N5247B from Keysight Technologies as IF and LO signal sources, and the FSW signal and spectrum analyzer from Rhode & Schwarz to measure the spectrum. The PNA-X does have a Spectrum Analyzer option, but it is not supported for converter measurement at the time of development. Figure 7-30 shows the measurement setup. IF input is delivered by port 2 of the PNA-X, the LO signal by port 3. To calibrate the output

power, we connect the PNA-X to the FSW directly and measure the loss at RF frequencies. The loss is then retrieved from the measurement data.

Figure 7-30: Up-converter measurement setup for output spectrum measurements.

7.4.1.2 S-parameters measurement setup

The setup for S-parameters measurements is very similar to the setup of Figure 7-30 except that the DUT output is connected back to the PNA-X to port 1. We set the "Converter/Mixer" measurement class. We specify the LO quadrupler in the mixer settings. We use the Frequency sweep. We follow the Smart Cal guide to calibrate the PNA-X. The 2.4 mm ports are calibrated with Keysight electronic calibration module model N4693-60001 and the SMA connectors are calibrated with Maury calibration kit model 8770C for 2.92 mm connectors, 2.92 mm and SMA being compatible. Therefore, the results are reliable up to 50 GHz for the RF, and up to 18 GHz for the IF.

7.4.1.3 DC biasing procedure

Eight sources are needed for the DC biasing. First the bias voltages VGX, VGMU, VGLO, VDLO, VGRF and VDRF are applied using the bias-up procedure suggested in [21]. We wait to power up the converter and read the output spectrum to apply VI and VQ for LO nulling.

7.4.2 Measurement results

7.4.2.1 Output spectrum and LO nulling

Figure 7-31 shows the output spectrum when the input signal is 1 GHz at -10 dBm. We see that the spectrum is pretty clear and that the correct sideband (the upper one) is suppressed by at least 10 dBc. The conversion gain is 4.4 dB. However, we see that the LO leakages are pretty high, around -3 dBc. Figure 7-32 compares the output spectrum with and without LO nulling applied. We managed to decrease the LO level up to -33 dBc.

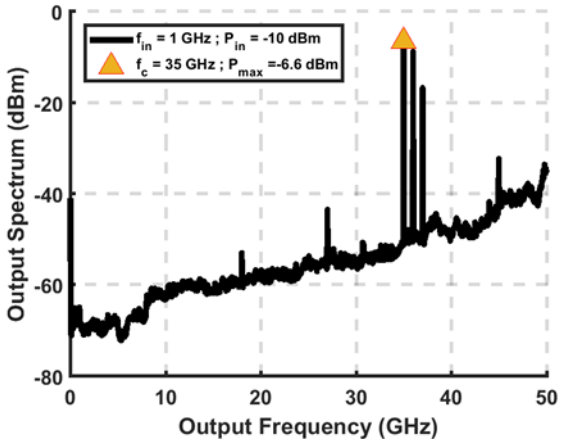

Figure 7-31: Output spectrum of the up-converter without LO nulling applied.

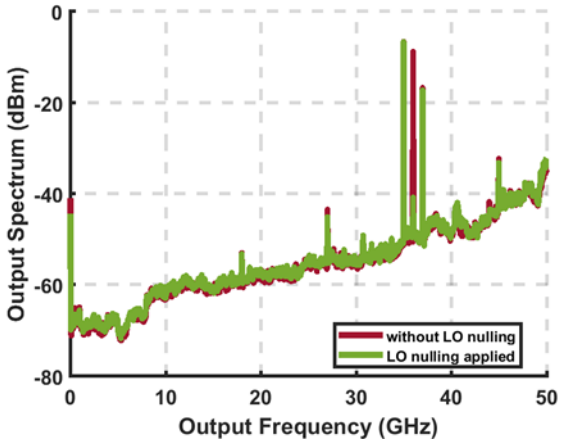

Figure 7-32: Output spectrum of up-converter when LO = 8 dBm @9 GHz: with LO nulling vs. without LO nulling.

The voltage couples [VI,VQ] = [-0.146V,-0.125V] was applied to the IF input with trials and errors to minimize the LO. The 4LO suppression is > 30 dBc

7.4.2.2 Conversion gain and image rejection

Figure 7-33 shows the conversion gain for the lower sideband and the upper sideband. They correspond to the SC12 parameters. The gain of the up-converter is around 7 dB. The passband is 34.5 to 35.5 GHz. Figure 7-34 depicts the image rejection which is the difference between the lower sideband and upper sideband conversion gain. The rejection is above 10 dBc within the passband and above 15 dBc within the 35-36 GHz band.

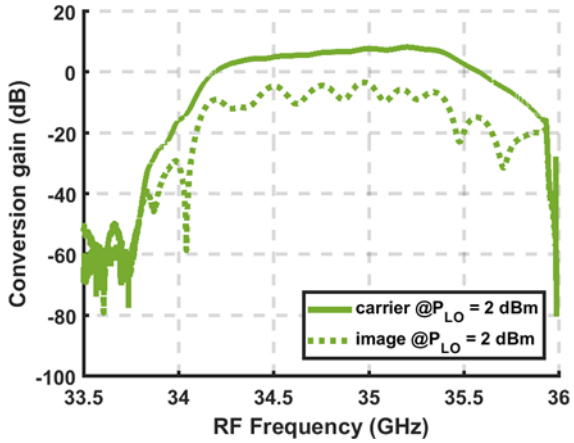

Figure 7-33: Conversion of up-converter when IF = [10MHz-3.5 GHz] @-10 dBm and LO = 2 dBm @9 GHz for LSB (carrier) and USB (image) conversion.

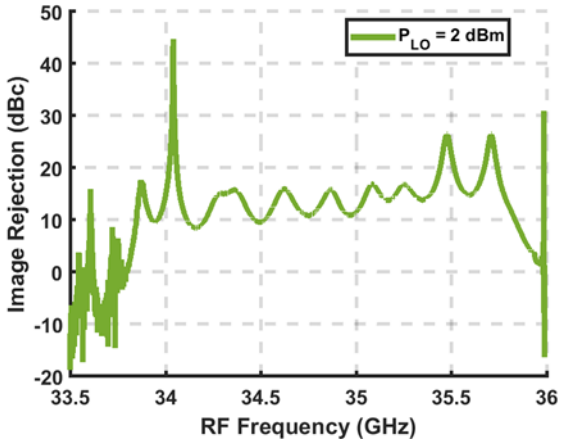

Figure 7-34: Image rejection of up-converter when IF = [10MHz-3.5 GHz] @-10 dBm and LO = 2 dBm @9 GHz.

The results of the characterization show that the chip is suited for lower sideband conversion and operates relatively well outside its specs. The results are satisfactory for our radar transmitter application.

7.4.3 Measurement improvement

Note that the image suppression simulations in the system study was optimistic as there was no proper way to anticipate the performance of the mixer outside its specs.

There is a difference of 3 dB between the conversion gain deducted from the S-parameter and the output spectrum measurement. This is because no source power was performed for the output spectrum measurement, therefore the input cable loss was not compensated.

The measurements can further be improved by decreasing the number of adapters and mounting female 2.4 mm-connector and male K connector on the board. The cable should have respectively male 2.4 mm and female K. The thru-open-short-load standard measurement could be measured with the mechanical calkits, there would be no need for adapter for power calibration with the power sensor and no adapter for thru line. In our case, we used the adaptor de-embedding option proposed by the PNA-X.

7.5 Driver measurement

The driver TA0L50VA from Centellax is used to drive the push-pull amplifier into saturation. We check that the gain is sufficient at 35 GHz.

7.5.1 Measurement setup

Figure 7-35 shows the output spectrum measurements using the Spectrum Analyzer measurement class for 2-port DUT of the PNA-X. The input port is calibrated with the E-cal. The output loss is measured by a thru line, including the attenuator and the bias tee. The loss is then compensated during post-processing.

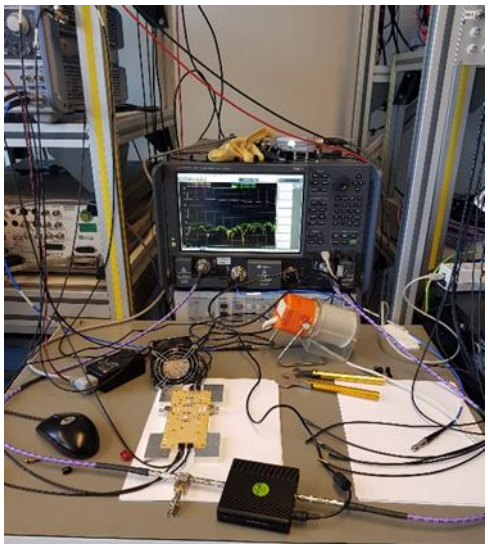

Figure 7-35: Measurement setup of the driver for spectrum measurement.
There is a 20 dB attenuator and a bias tee at the output (port 1) to protect the PNA-X from high power leakages.

7.5.2 Output spectrum and gain

Figure 7-36 shows the output spectrum of the driver. The gain at 35 GHz is 30 dB which is within the specs of the manufacturer [50]. The driver is suitable for our transmitter measurements.

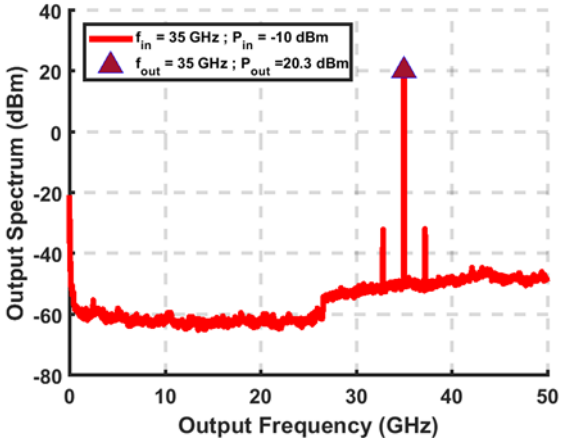

Figure 7-36: Output spectrum of driver.

7.6 Filter measurement

We characterize the filter specially designed for the 35 GHz radar.

7.6.1 Measurement setup

Figure 7-37 shows the filter and the measurement setup. It uses the PNA-X in the classic two port S-parameters measurements. The calibration is done with the electronic calibration module N4693-60001 for 2.4 mm connectors.

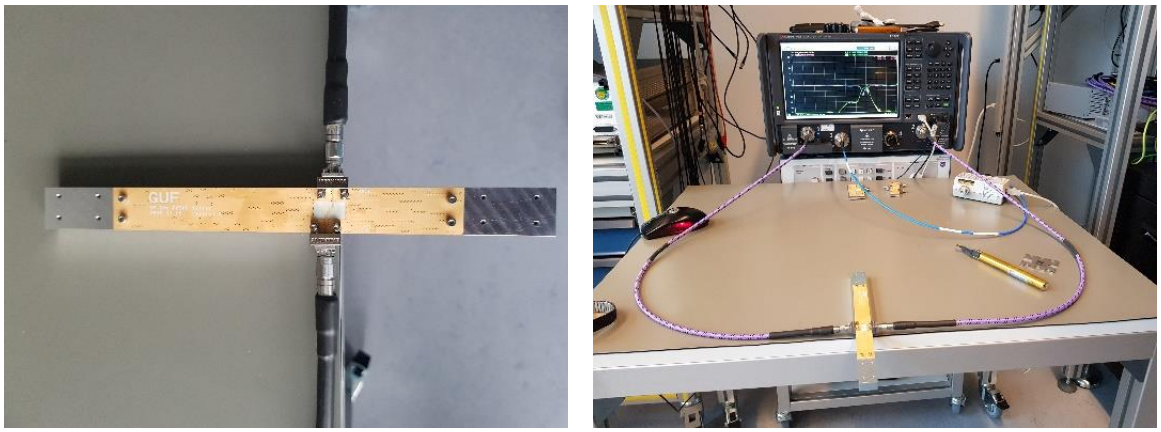

Figure 7-37: Filter measurement setup.

7.6.2 S-parameters measurements

Figure 7-38 displays the measured S-parameters of the filter. The insertion loss is 5 dB. Input and output return loss are 9 dB. The fractional bandwidth is 8%. The measurements are in accordance with the EM-simulations. The transitions from microstrip to GCPW and the connectors easily account for the additional loss.

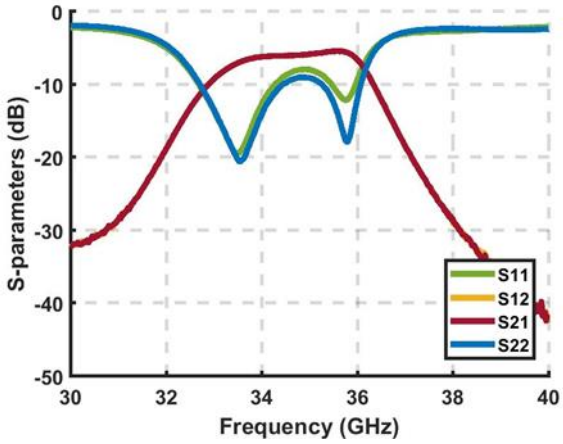

Figure 7-38: Measured S-parameters of the filter.
Insertion loss is 5 dB. Input and output return loss is 9 dB. Center frequency is 35.5 GHz and 3 dB-passband is 33-36.25 GHz.

7.7 Push-pull amplifier measurement

We want to characterize the push-pull amplifier architecture. We recall that the architecture can also double the output power, compared to using a single amplifier, only if the 180° couplers have a low insertion loss. Figure 7-39 exhibits the push-pull amplifier board. It includes two power amplifiers HMC7229LS6 from Analog Devices and two microstrip rat-race couplers. The 1-cm aluminum heatsink was cut around the DC tunnels to avoid grounding the signal lines. The performance of the microstrip 180° couplers directly impact the performance of the push-pull through gain and phase unbalance, therefore we start by characterizing the rat-race.

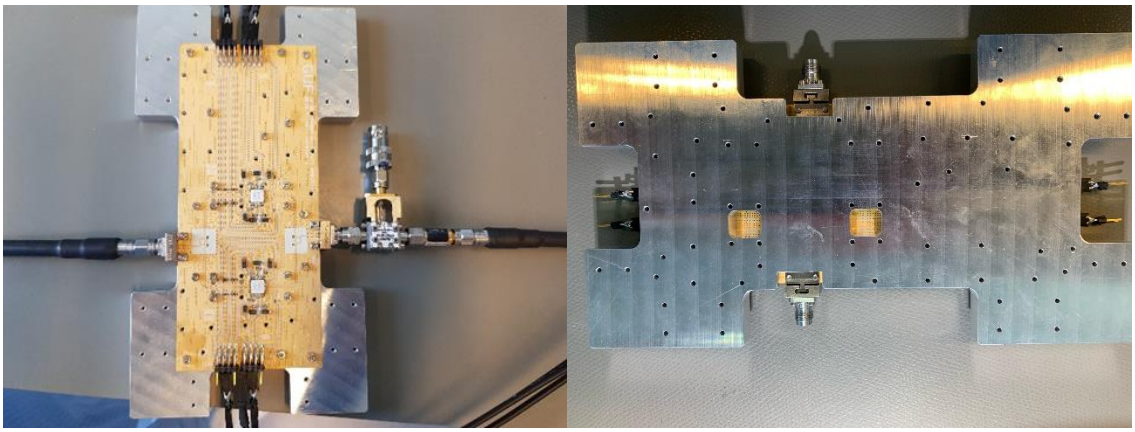

Figure 7-39: Push-pull amplifier upside (left) and backside (right).

7.7.1 Rat-race measurements

The rat-race coupler presented in Section 7.2.4 is fabricated and measured, using the 4-port PNA-X N5247B from Keysight, calibrated with the electronic calibration module N4693-60001. The measured rat-race corresponds to the one at the input of the push-pull, with its arms going till the DC tunnels. The measurement setup can be seen on Figure 7-40.

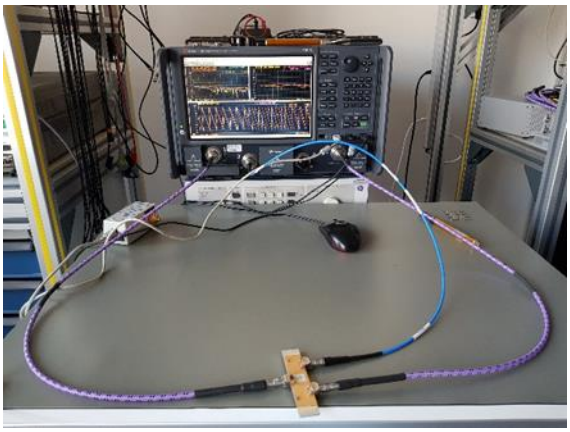

Figure 7-40: Rat-race coupler measurement setup.
The 2.4 mm connectors 1492-04A-4 from Southwest Microwawe are mounted on the board. The rat-race coupler input is connected to port 1 of the PNA-X, the -90° and the -270° outputs to port 2 and 3 respectively.

From the measurement results presented in Figure 7-41, we see that the insertion loss of the rat-race is 4 dB. The input return loss is less than 12 dB and the output return loss less than 8 dB. The isolation is around 20 dB in-band. The phase difference between both output ports is 180° with an unbalance up to 12° within the 35-36 GHz range. The gain unbalance is less than 0.2 dB

in-band. We can see from the reflection parameters that the rat-race output is slightly overdesigned to 36 GHz instead of 35.5 GHz. The input is well matched.

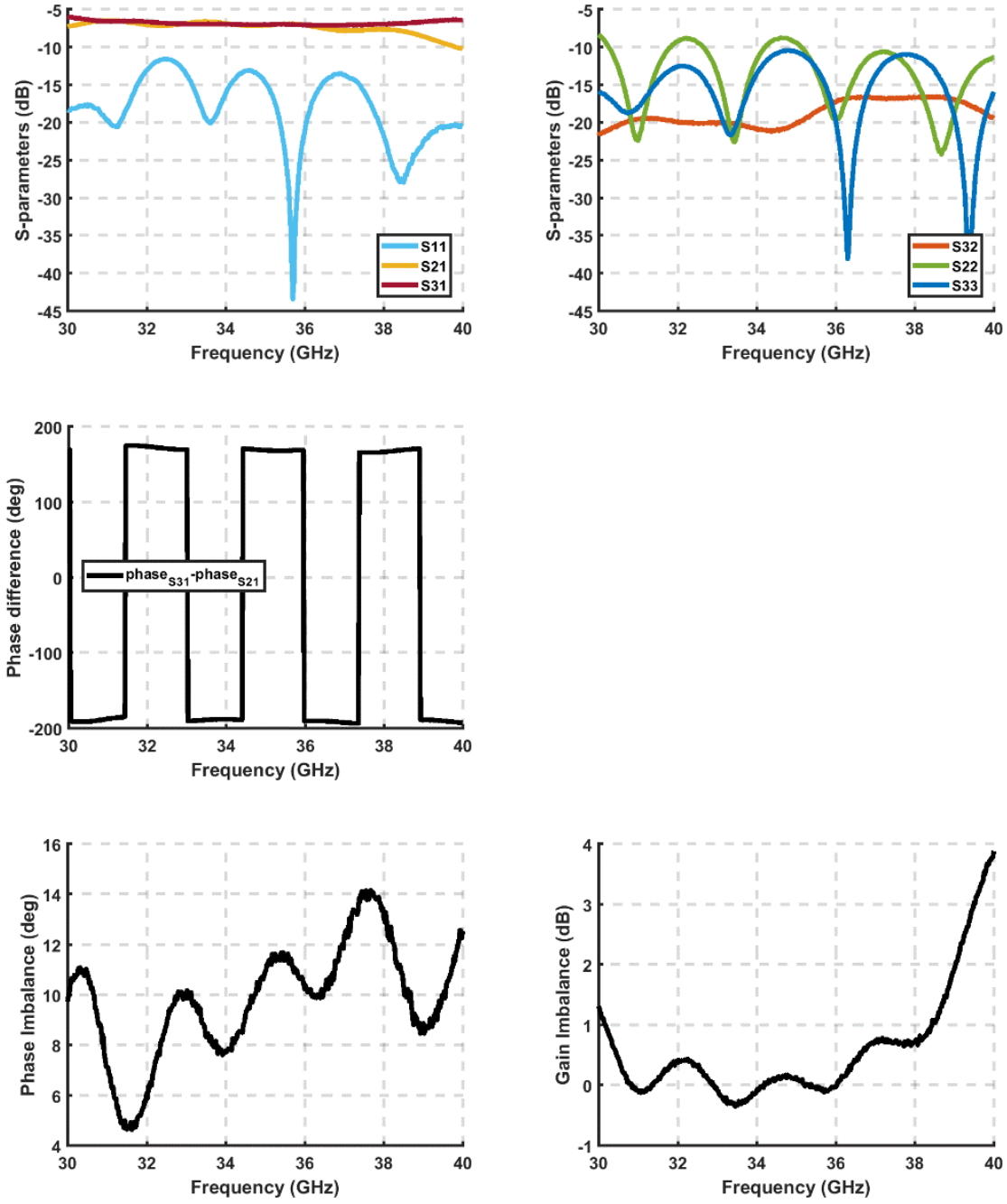

Figure 7-41: Rat-race coupler measurement results.

Results of gain unbalance and isolation matched the EM-simulations. The phase unbalance is much less than in EM-simulations but the measured results are still within the worst-case scenario which we had simulated in the system study. However, the 180° hybrid is much more lossy than expected, by 3 dB. This is because the rat-race arms are longer than expected due to the tunneling and the space that it takes on board. The output rat-race was not measured but it is assumed to be even more lossy, as its arms are longer than the input rat-race due to biasing network. This means that the output power of the push-pull amplifier will be at least 3 dB lower than expected in the system study.

7.7.2 DC tunnels measurements

We want to determine the actual impact of the DC tunnels on the performance of the push-pull amplifier system. We fabricate the subsystem including the input rate-race and the DC tunnels (cf. Figure 7-42). We measure right after the filter output and the power amplifiers input, with PNA-X N5247B from Keysight under the same calibration. The results of the measurements are shown in Figure 7-43.

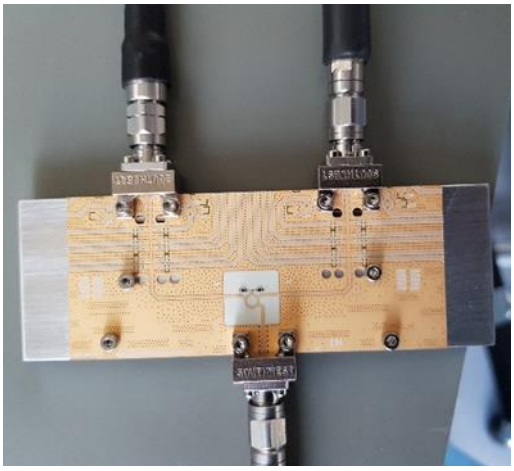

Figure 7-42: DC-tunnels including rat-race.
They represent the input of the push-pull architecture, from the filter output till the power amplifiers inputs.

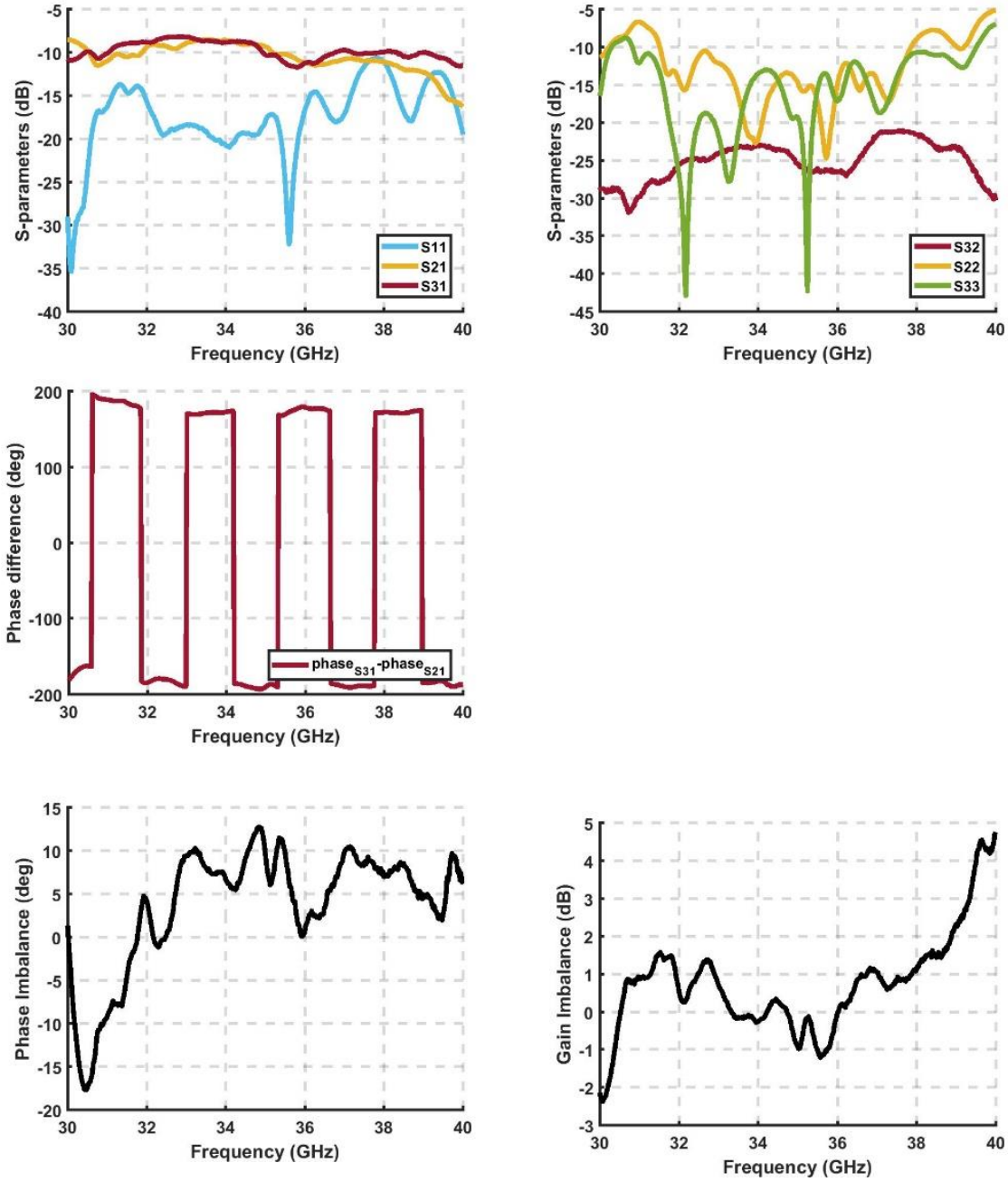

Figure 7-43: DC-tunnels measurement results.

The insertion loss drops to 7 dB, meaning that the lines due to DC tunneling bring an additional 3 dB loss at the push-pull input. The input return loss is less than 14 dB. The output return loss is less than 13 dB. The input and output of the system is well matched to 35.5 GHz. The isolation is

23 dB. The increase corresponds to the additional loss from the lines. The phase difference between the ports is 180° with an unbalance up to 12°. The gain unbalance is now 1 dB.

This shows that the unbalance performance of the rat-race is slightly degraded by the DC tunnels. The insertion loss is also very large. This is due to the extension of the lines because of the DC tunnels. This was not anticipated in the system study and will impact the gain performance of the rat-race, as more power will be needed to drive the power amplifier into saturation.

7.7.3 Push-pull amplifier measurements

We measure the push-pull amplifier with PNA-X N5247B from Keysight alone and then driven with the amplifier TA0L50VA from Centellax. We choose the Spectrum Analyzer measurement class. Both measurement setups can be seen in Figure 7-44. In both cases, we place the bias tee BTN20050 from Marki followed by the 20 dB-attenuator 8490D from Keysight at output to protect from eventual high power output. We calibrate by measuring the bias tee and the attenuator alone, then withdrawing the attenuation from the measured spectrum of the whole setup.

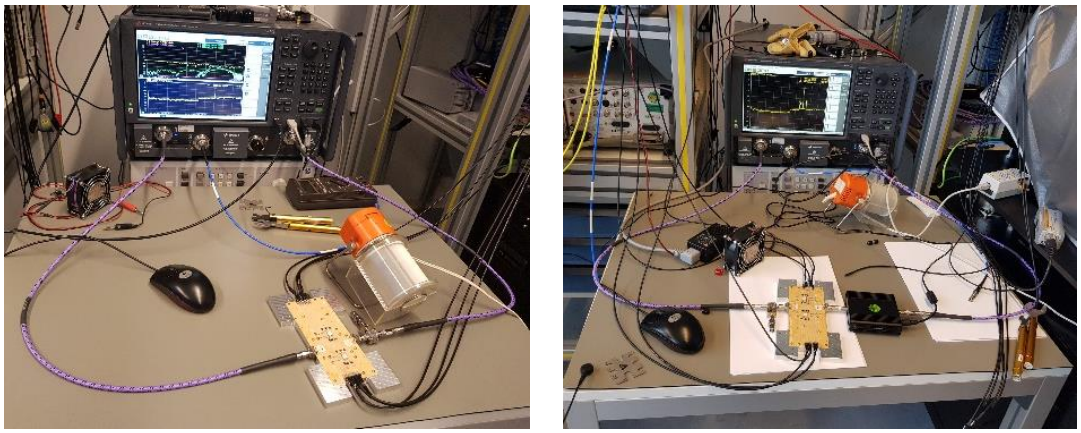

Figure 7-44: Push-pull architecture measurement setup when measured alone (left) of with a driver amplifier (right).
Input port of the DUT is connected to Port 2 of the PNA-X and output port to Port 1.

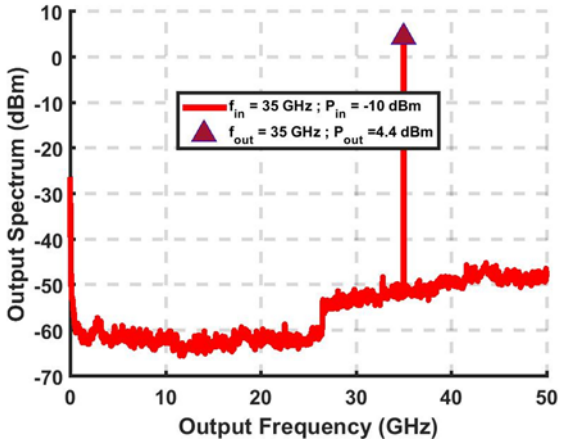

Figure 7-45: Output spectrum of the push-pull alone, without driver.

Figure 7-45 shows the output spectrum of the push-pull measured alone. We see that for an input of -10 dBm, the output is 4.4 dB corresponding to a gain of 14.4 dB. This is poor but expected, because of the 7 and 4 dB-loss at the input and output respectively. We see that the spectrum measured up to 50 GHz is clear. Figure 7-46 shows the output spectrum of the push-pull when driven by a pre-amplifier when the input power is -30, -20, -10 and 0 dBm. We see that the spectrum stays quite clear. The two harmonics around 32 and 37 GHz are triggered by the driver (cf. Figure 7-36) and amplified by the push-pull. The SFDR remains above 50 dBc in-band. When the push-pull is driven into saturation, the output power is 31.3 dBm. Which is 3 dB below what was expected in the system study (cf. Section 4.2) but anticipated in the balun characterization. Figure 7-47 plots the output power and the gain of the push-pull and the driver with respect to the input power. We see that the push-pull starts saturating when the power at the input of the driver is around -15 dBm, when the gain starts going down slowly. This corresponds to a power around 15 dBm at the input of the push-pull (cf. Section 7.5) and a power around 7 dBm at each amplifier input (cf. Section 7.7.2). This is expected as the saturation of the power amplifier occurs around 6 dBm input [25]. The input 1 dB compression point IP1dB is around -9.5 dBm. The output 1 dB compression point, OP1dB is then 31 dBm.

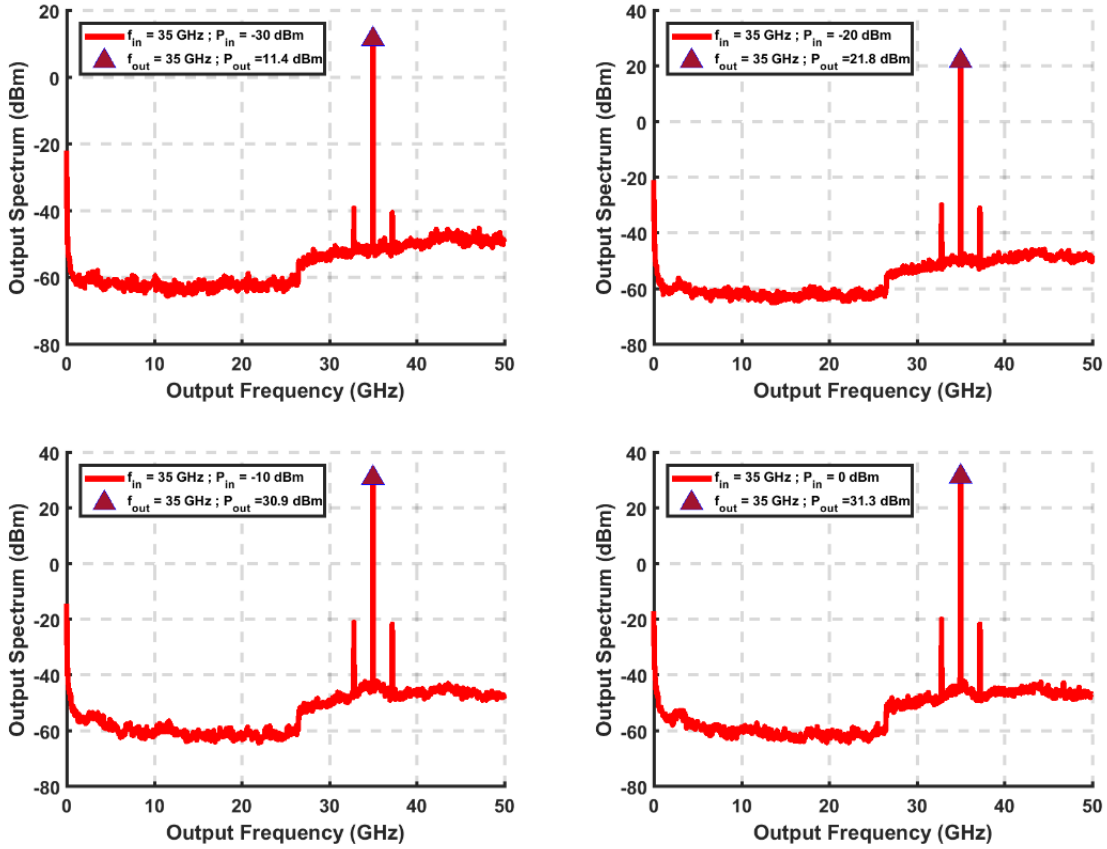

Figure 7-46: Evolution of push-pull output spectrum vs. input power.
The push-pull input is driven by amplifier TA0L50VA from Centellax.

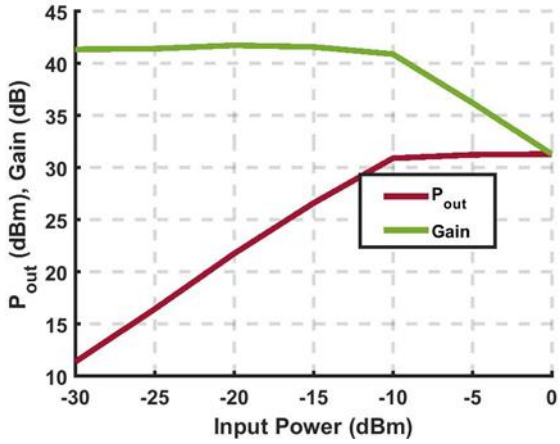

Figure 7-47: Output power and gain vs. input power at 35 GHz.
The measurement includes the push-pull amplifier and the driver. The small signal gain is 40.5 dB. The gain starts decreasing at -15 dBm input and drastically drops around -10 dBm.

Finally, Figure 7-48 compares the output spectrum in different scenarios, when we turn one or both power amplifier on. The push-pull is measured alone and not driven. We see that the output power of the push-pull architecture is indeed larger than the output power of a single power amplifier. This validates the principle of the push-pull operation.

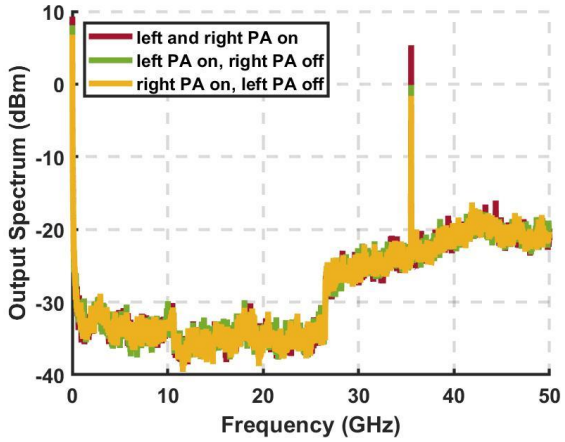

Figure 7-48: Comparison of output spectrum in different scenarios of the activation of the PA. *Strong DC leakages were present at the time of the measurements, the reason is unknown.*

The output power of the push-pull is 31 dBm when correctly driven to saturation. The output power is 3-4 dB less than simulated because of the loss due to large biasing network.

7.7.4 Performance improvement and second order distortion characterization

The push-pull architecture would have better performance if the chosen PA could be biased on one side. Both space between the PAs, and space for DC tunnels would be reduced tremendously. The length of the arms of the rat-race would be reduced and the rat-race would be less lossy. This would save power as the push pull could be driven into saturation at lower input power, and the output power would also be greater. This design limitation will not be a problem for W-band application where the amplifiers are self-designed.

We could not properly characterize the suppression of the second order distortion. A possibility would have been to characterize both PA alone and push-pull in the saturation regime, and compare their output distortion. Measurements could have been conducted above 50 GHz with a measurement mixer to see eventual harmonics.

7.8 Transmitter measurement

We measure the performance of the whole transmitter by assembling the different subsystems, that is up-converter, driver amplifier, filter and push-pull amplifier.

7.8.1 Measurement setup

All subsystems have female 2.4 mm connectors; we therefore connect them with male-male 2.4 mm adapters. We place at the output of the DUT a bias tee followed by an external attenuator. The IF and LO signals are generated by the PNA-X. As for the up-converter, we connect the DUT input to port 2, LO to port 3 and output to the FSW for spectrum measurements, and back to port 1 of the PNA-X for S-parameters measurements. The different measurement setups can be seen in Figure 7-49. For spectrum measurements, we apply the same calibration method as for the upconverter (see Section 7.4). For S-parameters measurements, we measure the transmitter chain using an external 10 dB-attenuator 8490D from Keysight and we include both attenuator and bias-tee in the calibration. To have a good calibration, we set port 1 at -10 dBm and port 2 at -20 dBm during the calibration: this way the power is roughly the same at the through reference. Measuring the S-parameters with a 10 dB-attenuator is preferable in our setup, because it facilitates the calibration as the attenuator can directly be included. The transmitter output power can be maximum 32 dBm according to previous measurements so we are sure not to damage the PNA-X.

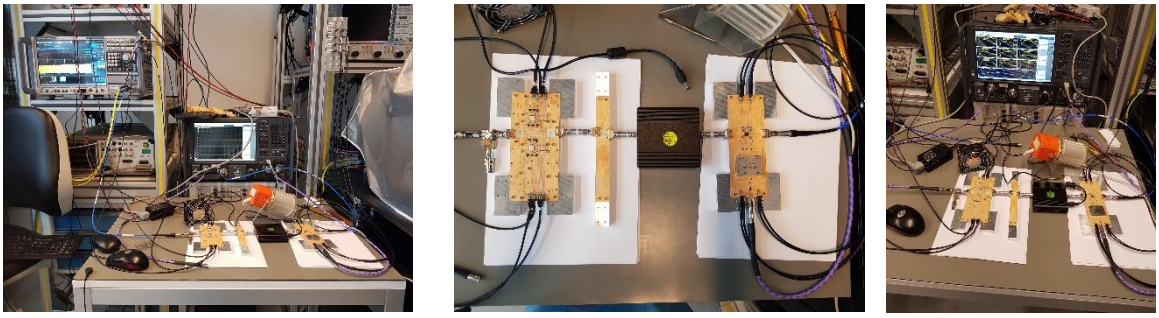

Figure 7-49: Measurement setup of the transmitter chain.
We use a 20 dB-attenuator for output spectrum measurements and a 10 dB-attenuator for S-parameters measurements.

7.8.2 Measurement results

7.8.2.1 Saturation and Compression

Figure 7-50 displays the output power and the gain of the transmitter chain in comparison to the input power measured at 35 GHz. The input power ranges from -20 dBm to 0 dBm. The small signal gain is 38.5 dB. We see that the transmitter starts overloading around -18 dBm input, when the gain starts dropping. This is expected; the gains of the upconverter, the filter, the driver and the input rat-race being 7 dB, -5 dB, 30 dB and -7 dB respectively, this means that the power at the input of each power amplifier is around 7 dBm which is saturation [25]. The input 1dB compression point, P1dB is around -15 dBm. The output P1dB is therefore 22.5 dBm. The

transmitter completely saturates at -4 dBm where the saturation power Psat is 24.4 dBm. The measurement results are 7 dB less than expected from the push-pull amplifier measurements. We assume that this is due to a sudden defect on board towards the output. Despite the discrepancy in power, the behaviour of the compression of the transmitter chain is in accordance with the characterization of the push-pull amplifier.

Figure 7-51 compares the carrier conversion gain and the image conversion gain when the input power is -4 dBm. The passband is flat in the range 34.3-35.8 GHz. The conversion gain is around 31 dB, and saturation therefore around 27 dBm, which is 3 dB more than in Figure 7-50. We recall that the 3 dB discrepancy between both measurement methods is due to the absence of source power calibration for the output spectrum measurement (cf. conclusions of Section 7.4) The results of both measurement methods are therefore consistent.

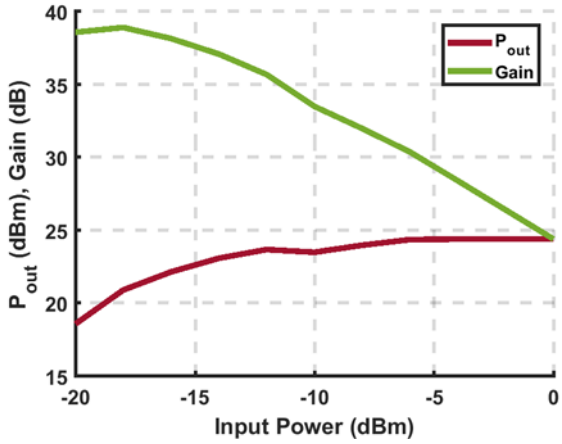

Figure 7-50: Output power and gain vs. input power of transmitter chain at 35 GHz.
The output spectrum was measured with a spectrum analyser and the power and the gain deducted. LO nulling was applied.

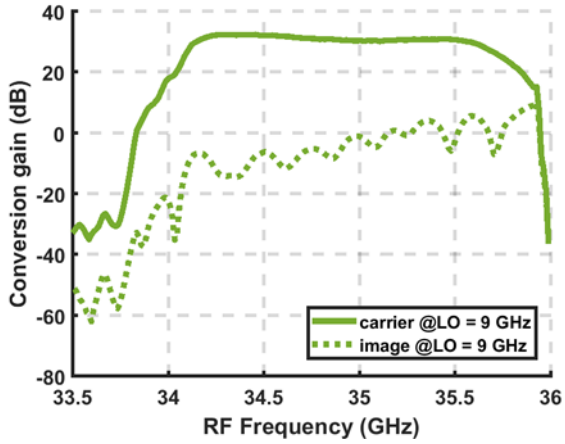

Figure 7-51: Conversion gain of the carrier and output frequency for a 9 GHz input LO when IF = -4 dBm (saturation).

The S-parameters were measured with network analyser. Note that since the push-pull architecture operates voluntarily in saturation, the critical parameter is the output power, and not the transmitter gain as conventionally.

7.8.2.2 Output spectrum in saturation

Figure 7-52 shows the output spectrum of the transmitter chain in saturation, for a 1 GHz input at -4 dBm and a 9 GHz LO. The LO nulling couple [-0.147V,-0.125V] is applied. The in-band SFDR is more than 20 dBc.

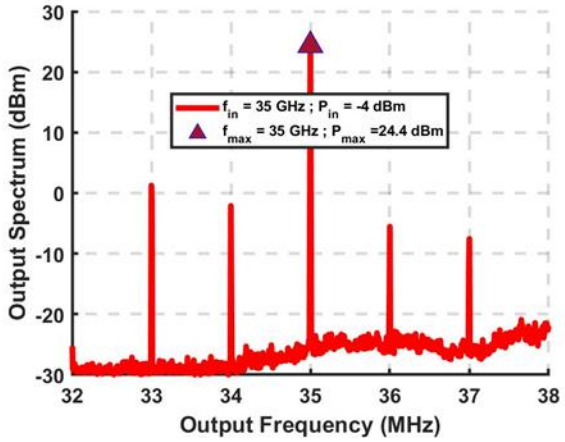

Figure 7-52: Output spectrum of the transmitter chain in saturation.

The measured spectrum is very close to the simulated spectrum Figure 4-5 a): the level of the spurious signal is similar but that the carrier signal level is 10 dB lower.

7.8.2.3 Image rejection

The image rejection performance is improved by the transmitter chain (see Figure 7-52 to Figure 7-53). It is above 25 dBc in-band, while it was 10 dBc for the up-converter alone. This is because the image is further rejected by 15 dB by the bandpass filter (cf. Figure 7-21).

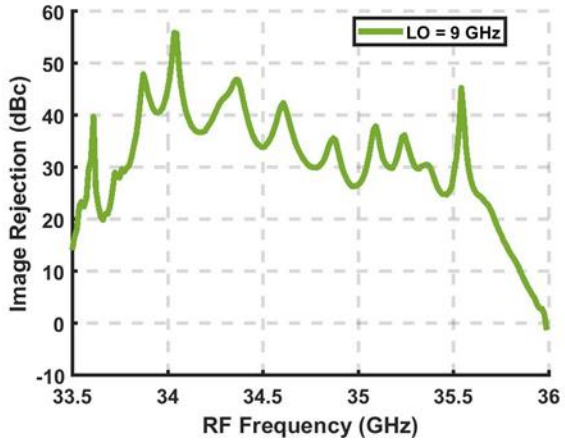

Figure 7-53: Image rejection when LO nulling is applied.

7.8.2.4 Input return loss

Figure 7-54 shows the input return loss of the transmitter. It is around 15 dB over the whole band which is very satisfactory for our radar application.

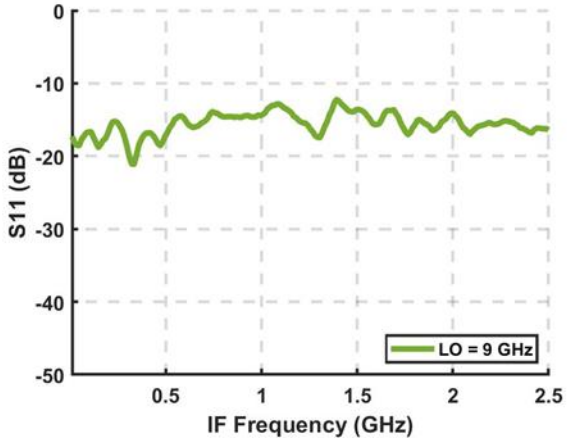

Figure 7-54: Input Return Loss of Tx

7.8.2.5 Output return loss

Figure 7-55 shows the output return loss of the transmitter. It is above 15 dB in the band 34.3-35.8 GHz and the transmitter output is matched around 34.6 GHz and 35.5 GHz. These results are very satisfactory for our radar development.

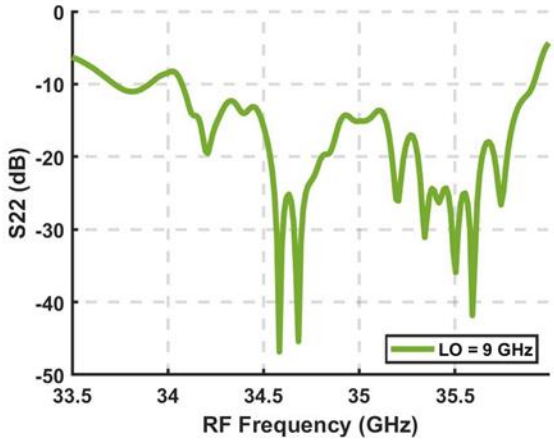

Figure 7-55: Output Return Loss of Tx

7.9 Summary and remarks

We developed and measured a modular Ka-band transmitter for millimetre-wave FMCW radar, based on the proposed advanced architecture. The transmitter is a prototype for future highly-integrated radar frontends. It is composed of commercial surface mount devices and in-house designed microstrip components which could be all integrated at W-band frequencies. We expect the novel architecture to guarantee a high output power and low spurious free dynamic range. The measurement results of the subsystems are satisfactory. The conversion gain of the up-converter is 7 dB, the upper-sideband image suppression is 10 dBc, the LO suppression is above 30 dBc. The bandpass filter has a 5 dB-insertion loss, 9 dB- input and output return loss, and its fractional bandwidth is 8%. The output power of the push-pull during saturation is 31.3 dBm and the output 1 dB compression point is 31 dBm, which is lower than expected in the system study. This is explained by the large size of the 180° hybrid on board and thereby large insertion loss. The measurements of the full transmitter show that the bandwidth is 34.3-35.8 GHz. The output power is up to 24 dBm. The image suppression and the LO suppression are above 25 dBc. The measurements of the full transmitter chain yet promising in regards with the sub-systems characterization, did not match the subsystem measurements due to a sudden defect on the board. Table 7-1 shows a summary of the transmitter performance, with output power from subsystem measurements.

The passband of the transmitter is significantly large and flat in the range desired frequency range 35-36 GHz. The spurious signals are well rejected. This validates the proposed system and makes it a suitable candidate for FMCW and CDM-based intra-pulse modulation for high-resolution imaging applications. The system validation can be improved by designing the push-pull architecture using amplifiers with single-sided biasing network. This would decrease the size of the push-pull amplifier and improve the gain and the output power. The out-of-band SFDR can be investigated by measuring the output spectrum using a spectrum analyser combined with a measurement mixer to see the second-order harmonics.

Table 7-1: Summary of Tx measured performance

Parameters	**Min.**	**Typ.**	**Max.**	**Units**
IF Frequency Range	0.2		1.7	GHz
LO Frequency Range		9		GHz
RF Frequency Range	34.3		35.8	GHz
Psat		24*		dBm
OP1dB		22.5*		dBm
Conversion Gain		37		dB
Input RL		15		dB
Output RL		15	25	dB
Image Rejection		25		dBc
LO Rejection		30		dBc
SFDR (in-band)		>20		dBc
Supply Power		28		W
LO Drive		8		dBm

Measurement results when Pin = -4 dBm. LO nulling couple [-0.147V,-0.125V] applied.

**Psat and OP1dB were impacted because of the sudden defect on the push-pull amplifier module and are expected to be around 31.3 dBm and 31 dBm respectively.*

Chapter 8

Receiver circuit design and measurements

This Chapter presents the measurement results of a variable high-gain receiver module for FMCW radar applications based on our proposed architecture for system validation. The receiver includes the front-end only; this means that stages after the deramp mixer, including the demodulation, are not considered as highlighted in Figure 8-1. It operates at 35 GHz and serves as prototype for future radar receiver designs, up-scaled in frequency to the W-band (75-110 GHz) and higher bands. Therefore, the work carried out in this Chapter aims to anticipate the different challenges which could be faced at W-band frequencies and to propose a realistic and optimal solution, tested and validated in the Ka-band.

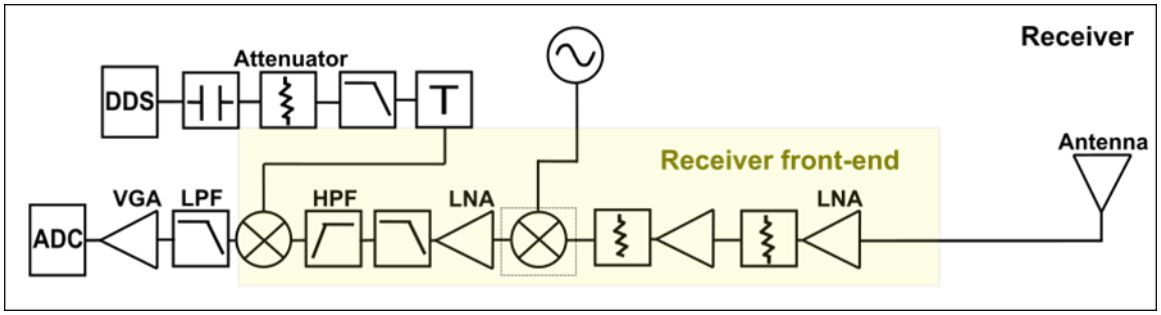

Figure 8-1: Proposed receiver.
All the components of the implemented front-end (highlighted) are commercial SMD.

8.1 Design rules and fabrication

The Rx module is designed on a 0.254 mm (10 mil)-thick Rogers RO4350B substrate. The substrate dielectric constant is 3.48 and the loss tangent is 0.0037, both measured at 10 GHz [45]. The thickness of the copper conductor layers is 35 µm (1 oz). Both top and bottom copper layers are covered with 0.6-0.8 µm-thick Electroless-Palladium-Immersion-Gold (EPIG) finish. The PCB is milled to the edge, and copper burrs are removed to ensure the electrical contact of the RF connectors. The diameters of the plated through holes (vias) are 254 µm with a 75 µm-thick

annual ring. The plated drills are 2058 µm. The Rx module is exclusively composed of commercial components in surface mount technologies (SMT), mounted on a grounded coplanar waveguide (GCPW) layout. As for the transmitter, we wish to avoid potential frequency distortion due to solder mask, while still guaranteeing the repeatability of the measurements results. Therefore we surround the SMT component landing footprints by a thin band of solder mask of 200 microns (cf. Figure 7-2). The manufacturing and the mounting of the receiver prototype are outsourced under the same design tolerance as for the transmitter.

The footprints of the SMT components are designed on grounded coplanar waveguide following the recommendations of the manufacturers [22]-[24],[30]-[37] and optimized to save space on the board. We focus more particularly on three tasks. First, we optimize the RF transitions to limit losses and reflections. Second, we process as for the transmitter and symmetrize the Hartley architecture used in the down-conversion in order to allow for either upper-sideband or lower-sideband suppression. Thereby we have more flexibility in the choice of the operating band and of the LO frequency. Finally, we design the receiver module so that one, two, all or none amplification stages can be selected.

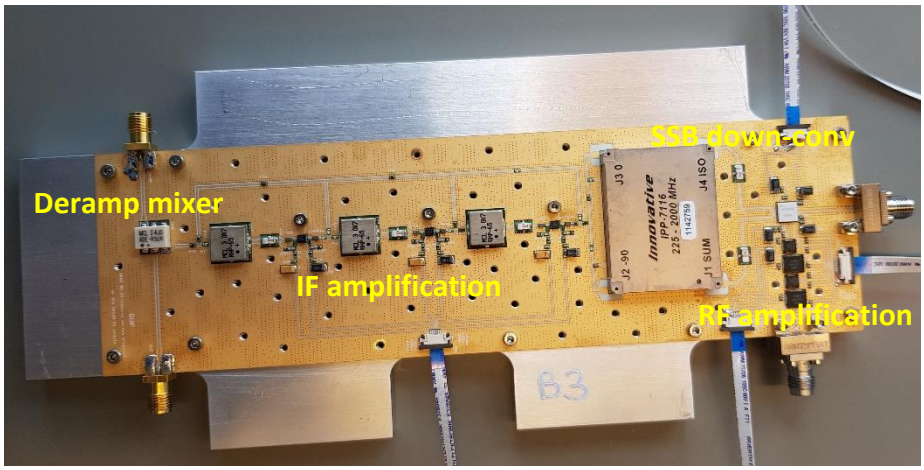

Figure 8-2: Proposed receiver module B3, featuring a single IF amplification stage.
The module is fixed to a 1 cm-thick aluminium heatsink. The boards are mounted on a 1 cm-thick aluminium heatsink.

Three receiver boards, B1, B2 and B3 were manufactured, where respectively three, none and one IF amplification stage is enabled. Figure 8-2 shows receiver module B3 and highlights its different stages. We want to characterize the boards within the power range covered by our in-house measurement technology and compare the results with the predictions from the system analysis. The minimum output power delivered by the equipment is -80 dBm and the maximum power around 4 dBm. Thus, B3 was fabricated to test the receiver in an optimum scenario, including IF amplification. B2 was fabricated to confirm the receiver operation up to the down-

converter. B1 was voluntarily over-designed for our measurement campaign with three IF amplification stages and fabricated to see the effect of overloading for high-gain receivers. The receivers were tested on various input frequency tones and bands, going from 33.5 to 38.5 GHz. The measurements results of B1 are presented in Annex B.

8.2 Circuit design and simulation

The receiver modules are designed on Keysight ADS and we use the same design methods used for the transmitter (cf. Section 7.2).

8.2.1 Optimization of the RF transitions

The transitions between the many SMT components are critical, as a poor transition can increase the loss significantly and can have a consequential effect on important parameters such as the return loss. This could considerably decrease the performance of each component and of the receiver in general. To ensure a good power transfer between the components, it is then necessary to optimize the transitions, especially at RF frequencies where the lines are particularly lossy.

The RF part of the receiver contains two RF connectors, a two-stage amplification, where each LNA is followed by an attenuator, as well as the first-stage down-conversion. Commonly, terminated circulators (isolators) are placed at the output of the LNAs to protect them from the potential damages caused by reflections passing to the amplifiers. Isolators also benefit from being low-loss. However, isolators tend to take much space on board compared to attenuators, especially if they are wide band. For example, a 25-40 GHz variable attenuator is typically 3 mm $\times$ 3 mm while a 34.5-35.5 GHz isolator is 5 mm $\times$ 5 mm [32],[51]. This is also true at higher bands (W-band). Therefore, the isolators are replaced by attenuators in the proposed design. This is done in trade-off to power level, which could be critical since the received power is usually very low.

To optimize the transitions design, we start from the component footprint design and consider the space constraint; we change the GCPW dimensions of the transition (signal line width and ground spacing) as well as the transition length to minimize the loss; we chose to use a tapered transition to improve the reflection. We EM-simulate the transitions on ADS using the trials and errors method until obtaining the minimum loss and a good matching.

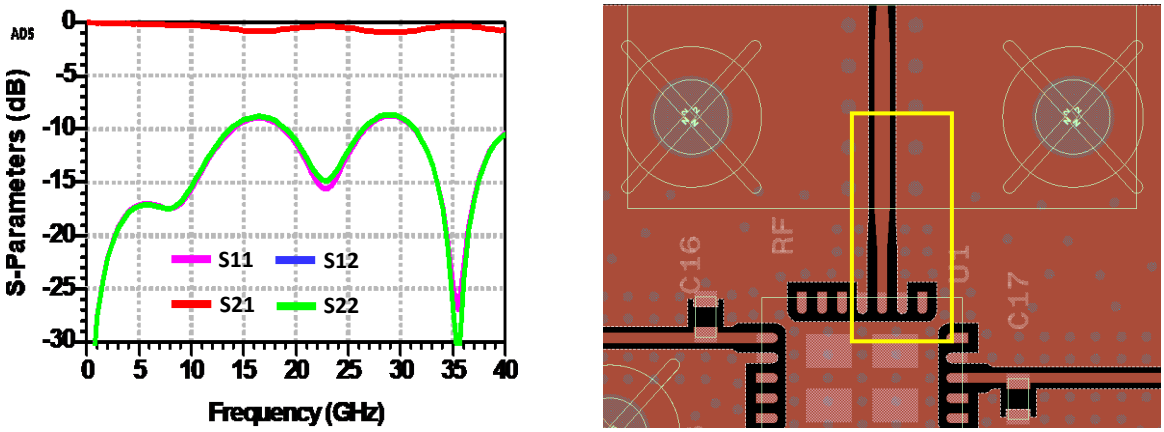

Figure 8-3: S-parameters of the transitions between the RF connector and the LNA.
The loss is 0.4 dB and the return loss is 8.6 dB.

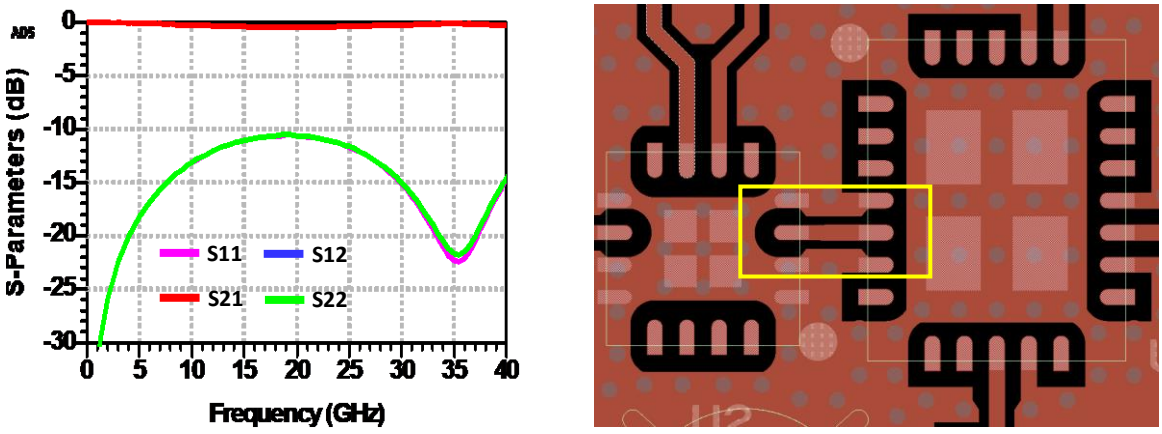

Figure 8-4: S-parameters of the transitions between the LNA and the attenuator.
The loss is 0.2 dB and the return loss is 10.5 dB.

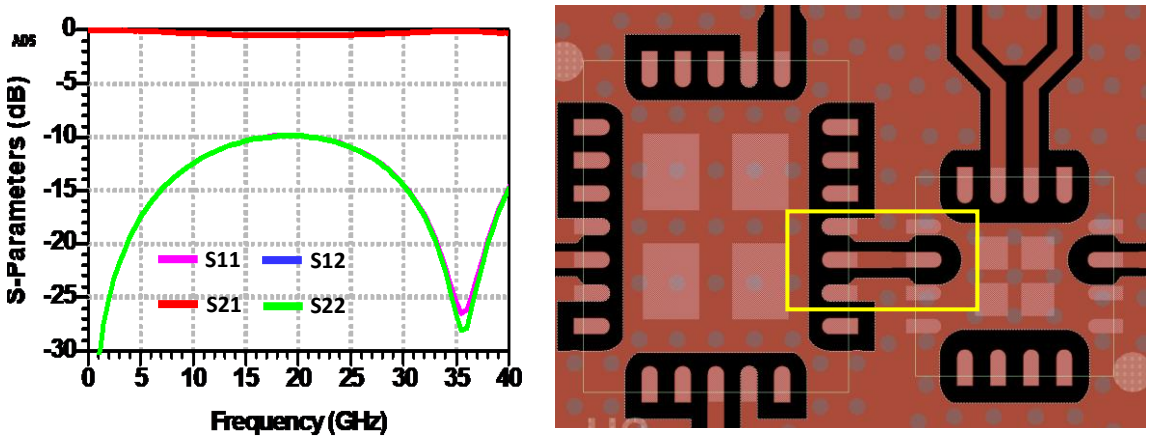

Figure 8-5: S-parameters of the transitions between the attenuator and the LNA.
The loss is 0.2 dB and the return loss is 10 dB.

Figure 8-3 to Figure 8-5 shows the simulation results for the different transitions between the RF connector and the LNA, between the LNA and the attenuator, and between the attenuator and the LNA respectively. We see that each transition between the connector up to the second attenuator is correctly matched to 35.5 GHz. The loss of a transition line is less than 0.4 dB and the return loss is minimum 8.6 dB. The transition between the last-stage attenuator and the down-converter shown in Figure 8-6 is challenging due to the many design constrains. Indeed, the device footprint should be respected to ensure a reliable and feasible soldering; the size of the transition should be minimal to decrease the loss. To avoid large reflection, we choose a full GCWG transition. This reduces inherently the gap of the line, because of the limited place between the RF line and the DC line VDRF2 to properly ground with vias (see Figure 8-6). Playing with all these parameters, we cannot properly match the line to 35 GHz. Therefore, the loss is 2.2 dB and the return loss is 8 dB. The reflection on the down-converter was expected and the simulated result is very close to the one of the datasheet [24]. The attenuator will protect the LNA in any case. In addition, the poor insertion loss was anticipated and included in the link budget as a worst-case scenario. Therefore, the simulation results are satisfactory for our radar application.

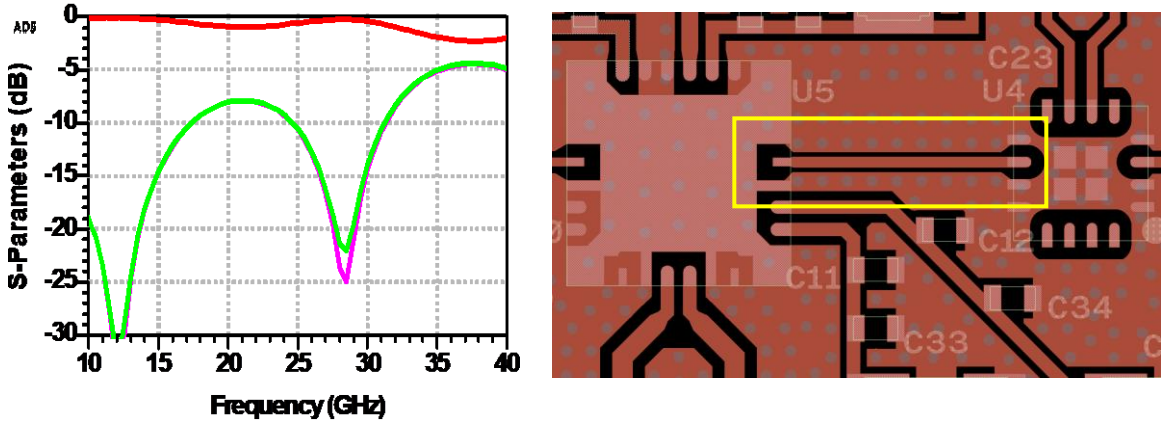

Figure 8-6: Transition between last-stage attenuator and down-converter (left) and S-parameters (right).

Dimensions of the transition line: S = 240 µm, G = 100 µm. The signal line corresponds to 65 Ohm at 35 GHz. A good matching cannot be obtained due to the spacing between the RF signal line (pad) and the DC line (pad) below. The loss is 2.2 dB and the return loss is 8 dB, in accordance with the datasheet.

8.2.2 Single sideband down-conversion

The modified Hartley architecture for down-conversion is composed of an IQ mixer, a low-pass filter at each IF output of the IQ mixer and a 90° hybrid coupler. As for the transmitter, we symmetrize the output of the hybrid to be flexible in the choice of the bandwidth. Figure 8-7 shows the structure and specifies the mounting for lower sideband conversion.

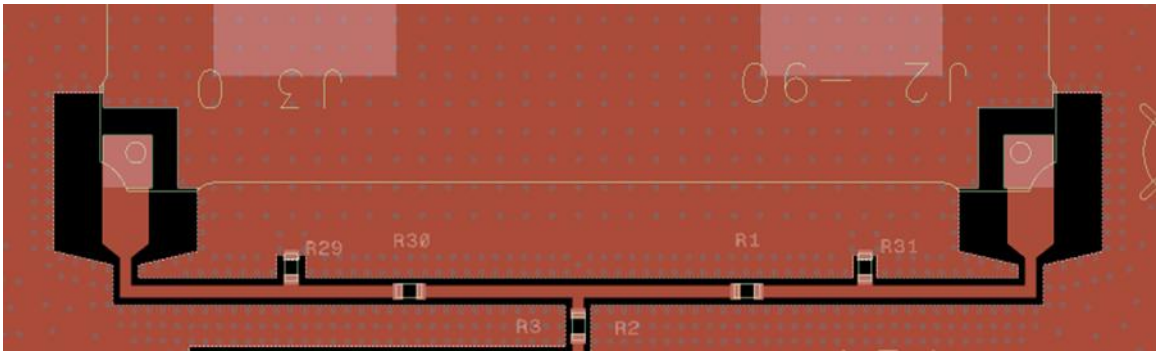

Figure 8-7: Symmetrizing the 90° hybrid output for single sideband down-conversion.

Lower sideband conversion is obtained when R33 is a 0 Ohm-resistor, R31 is a 50 Ohm resistor and R29 and R1 are left unmounted. The symmetrizing was demonstrated in Section 7.2.1

8.2.3 High-power IF amplification

The PCB can feature up to three IF amplification stages, each composed of an LNA, an LPF and an HPF. In order to adapt the amplification to the different scenarios, in addition to the classic routing going through all of the amplification stages, we create an alternative routing which

isolates each IF amplification stage. The routing is shown in Figure 8-8. The many gaps will be populated by 0-Ohm resistors (jumpers) according to the amount of amplification needed. Extra jumpers are placed very close to the junctions to avoid high reflection signals. Thus, we will populate the main route with jumpers and leave the alternative route open when we want to amplify the signal. Alternatively, we will mount the jumpers in the alternative route and leave the space open when we do not wish more amplification.

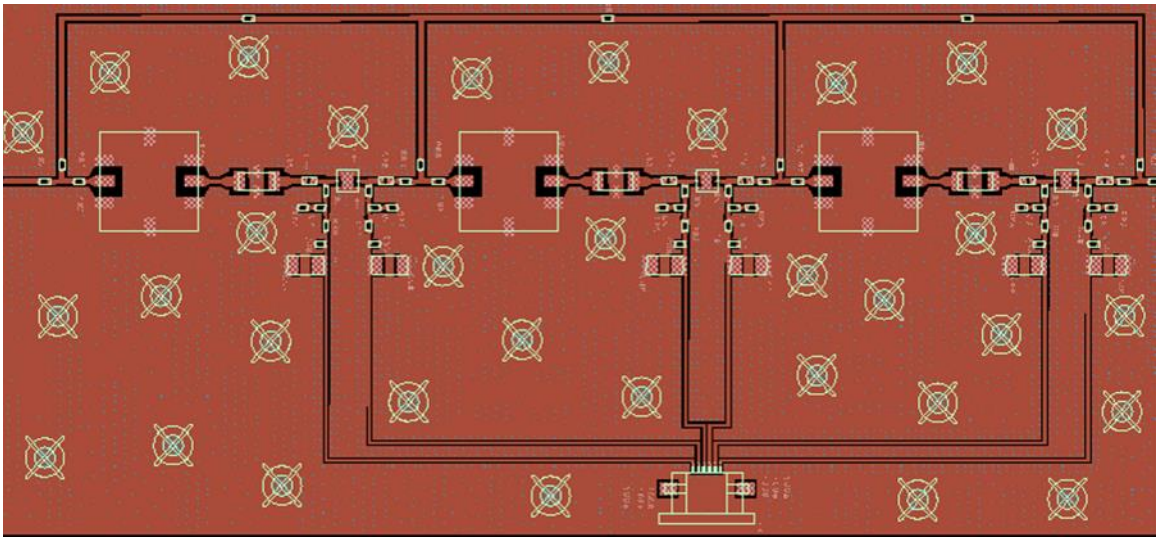

Figure 8-8: By-passing of IF amplification stages. As a rule of thumbs, the alternative route is away from the main route by about 2.5 times the size of the larger SMD

This method is also convenient to test the board subsystems and by-pass a defective amplification stage.

8.3 Measurements setups

We want to measure the output spectrum and the S-parameters to validate the design of the receiver and characterize its performance. For this purpose, we need a spectrum analyzer and a vector network analyzer respectively in two different setups.

8.3.1 Spectrum measurement set-up

Figure 8-9 shows a sketch of the setup for output spectrum measurements. The 4-port Keysight PNA-X network analyzer N5247B possesses two RF signal sources. It generates the receiver input signal (RF) and the first LO drive (LO1). The second LO drive (LO2) is generated by the MXG vector signal generator N5182B from Keysight. Finally, the output spectrum is visualized on the FSW signal and spectrum analyzer from Rhode & Schwarz. Note that the PNA-X does not

offer the spectrum analyzer option for converter measurements, hence the use of an extra spectrum analyzer.

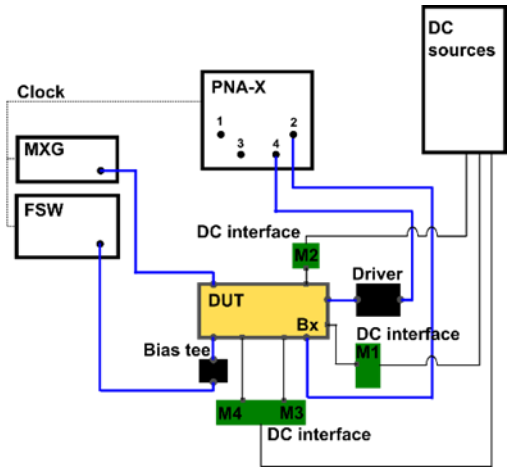

Figure 8-9: Measurement setup for spectrum measurements.
The DUT input is connected to Port 2 of the PNA-X, LO1 to Port 4 of the PNA-X, LO2 to the MXG and the output port to the FSW. Currently, the PNA-X does not support the spectrum analyzer option for mixers/ converters measurements, hence the FSW.

The RF signal power generated by the PNA-X is low (from -40 to -80 dBm) while LO1 drive is large (around 4 dBm). As for now, the PNA-X cannot generate such signals simultaneously. Thus, we set both RF and LO1 power levels low and we use the broadband RF amplifier TA0L50VA from Centellax to drive LO1 with optimal LO signal power. We favor this method instead of setting high power outputs and using external attenuators for the DUT RF input because it facilitates the measurements of input return loss and the calibration: indeed, we do not need to de-embed high-attenuation external attenuators.

To protect the FSW from potential high-power DC leakages, we place at the receiver output the bias tee BTN20050 from Marki Microwave.

8.3.2 S-parameter measurements set-up

Figure 8-10 shows a scheme of the setup for S-parameters measurements. Photos of the measurement setups are displayed in Figure 8-11. The RF and the LO1 sources are provided by the PNA-X, the LO2 source is provided by the MXG. The output is connected to the FSW for spectrum measurements and to the PNA-X for S-parameters measurements. An external amplifier drives LO1. Both PNA-X and FSW are protected from potential strong DC leakages by a bias tee. The setup is very similar to the previous one except that the receiver output is connected back to the PNA-X.

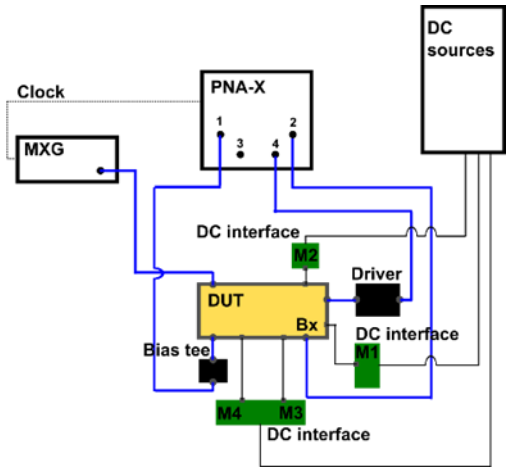

Figure 8-10: Measurement setup for S-parameters measurements.
The DUT input is connected to Port 2 of the PNA-X, LO1 to Port 4 of the PNA-X, LO2 to the MXG and the output port to Port 1 of the PNA-X.

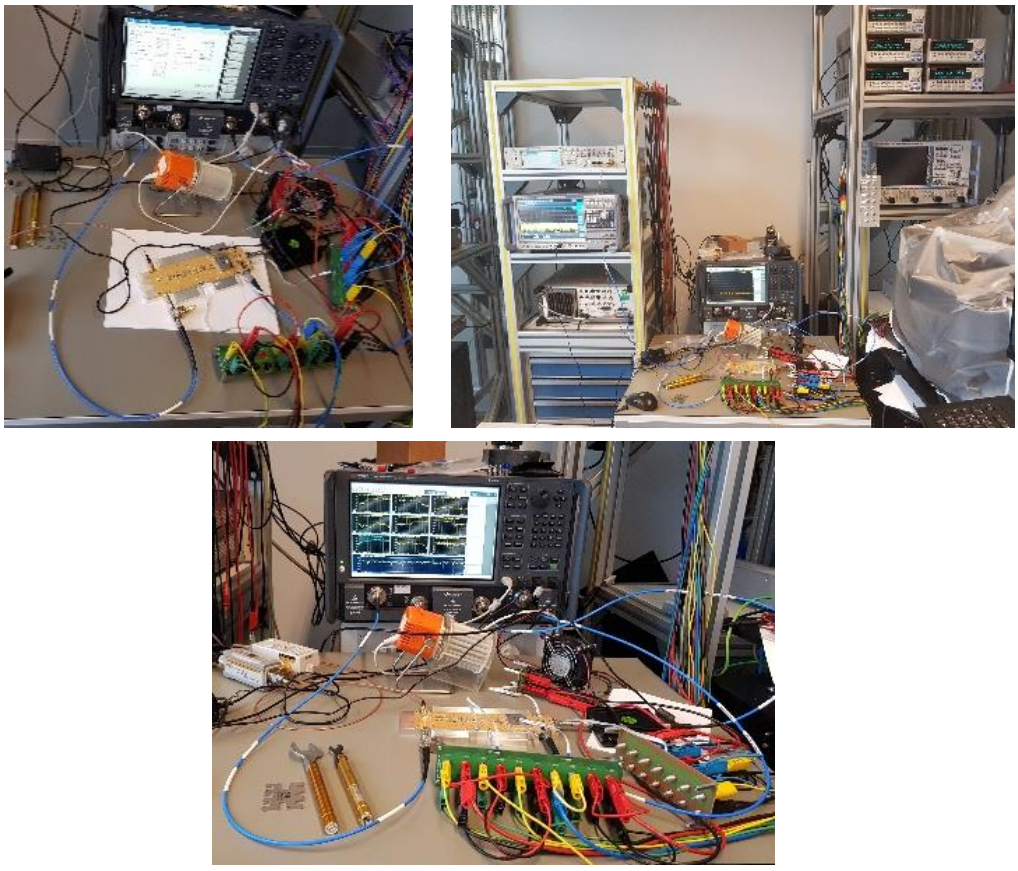

Figure 8-11: Measurement setup for S-parameters measurements

8.3.3 Biasing network and power verification

The receiver boards contain many active components and therefore large number of DC feeds. We would need a total of 19 sources to control each DC bias. We do not wish to gather so many sources but we would need to be able to test and control each component separately to see if voltages are correctly applied and if currents are properly drained.

Here, we developed interface boards external to the Rx boards that contain all the DC bias circuitry. The DC interfaces are shown in Figure 8-12. They are built on FR4 substrate. We use 6-pin and 8-pin WR-FPC SMT ZIF horizontal low-profile connectors, part numbers 687106183722 and 687108183722 from Würth Elektronik on both receiver boards and interfaces, and connect them with corresponding WR-FF6 0.5 mm flat flexible cables (FFC) of type 2, part numbers 6877062000002 and 6877082000002 from Würth Elektronik. The DC lines of the interfaces leads to 4-mm banana sockets. We test each active device separately and determine the different gate voltages. Then, we simplify the biasing network by connecting all equal voltages together. With this technique, we manage to reduce the number of DC sources to 9. Also, having external DC interfaces avoids overmanipulating and damaging the DUT.

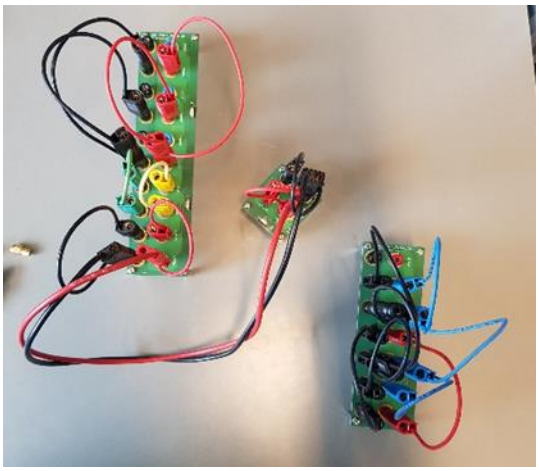

Figure 8-12: DC interfaces boards.
They are connected to the Rx boards with flexible cables. The voltage simplification and biasing is directly performed on the interfaces which can be safely manipulated.

We test all components following the biasing procedures of the manufacturers [24], [32]-[34]. To bias the whole receiver, we apply first all the drain and gate voltages, then we tune the gate until recommended current is drained. The total supply current for receiver B1 is 575 mA. The total supply current for receiver B3 is 445 mA. B1 and B3 receiver boards consume 2.28 Watts and 1.63 Watts respectively.

8.4 Measurements settings and calibration method

For each measurement setup, we calibrate the PNA-X and the FSW to have the most reliable measurement data. The bias tee and the adaptors are included in each calibration.

8.4.1 Settings and calibration for output spectrum measurements

In this setup, the PNA-X is only used as power sources (cf. Figure 8-9). So as to easily change the frequency tone and the power levels of each port, we set the PNA-X measurement class to "Spectrum Analyzer".

The ideal way to determine the cable loss between the PNA-X and the DUT input is to carry out a source calibration with a compatible power meter – this was not possible at the time of measurement. Alternatively, we measured the output power at the end of the cables when the PNA-X delivers 0 dBm at different frequencies with Rohde & Schwarz NRP-Z57 thermal power sensor; the cable loss is the measured number in dB. During the receiver characterization, we compensated the loss by increasing the power delivered by the PNA-X by the same loss. For instance, if we want to have a -70 dBm input at 35 GHz, the loss of the cable is 2.7 dB so we set the PNA-X port power to -67.3 dBm.

To determine the cable loss between the DUT output and the FSW, we connect the PNA-X to the FSW, we generate IF tones with the PNA-X and we measure the received power at the FSW for each IF frequency tone. The output cable loss is then compensated in post-processing.

8.4.2 Settings and calibration for CW Time measurements

To measure the S-parameters using continuous time sweep, we set the PNA-X measurement class to "Scalar Mixer/Converter + Phase". We chose the CW Time sweep option. In the Mixer Setup settings, we specify to the PNA-X that the DUT is a 2-stage converter. The DUT input is Port 2, the output is Port 1, LO1 is Port 4 and has a ×2 multiplier and LO2 is the external LO source. In the Power settings, the power level of the DUT input port is -40 dBm and the internal source attenuation is automatically set to 30 dB. We keep the DUT input and output ports coupled. In the Mixer Power settings, we set the LO1 to -26 dBm (this will give a 4 dBm LO1 after amplification). LO2 is delivered by the MXG, which is controlled by the PNA-X and is set to 10 dBm. In the Mixer Frequency, we set different single tone RF from 33.5 GHz to 38.5 GHz. LO1 is 18 GHz and LO2 is 950 MHz. We select the lower sideband conversion. The output frequency is automatically calculated by the PNA-X. Because the PNA-X output power is low, we reduce the IF bandwidth to 100 Hz. Span is about 1.7832 s. We chose the pre-sweep leveling option.

With these settings, we follow the guided Smart Cal of the PNA-X. The calibration settings consider no receiver attenuator and 0 dBm source calibration. We do not calibrate the LO. We

calibrate port 1 with Maury calibration kit model 8770C for 2.92mm female connectors and Port 2 with Keysight electronic calibration module model N4693-60001 for 2.4 mm female connectors. Port 1 source calibration uses U8485A power meter from Keysight. Port 2 source calibration uses U8488A power meter from Keysight. For B1, Port 2 power is calibrated with -70 dBm including 50 dB attenuation pre-settings. For B3, Port 2 power is calibrated with -40 dBm including 30 dB attenuation pre-settings. We do not recalibrate the port power when we modify it, as losses through the cables should be linear and the PNA-X automatically corrects it. The effect of the change of attenuator within the PNA-X is also automatically corrected.

8.4.3 Settings and calibration for Linear Frequency measurements (PNA-X)

We use the same measurement class option but change the sweep to Linear Frequency. The settings for the Mixer Setup, Power and Mixer Power stay the same. We change the Mixer Frequency settings to have a frequency band at the DUT input and output. RF frequency bands are chosen so that IF and LO2 bands do not overlap as the PNA-X does not permit it for a low-side mixer at the time of development.

We use the same calibration method than for the CW-Time measurements.

8.4.4 Measurements uncertainty

For few measurements, there is a problem of source leveling at the PNA-X which has remained unsolved as for now.

8.5 Measurement results

We present the measurements for the optimum case scenario, B3 mostly. Note that the spectrum analyser and the vector network analyser both operate in narrow band. Therefore, the measurements will not be affected by a poor receiver sensitivity.

8.5.1 Output spectrum

Figure 8-13 shows the output spectrum of receiver board B3, for the carrier frequency, 35 GHz and its corresponding image, 37 GHz. LO2 is 950 MHz and is well within the frequency range of the radar reference signal for deramping, i.e. [0.2-1.25 GHz].

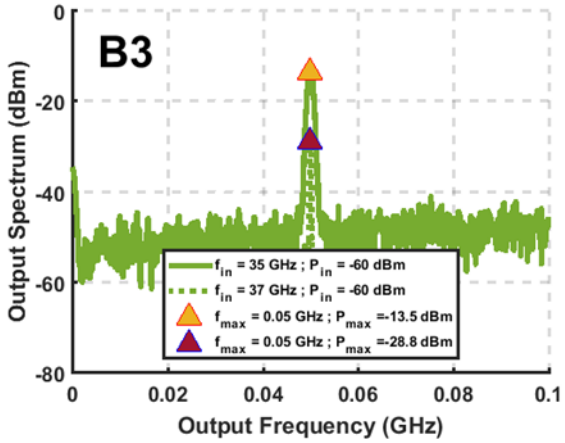

Figure 8-13: Receiver B3 output spectrum measured with the FSW (LO1 = 18 GHz, LO2 = 950 MHz).

In Figure 8-13, we see that the signal is correctly down-converted by the receiver B3. The conversion gain of receiver B3 is 47.4 dB, measured at 35 GHz for a -60 dBm input power at instantaneous time which is in accordance with the link budget calculated in the worse-case scenario. The sideband suppression is 15.3 dBc.

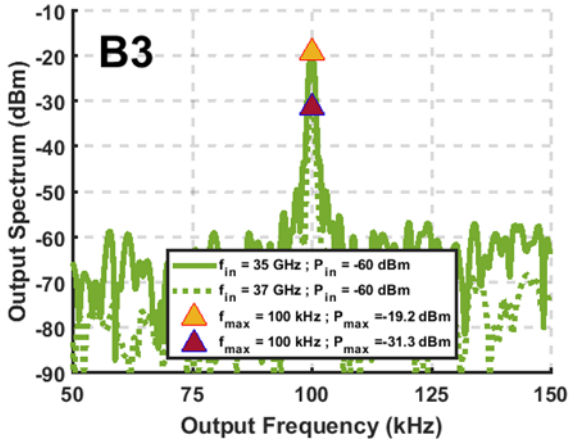

Figure 8-14: Receiver B3 output spectrum measured with FSW (LO1 = 18 GHz, LO2 = 999.9 MHz).

Figure 8-14 shows the output spectrum for very low output frequencies for the carrier at 35 GHz and its image. 100 kHz is the typical beat frequency which should be detected in our radar application. To read such output spectrum, it is necessary to disable the embedded bias tee of the FSW. In this case, the FSW embedded calibration is not valid anymore and the manufacturer warns that the results are not reliable. We see that the receiver output power – and therefore the total conversion gain is lower than when LO2 is 950 MHz. The gain drops to 40.8 dB and the sideband suppression is around 12.1 dBc. Note that the bias tee BTN20050 connected at the Rx

output operates from 3 MHz to 50 GHz: it might filter out the 100 kHz output. Finally, the conversion gain of the mixer can also differ depending on the LO2. This could explain that the output power is lower than expected.

8.5.2 Conversion gain

We further calculate the conversion gain of the different boards by measuring the transmission parameters S12 of the boards at different input frequencies and input powers, with a CW Time sweep. Figure 8-15 is an example of such measurements on receivers B2 and B3. We see that the S12 parameter does not fluctuate much over time and averages 27 dB for B2, and 47 dB for B3. This matches the expected gains of both receivers at different stages and validates the system analysis. For each measurement, the gain is the mean of S12 over time. Figure 8-16 shows the conversion gain of board B3. It is 45 dB typically, as expected by the link budget. We see that the conversion gain depends on both input power and on input frequency. The receiver is the most efficient between 34.5 and 35.8 GHz and the curve is relatively flat. Within this band, we see that B3 saturates around -40 dBm as the conversion gain drops by 5-10 dB. This is expected as B3 overloads at -38.5 dBm input (cf. Table 3-5). Figure 8-17 shows the conversion gain calculated from the output spectrum. The conversion gain is the difference between the peak of the output IF signal and the input power. The curves match the previous measurement quite well and slightly differs due to the noise fluctuation during spectrum measurements.

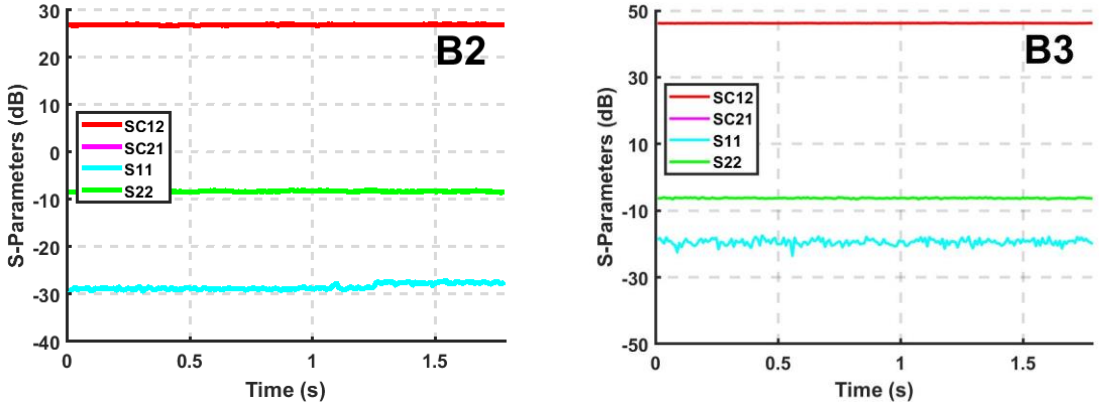

Figure 8-15: S-parameters of B2 and B3 measured in continuous time with PNA-X at 35 GHz.
For B2, the input power is -40 dBm and the gain is 27 dB. For B3, input power is -60 dBm and the gain is 47 dB. Both results are in full compliance with predictions from Table 3-5

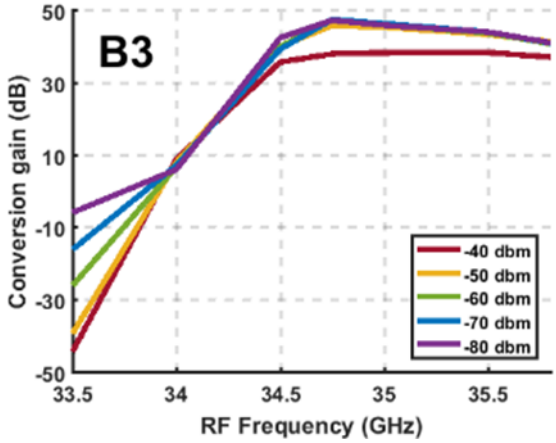

Figure 8-16: Conversion gain measured with PNA-X on CW Time sweep at different input powers

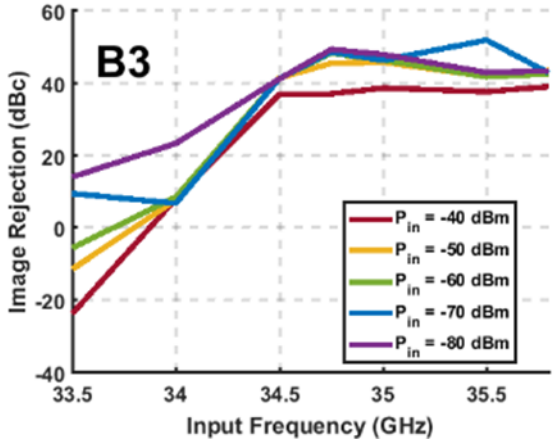

Figure 8-17: Conversion gain measured with FSW at different input powers

8.5.3 Sideband Suppression

We measure the upper sideband suppression in two ways. With the PNA-X, we measure S12 parameters in CW Time for different input carriers and their corresponding image frequencies. We average all S12 measurements over time. The image suppression is the ratio between the carrier and its corresponding image frequency. With the FSW, we measure the peak of the output IF for both input carrier and image frequency. The sideband suppression is the difference between both peaks. Note that we do not need to account for the loss of the cable since it will cancel out in the ratio. Figure 8-18 show the image suppression for board B3. The order of magnitude for both measurement types is quite constant: within the 34.5-35.8 GHz range, the suppression is between 1 and 13 dBc. -40 dBm input saturates and the conversion is not as

effective. We can also see that the sideband suppression drops around 35.5 GHz. Both measurements do not properly match because the sideband suppression calculated from the PNA-X CW time measurements are results of a mean over the time sweep, while curves calculated from FSW spectrum result from a snapshot at a given time. Spectrum measurements with FSW fluctuate because of the noise. This is especially true for low power measurements. Measurements with PNA-X are more reliable. Note that the image rejection is less than in HMC6789BLC5A datasheet because first, the down-converter operates out-of-range; second, the lower sideband conversion does not perform as well as the USB.

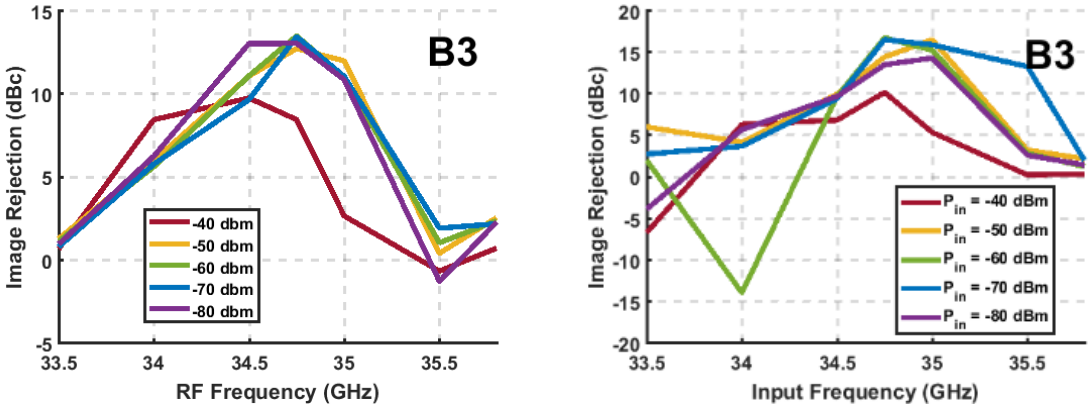

Figure 8-18: Image rejection of B3 measured with PNA-X (left) and with the FSW (right) at different input powers.

8.5.4 Power performance

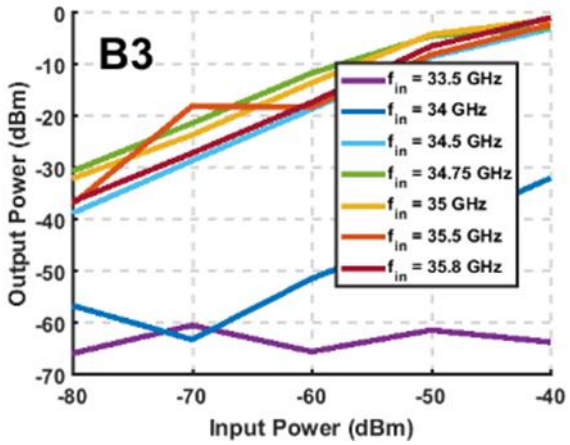

Figure 8-19: Output power vs. input power measured with the FSW at different input frequencies.

Figure 8-19 shows the output power with respect to the input power for B3 at different frequencies. The output power is measured with the FSW and is once again a snapshot. However, we can see that the output power is much larger for frequencies above 34.5 GHz. This corroborates that the receiver operates at its best between 34.5 and 35.8 GHz. We also see that the curves above 34.5 GHz are mostly linear, and breaks at -40 dBm input, which shows again that the receiver starts saturating.

8.5.5 Bandwidth characterization and feasibility validation for FMCW radar

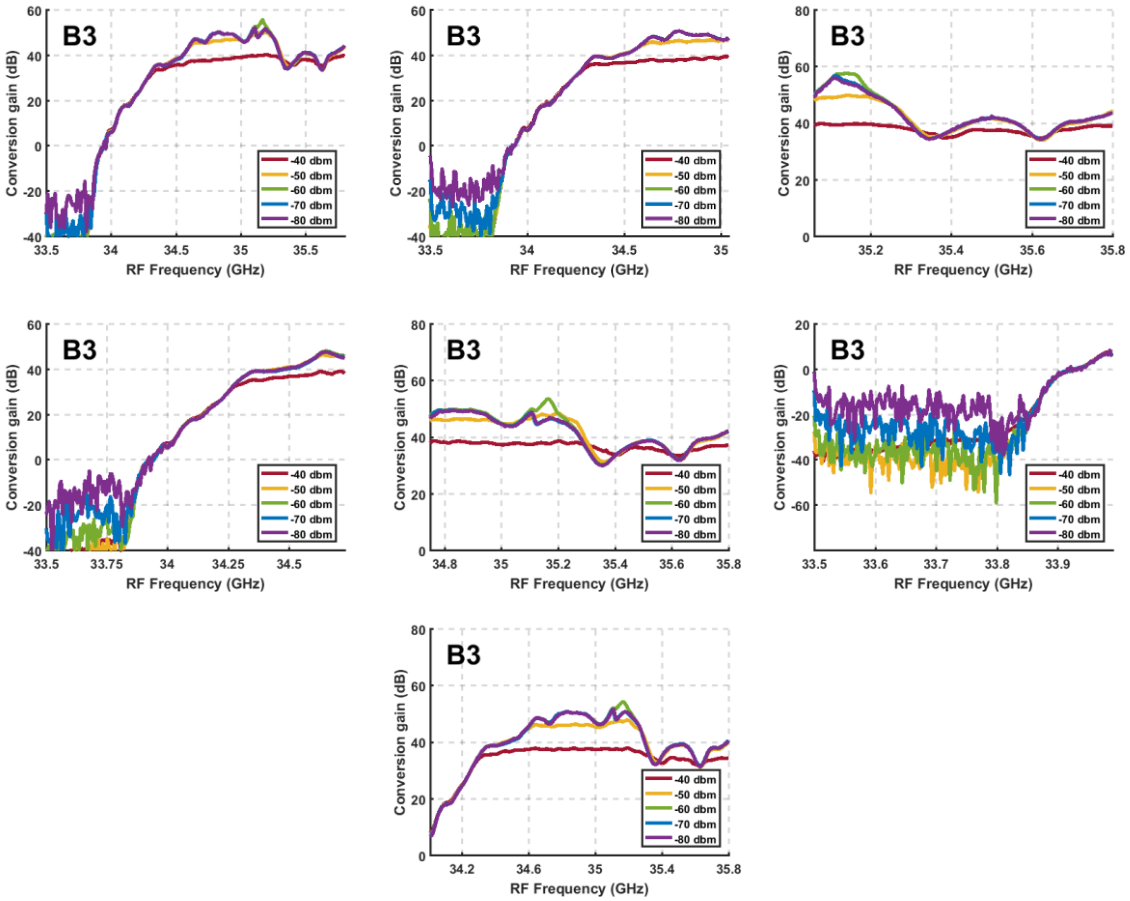

Figure 8-20: S-parameters of board B3 measured with PNA-X on Linear Frequency sweep at different input powers

when LO1 = 18 GHz and: 1) RF = [33.5-35.8] GHz, LO2 = 190 MHz; 2) RF = [33.5-35.04] GHz, LO2 = 950 MHz; 3) RF = [35.06-35.8] GHz, LO2 = 950 MHz; 4) RF = [33.5-34.73] GHz, LO2 = 1260 MHz; 5) RF = [34.75-35.8] GHz, LO2 = 1260 MHz; 6) RF = [33.5-33.99] GHz, LO2 = 2000 MHz; 7) RF = [34.01-35.8] GHz, LO2 = 2000 MHz.

We want to characterize the bandwidth of the receiver for the whole spectral band allocated for wind-turbine structural health measurements, between 33.5 and 35.8 GHz, using the Linear

Frequency sweep option of the PNA-X, at different LO2 frequencies. The LO2 frequencies are taken at the edges (190 MHz and 1260 MHz), at the center (950 MHz) and above (2000 MHz) the bandwidth of the reference signal for the radar deramp which is 200-1250 MHz. In most cases, it is not possible to measure the full bandwidth in one single measurement because PNA-X does not permit the LO2 and the output IF signal to overlap. Therefore, we separate the RF bandwidth in two to avoid that overlapping, as described in Figure 8-20.

First, we see that all curves follow the same pattern and are constant, independently of LO2 frequency. This means that the receiver boards will be adequate for FMCW radar deramping. Second, we see that the S12 is very low and noisy below 33.85 GHz. S12 smoothens and significantly increases above 34.1 GHz and flattens around 34.3 GHz up to 35.8 GHz. This confirms that the receiver bandwidth is 34.3-35.8 GHz. Third, the curves of the conversion gain measured in Continuous Time, snapshot (FSW) and Linear Frequency sweep all match. We can recognize the same pattern: -40 dBm input power saturates the receiver, all other input powers give very similar curves and -50 dBm input is slightly lower than the rest. Conversion gain goes up to 50 dB.

8.5.6 Input return loss

Figure 8-21 shows the input return loss of B3 measured at different input powers. We see that the input is well matched round 34.75 and 35.15 GHz. The return loss is less than 9 dB over the receiver bandwidth. These results match the EM-simulated one. We also see that return loss can only be measured correctly at -40 dBm at least. Otherwise, the return power is too low and the PNA-X cannot read it.

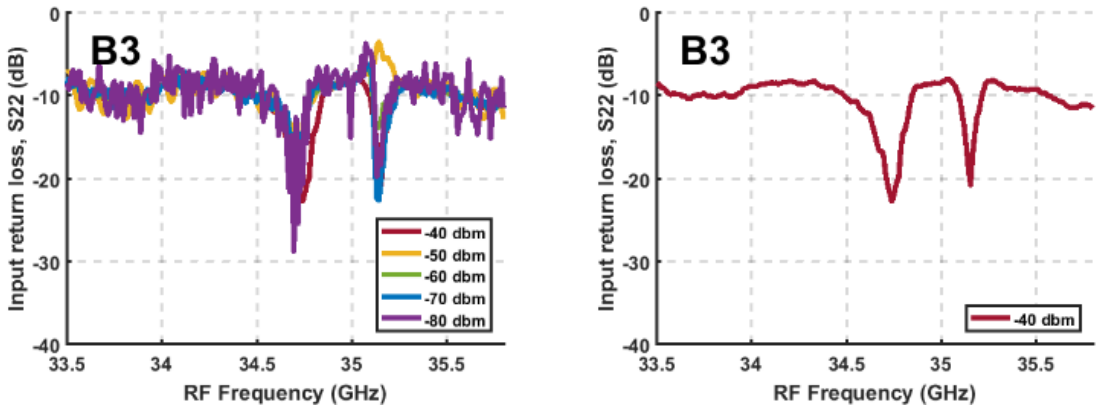

Figure 8-21: Input return loss (S22) of B3
measured with PNA-X on Linear Frequency sweep at different input powers (left) and at -40 dBm (right), when RF = [33.5-35.8] GHz, LO1 = 18 GHz and LO2 = 190 MHz

8.5.7 Output return loss

Likewise, we have to increase port 1 power to at least -40 dBm to measure the reflection at the output. Figure 8-22 shows the output return loss. It is below 9 dB over the band.

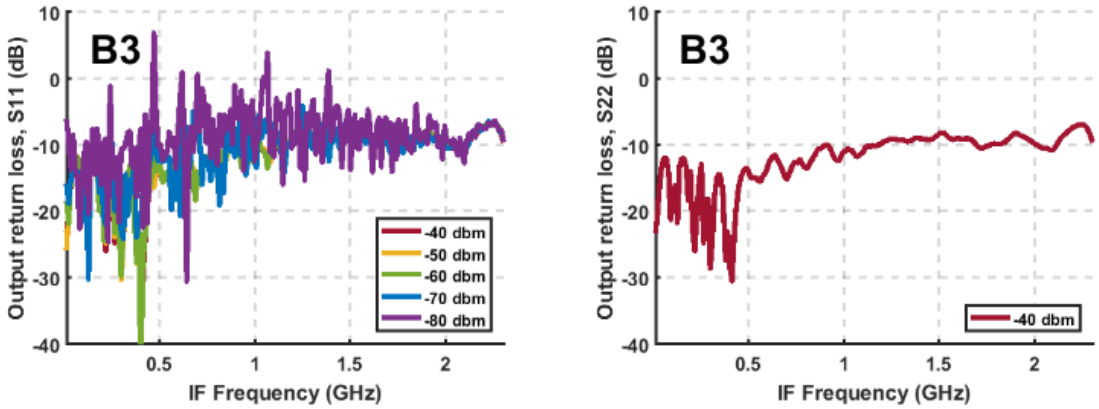

Figure 8-22: Output return loss (S11) of B3
measured with PNA-X on Linear Frequency sweep at different input powers (left) and at -40 dBm (right), when RF = [33.5-35.8] GHz, LO1 = 18 GHz and LO2 = 190 MHz

8.5.8 Spurious free dynamic range (SFDR)

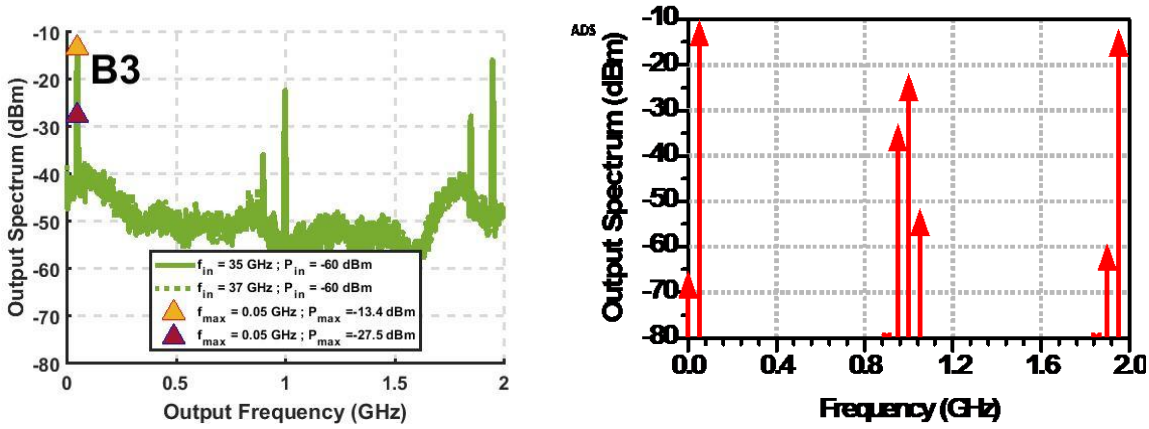

Figure 8-23: Output spectrum of B3, measured (left) vs. simulated (right) at -60 dBm input power.
Input frequency is 35 GHz, LO1 is 18 GHz and LO2 is 950 MHz. One reason measured output power is slightly lower than simulated is the output cable loss. SFDR is around 10 dBc.

Figure 8-23 shows the output spectra of receiver board B3 on a wider frequency band and compared to simulated output on ADS. The simulation uses close-to-reality component model based on Hammerstein-Wiener model, as described in Section 4.1. The input carrier frequency is a single tone at 35 GHz and LO2 is 950 MHz. We see that measured and simulated results match. There is a strong IF leakages because of low IF-DC isolation of mixer ADE-R5LH+. The SFDR is

limited by the LO leakage and is around 10 dBc typically, which is a very satisfactory result for our radar application.

8.6 Summary and remarks

We developed and characterized a variable-gain receiver prototype at 35 GHz, based on our fully-simulated novel architecture. We designed the receiver boards and optimized critical points including the RF transitions, the single sideband conversion and the variable IF gain. We presented the measurement results in the case when the board comprises one IF amplification stage, using several measurement methods. The performance of the receivers is summarized in Table 8-1. The results of the different measurements were constant despite the different measurement methods. The proposed receiver has a bandwidth of 34.3-35.8 GHz. The conversion gain is 45 dB typically, relatively flat over the input frequency and constant over the reference signal or LO for deramping. This predicts a good signal integrity. The image rejection is 7 dBc typically. The input and output return loss are 9 dB. The SFDR is 10 dBc. This testifies of a sufficient spectral purity. The measurement results are in total accordance with the anticipated performance of the receiver simulated and calculated in link budget. This validates the feasibility study of the proposed novel radar receiver and shows that the receiver board is perfectly adequate for FMCW radar application between 34.3 and 35.8 GHz.

Table 8-1: Summary of measured Rx performance of B3

Parameters	Min.	Typ.	Max.	Units
RF Frequency Range	34.3		35.8	GHz
LO1 Frequency Range		18		GHz
LO2 Frequency Range	190		2000	MHz
IF Frequency Range	0.1		1800	MHz
Conversion Gain	30	45	50	dB
Image Rejection	1		13	dBc
Input Return Loss		9		dB
Output Return Loss		9		dB
SFDR		10		dBc
Supply Power		1.63		W
LO1 Drive Range		4		dBm
LO2 Drive Range		10		dBm
PCB Size		5.64 × 19.56		cm × cm

Chapter 9

Conclusions and outlook

We proposed an advanced millimeter-wave FMCW radar system towards highly integrated front-ends for high-resolution imaging applications. The architecture limits the use of off-chip high-order bandpass filters by comprising a modified Hartley architecture for image suppression and an enhanced push-pull architecture for second-order harmonics cancellation. The signal generation is based on novel frequency- and phase-controlled direct digital synthesis. This allows the implementation of CDM-based MIMO radar architecture using intra-pulse modulation. We modulated the chirp in phase at each transmitter using quasi orthogonal codes. It is then possible to identify the channel to a specific transmitter by simply deramping the received signal with a chirp modulated with the same code as used for this very transmitter and estimate the range. The demonstration of the proposed MIMO FMCW radar architecture was performed from theory development, through system level design to hardware characterization, for a 35 GHz radar of 1 GHz-bandwidth, enabling a 15 cm range resolution. The developed radar serves as a prototype for future higher frequency systems.

The performance of the radar before post-processing was evaluated in an extensive link budget and system analysis. To correctly predict the radar hardware performance, the input RF connector of the receiver module was taken into account. The gain of the receiver is variable and ranges between 27.5 and 80 dB. The receiver noise is 6.28 dB, mostly impacted by the input RF connector. The sensitivity is -62.4 dBm, the MSD is -74.4 dBm. The minimum dynamic range is 0.9 dB, in the case of high-gain receiver, which shows that the radar can always detect the signal. The sensitivity of the receiver can be improved by sending a narrow band signal, at the cost of the range resolution, which is not viable for high-resolution imaging applications. The link performance is thereby improved by increasing the transmitted power or carrying out post-processing integration.

We developed a radar simulation environment emulating realistic datasheet-based device performance. We used an innovative 3D electromagnetic propagation model to account for the antenna and wave propagation to the target. With the above architecture we expect to achieve

a conversion image rejection of -53.5 dBc with an output power above 34 dBm across 1 GHz bandwidth, using various commercial components. A spectral purity less than -130 dBc should be achieved for the 2nd and 3rd order harmonic suppression, respectively. The total DC consumption is around 30 W determined by the power amplifiers.

We discussed the performance of a code-division based FMCW MIMO radar for imaging applications. We compared the implementations of coding techniques using intra-pulse modulation based on BPSK and QPSK, utilizing Gold sequences of different lengths. For a 8×1 MIMO radar of initial baseband frequency 0.2 GHz, bandwidth 1 GHz and chirp duration 500 μs, it was shown that the range estimation is the most accurate when the code rate is between 254 kHz and 8.19 MHz for short-range, and between 126 kHz and 1.022 MHz for mid-range detection. Each signal from the different transmitters can be recovered and the different ranges estimated with a peak-to-sidelobe ratio above 6 dB.

The feasibility of our proposed MIMO model was further demonstrated at 90 GHz, for a 16 mm-resolution FMCW radar of bandwidth 9.5 GHz and a chirp duration of 500 μs. We presented a step-by-step system simulation of the radar, using Gold sequences. The full radar system could differentiate the transmitters and recollect the range as well as a SISO radar with an error of maximum 0.42%, and a 13 dBc PSR. Such as for SISO systems, the detection is deteriorated by the use of bandpass filters, the error dropping to 0.11% when the radar does not comprise any. This makes the proposed highly-integrable architecture all the more interesting for highly-reliable high-resolution imaging applications.

We manufactured and characterized a transmitter and a receiver module at 35 GHz. The transmitter bandwidth is 34.3-35.8 GHz. The measurement results of the transmitter subsystems are satisfactory. The conversion gain of the up-converter is 7 dB, the upper-sideband image cancellation is 10 dBc, the LO suppression is above 30 dBc. The bandpass filter has an insertion loss of 5 dB, an input and output return loss of 9 dB, and its fractional bandwidth is 8%. The output power of the push-pull during saturation is 31.3 dBm which is lower than simulated, due to the unavoidable large size of the hybrid on board. The output power of the full transmitter chain is 24 dBm measured with the output spectrum at 35 GHz and 27 dBm calculated from the S-parameters. The image suppression and the LO suppression are above 20 dBc. The input and output return loss are 15 dB. The output power measurements of the full transmitter chain did not match the subsystem measurements, probably due to a sudden defect on the board.

The proposed receiver has a bandwidth of 34.3-35.8 GHz. The conversion gain is 45 dB typically and constant over the reference signal or LO for deramping. The image rejection is 7 dBc typically. The input and output return loss are 9 dB. The SFDR is 10 dBc. The measurement results are in total accordance with the anticipated results from the system analysis.

The measurement results verified the predictions from the simulations and confirmed that our highly-integrable novel architecture is a viable candidate for mm-wave high-resolution FMCW radar application at larger bands, in the W-band and above.

In a next work, the transmitter hardware could be improved by featuring power amplifiers with single-sided DC feeds to reduce the size of the push-pull architecture and improve the output power. The full radar, including LO generation, could be tested in lab and field environments. The MIMO FMCW radar detection can be further improved by using more orthogonal codes to decrease the sidelobes. Finally, the proposed architecture could be implemented on a single chip in the W-band and tested for final system validation.

Bibliography

[1] Leddartech website, “https://www.leddartech.com,” [Accessed 12 03 2022]

[2] C. Wolff, 1998, “https://radartutorial.eu”, [Accessed 12 3 2022]

[3] N. Sarmah, J. Grzyb, K. Statnikov, S. Malz, P. Vazquez, W. Förster, B. Heinemann and U. Pfeiffer, “A fully integrated 240 GHz direct conversion quadrature transmitter and receiver chipset in SiGe technology,” IEEE Transactions on Microwave Theory and Techniques, vol. 64, no. 2, pp. 562-574, 2016.

[4] M. Hitzler, S. Saulig, L. Boehm, W. Mayer, W. Winkler, N. Uddin and C. Waldschmidt, “Ultracompact 160-GHz FMCW radar MMIC,” IEEE Transaction on Microwave Theory and Techniques, vol. 65, no. 5, pp. 1682-1691, 2017.

[5] M. Furqan, F. Ahmed, R. Feger, K. Aufinger and A. Stelzer, “A 120- GHz wideband FMCW radar demonstrator based on a fully-integrated SiGe transceiver with antenna-in-package,” in 2016 IEEE MTT-S International Conference on Microwaves for Intelligent Mobility (ICMIM), San Diego, CA, 2016.

[6] J. Yu, F. Zhao, J. Cali, F. F. Dai, D. Ma, X. Geng, Y. Jin, X. Jin, D. Irwin and R. Jaeger, “An X-band radar transceiver MMIC with bandwidth reduction in 0.13 um SiGe technology,” IEEE Journal of Solid-State Circuits, vol. 49, no. 9, September 2014.

[7] “IQ, image reject & single sideband mixer primer,” [Online]. Available: http://www.markimicrowave.com/ [Accessed 18 07 2022]

[8] A. Haider, A. Eryildirim, M. Thumann, T. Zeh and S. -A. Schneider, "Influence of RF Group Delay on the Performance of FMCW Automotive Radar Sensor," 2021 IEEE 21st Annual Wireless and Microwave Technology Conference (WAMICON), 2021, pp. 1-6.

[9] Z. Peng, D. Psychogiou and C. Li, "Investigation of the roles of filters for a harmonic FMCW radar," 2017 International Applied Computational Electromagnetics Society Symposium (ACES), 2017, pp. 1-2.

[10] F. Belfiori, N. Maas, P. Hoogeboom and W. van Rossum, "TDMA X-band FMCW MIMO radar for short range surveillance applications," in 5th European Conference on Antennas and Propagation (EUCAP), Rome, 2011.

[11] D. Cohen, D. Cohen and Y. C. Eldar, "High resolution FDMA MIMO radar," 16 11 2017. [Online]. Available: arxiv.org/pdf/1711.06560.pdf. [Accessed 11 02 2018].

[12] H. Haderer, R. Feger, C. Pfeffer and A. Stelzer, "Millimeter-Wave Phase-Coded CW MIMO Radar Using Zero- and Low-Correlation Zone Sequence Sets," in IEEE Transactions on Microwave Theory and Techniques, vol. 64, no. 12, pp. 4312-4323, Dec. 2016.

[13] A. Shrestha, J. Moll, A. Raemer, M. Hrobak and V. Krozer, "20 GHz Clock Frequency ROM-Less Direct Digital Synthesizer Comprising Unique Phase Control Unit in 0.25 µm SiGe Technology," 2018 13th European Microwave Integrated Circuits Conference (EuMIC), Madrid, 2018, pp. 206-209.

[14] A. Shrestha, J. Moll and V. Krozer, "Wideband Doppler Radar Using a 18.5 GHz Microwave Direct Digital Synthesizer," *2020 21st* International *Radar Symposium (IRS)*, 2020, pp. 308-311.

[15] J. Moll and V. Krozer, "A novel receiver architecture for spread spectrum MIMO-radar systems," in 2012 9th European Radar Conference, Amsterdam, 2012.

[16] K.-W. Gurgel and T. Schlick, “Remarks on Signal Processing in HF Radars Using FMCW Modulation,” 2018

[17] G. Babur, O. A. Krasnov, A. Yarovoy and P. Aubry, "Nearly Orthogonal Waveforms for MIMO FMCW Radar," in *IEEE Transactions on Aerospace and Electronic Systems*, vol. 49, no. 3, pp. 1426-1437, July 2013.

[18] K. A. Farell and P. J. McLane, “Performance of the cross-correlator receiver for binary digital frequency modulation,” *IEEE Transactions on Communications,* vol. 45, no. 5, pp. 573-582, May 1997.

[19] U. K. Majumder, “Nearly orthogonal, Doppler tolerant waveforms and signal processing for multi-mode radar applications,” PhD. thesis, Purdue University, West Lafayette, IN, USA, Aug. 2014.

[20] W. Smidth and A. Egido, “Fully focused SAR altimetry: theory and applications,” IEEE Transactions on Geoscience and Remote Sensing, vol. 55, no. 1, pp. 392-406, January 2017.

[21] “TGC4546-SM: 36-45 GHz upconverter with quadrupler,” [Online]. Available: http://www.qorvo.com/ [Accessed 27 11 2018].

[22] “IPP-7116: SMD coupler, 90°, 225-2000 MHz, 200W,” [Online]. Available: http://innovativepp.com/ [Accessed 30 11 2018].

[23] “LFCN-1575: low pass filter,” [Online]. Available: http://www.minicircuits.com/ [Accessed 03 12 2018].

[24] “HMC6789BLC5A: GaAs MMIC I/Q downconverter 37-44 GHz,” [Online]. Available: https://www.analog.com [Accessed 30 05 2021].

[25] “HMC7229LS6: GaAs pHEMT MMIC 1 Watt power amplifier with power detector, 37-40 GHz,” [Online]. Available: http://www.analog.com\ [Accessed 03 12 2018].

[26] “Model D10AAXXZ4: surface mount attenuator,” [Online]. Available: http://www.anaren.com [Accessed 30 11 2018].

[27] “C04/C06/C08 broadband DC blocks: low loss resonance free performance,” [Online]. Available: http://www.knowlescapacitors.com/ [Accessed 30 11 2018].

[28] “HMC635LC4: GaAs pHEMT MMIC driver,” [Online]. Available: http://www.analog.com\ [Accessed 30 11 2018].

[29] “NCS-122+: RF transformer,” [Online]. Available: http://www.minicircuits.com/ [Accessed 30 11 2018].

[30] “1492-04A-6: 2.40mm Jack (female) end launch connector low profile,” [Online]. Available: http://mpd.southwestmicrowave.com/ [Accessed 03 12 2018].

[31] “901-10512-1, high freq end launch SMA jack assembly, PC mount, 15 mil pin,” [Online]. Available: http://www.amphenolrf.com/ [Accessed 03 12 2018].

[32] “CHT4694-QAG: 25-40 GHz Attenuator, GaAs MMIC in SMD leadless package,” [Online]. Available: https://www.ums-rf.com [Accessed 30 05 2021].

[33] “CHA2494-QEG: 34-44 GHz LNA, GaAs MMIC in SMD leadless package,” [Online]. Available: https://www.ums-rf.com [Accessed 30 05 2021].

[34] “HMC8410: 0.01-10GHz, GaAs, pHEMT, MMIC, LNA,” [Online]. Available: https://www.analog.com [Accessed 30 05 2021].

[35] “RHP-65+: high pass filter,” [Online]. Available: https://www.minicircuits.com [Accessed 30 05 2021].

[36] “ADE-R5LH+: high reliability mixer,” [Online]. Available: https://www.minicircuits.com [Accessed 30 05 2021].

[37] “292-07A-6: SMA Jack (female) end launch connector low profile,” [Online]. Available: http://mpd.southwestmicrowave.com/ [Accessed 03 12 2018].

[38] R Hartley, Modulation System US patent 1666206 Apr (1928).

[39] Sorin Voinigescu, “High-frequency integrated circuits,” Cambridge University Press, New York, 2013, P 594, chap. 9 Mixers, switches, and other control circuits.

[40] W. H. Lambert, "Second-order distortion in CATV push-pull amplifiers," in *Proceedings of the IEEE*, vol. 58, no. 7, pp. 1057-1062, July 1970, doi: 10.1109/PROC.1970.7849.

[41] G. Watkins, “Enhancing second harmonic suppression in a ultrabroadband RF push-pull amplifier,” High Frequency Electronics, pp. 32-40, March 2014.

[42] “Discussion on “Noise Figures of Radio Receivers” (H. T. Friis),” in Proceedings of the IRE, vol. 33, no. 2, pp. 125-127, Feb. 1945.

[43] “ADC12SJ800: ADC12xJ800 Quad, dual, single channel, 800-MSPS, 12-bit, ADC with JESD204C interface,” [Online] https://www.ti.com/product/ADC12SJ800 has Vpp = 0.8V

[44] Favier, Gerard. (2009). “Nonlinear system modeling and identification using tensor approaches (Invited paper).”

[45] “RO4000 Series: high frequency circuit materials,” [Online]. Available: http://www.rogerscorp.com/ [Accessed 27 11 2018].

[46] S.W. Wong, Z. Chen and Q.-X. Chu, “Microstrip-line millimeter-wave bandpass filter using interdigital coupled-line,” Electronics Letters, vol. 48, no. 4, pp. 224-225, 16 February 2012.

[47] H. Zhong, R. Xu and M. Zhan, “Design for Ka-band wideband bandpass filter with three-line microstrip structures,” in *2008 International Conference on Microwave and Millimeter Wave Technology*, Nanjing, 2008.

[48] L. Zhang, X. Yang, Z. Yang and Z. Ma, “Design of millimeter-wave bandpass filter using microstrip stepped-impedance stubs,” in *IET International Communication Conference on Wireless Mobile and Computing (CCWMC 2011)*, Shanghai, 2011.

[49] D. M. Pozar, Microwave Engineering, 4th Edition, New York: John Wiley & Sons, 2011.

[50] “100kHz-50GHz broadband RF amplifier,” [Online]. Available: wookoohitech.com/pages/pdf/TA0L50VA.pdf [Accessed 02 07 2022]

[51] “JIS34K5T35K6G0: microstrip isolator,” [Online]. Available: https://www.jqlelectronics.com [Accessed 30 05 2021].

Annex A

Bill of Materials

Table A-1: Transmitter bill of material (complete)

Item	Value	Description	Manufacturer	Part Number	Qty/board
J1		SMA connector	Amphenol	901-10512-1	1
J2		SMA connector	SOUTHWEST	292-07A-6	1
J3		2.4 mm connector	SOUTHWEST	1492-04A-6	1
Vxx		DC SMT pin headers	SAMTEC	TSM-136-01-F-DH	30
U1		DC-block	Dielectric Labs	C04BL121X-5UN-X0B	1
U2		3dB Attenuator	Anaren	D10AA3Z4	1
U3		Lowpass Filter	Mini-Circuits	LFCN-1575	1
U4		90° Hybrid	Innovative Power Products	IPP-7116	1
U5, U6		Balun	Mini-Circuits	NCS1-112+	2
U7		Ku-band Upconverter	Qorvo	TGC4546-SM	1
U8		Driver amplifier	Analog Devices	HMC635LC4	2
U9, U10		Power amplifier	Analog Devices	HMC7229LS6	2
C1-C24	100 pF	Cap, 0402, 50V, 5%, NPO	Knowles	0402J1000101GCB	24
C25-C28	220 pF	Cap, 0402, 50V, 5%, NPO	Knowles	0402N221J500N	4
C29-C34	1000 pF/1 nF	Cap, 0603, 50V, 2%, NPO	Knowles	0603J0500102GCB	6
C35-C52	0.01 uF/10000 pF	Cap, 0603, 25V, 5%, COG/NPO	Samsung Electro-Mechanics	CL10C103JA8NNNC	18
C53-C57, C98	1 uF	Cap, 0805, 25V, 5%, X7R	AVX	08053C105JAT2A	6
C58, C59	2.2 uF	Cap, 0805, 25V, 10%, X7R	AVX	08053C225KAT2A	2
C60-C77	4.7 uF	Cap, tantalum, Case A	Vishay	T55A475M010C0200	18
C78-C97	50 GHz cutoff, Dcblock	Cap, 0402	Knowles	P42BN820MA3152	20
L1, L2	15 nH	Inductor, 0402, 460 mA, SMD	Vishay	IMC0402ER15NG01	2
R2	49.9 Ohm	Res, 0402, 1%, 1/16W, SMD	Yageo	RC0402FR-0749R9L	1
R3	0 Ohm	Res, 0402, 1/16W, SMD	Yageo	RC0402JR-070RL	1
R1, R4		DNP			
R6-R9	100 Ohm	Res, 0402, 1%, 1/16W	Yageo	RC0402FR-07100RL	4
R10-R13	40.2k Ohm	Res, 0402, 1%, 1/16W	Yageo	RC0402FR-0740K2L	4
PCB		35 GHz RADAR Tx module - v1	GUF		2
PCB		35 GHz RADAR up-converter - v1	GUF		2
PCB		35 GHz RADAR push-pull amplifier - v1	GUF		2
PCB		35 GHz RADAR filter - v1	GUF		2

Table A-2: Rx bill of materials (complete)

Description	Manufacturer	Part Number	Qty/board
2.4 mm connectors	Southwest	1492-04A-6	1
SMA connectors	Southwest	292-07A-6	1
SMA connectors	Amphenol RF	901-10512-1	1
6-pin SMT ZIF Horizontal Low Profile DC	Würth Elektronik	687106183722	3
8-pin SMT ZIF Horizontal Low Profile DC	Würth Elektronik	687108183722	1
6-pin WR-FFC 0.50 mm Flat Flexible Cable Type 2 (Contacts opposite), 250 mm	Würth Elektronik	687706200002	3
8-pin WR-FFC 0.50 mm Flat Flexible Cable Type 2 (Contacts opposite), 250 mm	Würth Elektronik	687708200002	1
Low-Noise Amplifier (RF)	UMS	CHA2494-QEG	2
Attenuator	UMS	CHT4694-QAG	2
I/Q Downconverter	Analog Devices	HMC6789BLC5A	1
Hybrid 90°	Innovative Power Products	IPP-7116	1
Lowpass Filter	Mini-Circuits	LFCN-1575+	3
Low-Noise Amplifier (IF)	Analog Devices	HMC8410LP2FE	3
Highpass Filter	Mini-Circuits	RHP-65+	3
Mixer	Mini-Circuits	ADE-R5LH+	1
Cap, 0402 (Ceramic, 100V, 0.1 pF, C0G)	KEMET	CBR04C509B1GAC	1
Cap, Ceramic, 0402, 50V, 5%, NPO	Murata Manufacturing	GJM1555C1H200JB01J	6
Cap, 0402, 50V, 5%, NPO	Knowles	0402J1000101GCB	8
Cap, 0402, 50V, (10% enough) 5%, NPO	Murata Manufacturing	GCM155R71H103JA55D	8
Cap, 106 kHz and 40 GHz, 0502, broadband	Presidio Components	MBB0502X103MLP5N83	6
Cap, Ceramic, 0402, 50V, 5%, X5R	Murata Manufacturing	GRM155R61H104JE14D	11
Cap, Tantalum, Case A (3216 Pkg) (16V,10%)	KEMET	T495A225K016ATE2K5	3
Cap, Tantalum, Case A (3216 Pkg) (10V, 20%)	Vishay	T55A475M010C0200	9
Inductor, 0805, 360 mA, 2%	Coilcraft	0805HP-331XGRB	1
Inductor, Ferrite DF, 0402, 5%	Coilcraft	0402DF-591XJRU	6
Res, 0402, 1/16W, SMD	Yageo	RC0402JR-070RL	19
Res, 0402, 1/16W, SMD	Yageo	RC0402JR-0715RL	3
Res, 0402, 1/16W, SMD	Yageo	RC0402JR-0730RL	6
Res, 0402, 1/16W, SMD	Yageo	RC0402JR-0750RL	1
PCB, 3 pieces			

Annex B

Effects of saturation on high-gain receivers

We want to investigate the effects of overloading on receiver B1. The receiver comprises three stages of IF amplification and is expected to overload at an input power of -73.5 dBm.

a. Output spectrum

Figure B-1 shows the output spectrum of receiver B1, for the carrier frequency, 35 GHz and its corresponding image, 37 GHz. The LO2 is 950 MHz. The receiver input frequency is -70 dBm.

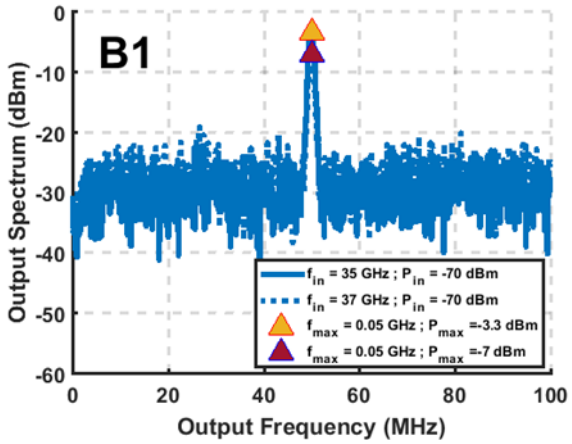

Figure B-1: Receiver B1 output spectrum measured with the FSW (LO1 = 18 GHz, LO2 = 950 MHz).

We see that the signal is correctly down-converted by the receiver B1. The measured output signal is around -3.3 dBm. Including the 0.94 dB-loss from the cable, B1 conversion gain at 35 GHz is around 67.6 dB, measured at instantaneous time. This is almost 8 dB lower than what is expected. The measured sideband suppression at 35 GHz is 3.7 dBc. Saturation does not cancel the conversion capacity of the receiver but seems to decrease its performance. It also seems to impair the sideband suppression.

b. Conversion gain

Figure B-2 shows the transmission parameter S12 of the receiver module measured with a CW Time sweep with a 35 GHz input. We see that the the conversion gain is around 70 dB. The signal is noisier than for B3 characterization. We further calculate the conversion gain of B1 by following the same approach as in Section 8.5.2. Figure B-3 shows the conversion gain. It is 60 dB typically. The conversion gain is indeed less than expected since the receiver is overloading at -70 dBm. Measurements at -80 dBm show that the receiver is already saturating. This would explain why they are particularly noisy: since the gain is decreasing, the impact of the receiver noise, 6.28 dB becomes predominant. We see that the conversion gain depends on both input power and on input frequency. There is a consequent difference in the conversion gain for B1 between -70 and -80 dBm input power around 35-35.5 GHz. The receiver still has the best performance around 35 GHz. Figure B-4 shows the conversion gain calculated from the output spectrum. The conversion gain is the difference between the peak of the output IF signal and the input power. The curves differ to previous measurements due to the noise fluctuation during spectrum measurements.

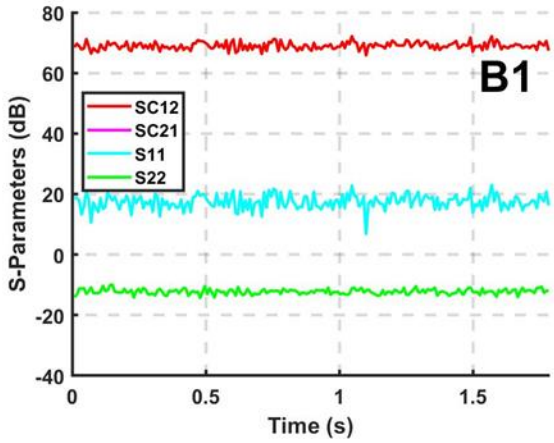

Figure B-2: S-parameters of B1 measure in CW Time with input power of -70 dBm

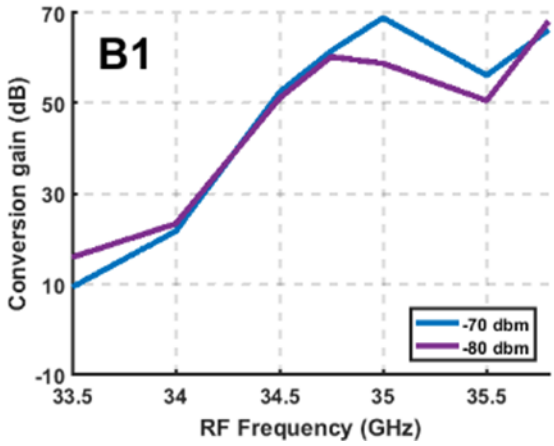

Figure B-3: Conversion gain measured with PNA-X on CW Time sweep at different input powers

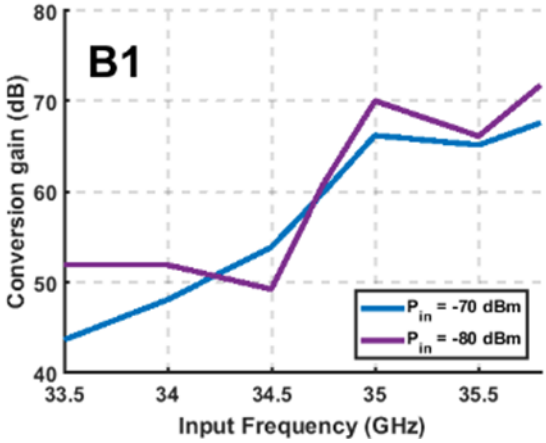

Figure B-4: Conversion gain measured with FSW at different input powers

c. Sideband Suppression

We measure the upper sideband suppression in two ways, following the same methods as in Section 8.5.3. Figure B-5 shows the image suppression for B1. The order of magnitude for both measurement types is quite constant: within the 34.5-35.8 GHz range, the suppression is between 3 and 7 dBc. Both measurements do not properly match because the sideband suppression calculated from the PNA-X CW time measurements are results of a mean over the time sweep, while curves calculated from FSW spectrum result from a snapshot at a given time. Spectrum measurements with FSW fluctuate because of the noise. This is especially true for low power measurements. Measurements with PNA-X are more reliable. Note that the image rejection is less than in HMC6789BLC5A datasheet because first, the down-converter operates

out-of-range; second, the lower sideband conversion does not perform as well as the USB. We also see that the image rejection is indeed degrading with larger IF amplification. This might be due to intermodulation products.

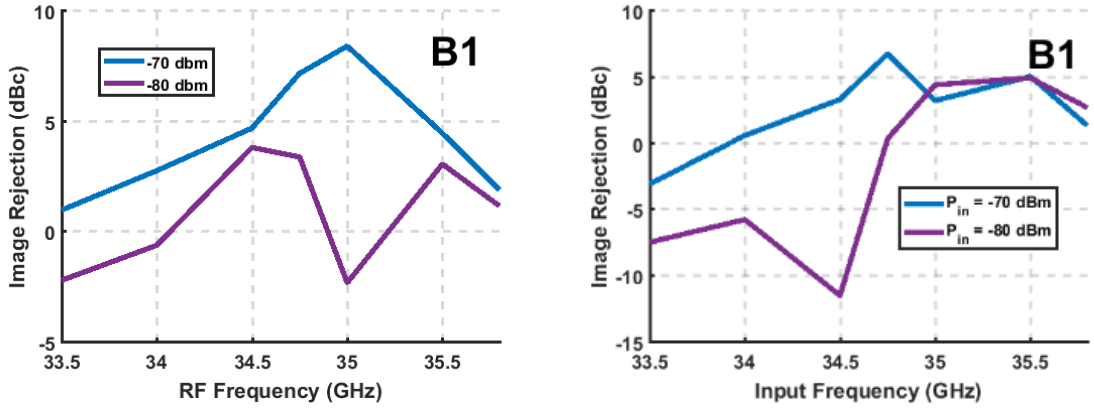

Figure B-5: Image rejection of B1 measured with PNA-X (left) and with the FSW (right) at different input powers.

d. Power performance

Figure B-6 shows the output power with respect to the input power for B1 at different frequencies. The output power is measured with the FSW and is once again a snapshot. However, we can see that the output power is much larger for frequencies above 34.5 GHz. This corroborates that the receiver operates at its best around 35 GHz.

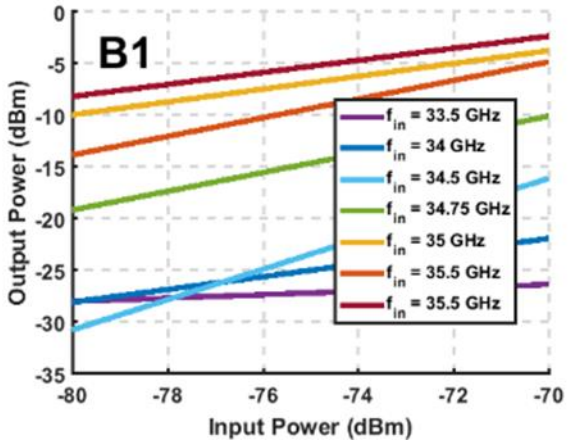

Figure B-6: Output power vs. input power measured with the FSW at different input frequencies.

e. Bandwidth characterization and feasibility validation for FMCW radar

We characterize the bandwidth of receiver B1 as described in Section 8.5.5 and the results are displayed in Figure B-7.

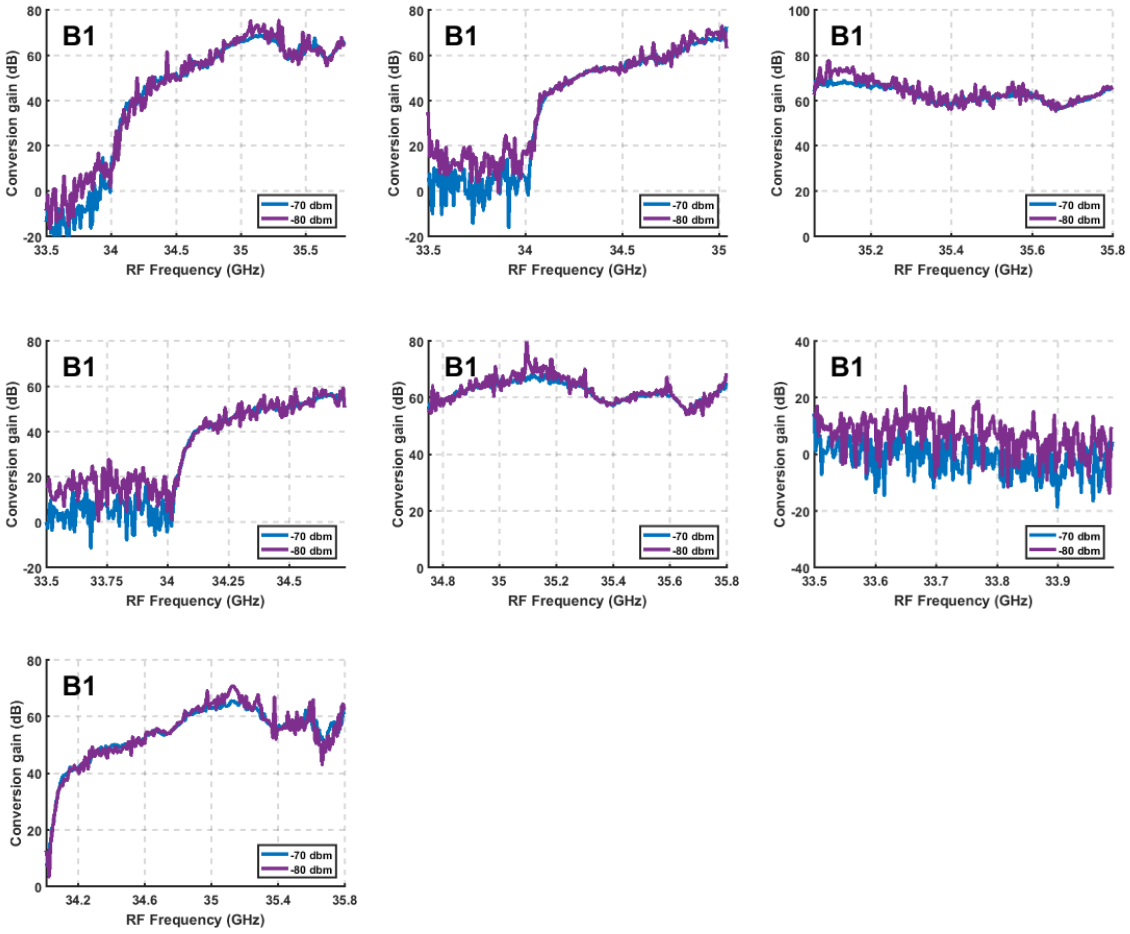

Figure B-7: S-parameters of board B1 measured with PNA-X on Linear Frequency sweep at different input powers

when LO1 = 18 GHz and: 1) RF = [33.5-35.8] GHz, LO2 = 190 MHz; 2) RF = [33.5-35.04] GHz, LO2 = 190 MHz; 3) RF = [35.06-35.8] GHz, LO2 = 190 MHz; 4) RF = [33.5-34.73] GHz, LO2 = 1260 MHz; 5) RF = [34.75-35.8] GHz, LO2 = 1260 MHz; 6) RF = [33.5-33.99] GHz, LO2 = 2000 MHz; 7) RF = [34.01-35.8] GHz, LO2 = 2000 MHz.

The trend stays the same as for receiver B3. We see that a-70 dBm input signal gives a much smoother output signal than with the -80 dBm input. This was anticipated as the receiver is overlading, the gain is going down, and the noise of the receiver is more visible.

List of Figures

List of Tables

Acknowledgments

First of all, I would like to thank my supervisor Prof. Viktor Krozer for trusting me to pursue this research work, for his guidance throughout my thesis and for his support both professionally and personally. Many thanks to Prof. Visvanathan Ramesh for being so kind to review my dissertation and to Prof. Marc Wagner and Prof. Hartmut Roskos for agreeing to being part of the defence committee. Thank you all for your fruitful feedback, professional advice and for making the defence nice and memorable.

I would also like to thank my co-supervisor Prof. Tom K. Johansen for his guidance and eternal enthusiasm and Prof. Vitaliy Zhurbenko for giving me the opportunity to assist him in his teaching. Many thanks to Olof Bengtsson, Andreas Kaiser, Steffen Schulz, Armin Liero and Andreas Wentzel for their help in the lab. I am thankful to Hui, Amit, Dovile, Yunfeng, Bruno, Sophie, Ralf and the rest of my colleagues from the Goethe University Frankfurt, the Technical University of Denmark, the Ferdinand-Braun-Institut and the CELTA group for the numerous dinners, nights out and the incredible atmosphere in the office. I am thankful to my colleagues from the Max Planck Institute for Radio Astronomy for their support in the last steps of the thesis.

I wish to thank EU Horizon 2020 Marie Sklodowska-Curie ITN CELTA project, RAMMS project and DLR MIMIRAWE project for their financial support to accomplish this doctoral thesis.

I would like to express my warmest gratitude to my dear friends all around the world for their constant support during this journey – from Germany: Daniel, Sara, Sonjati, Fairooz, Miss Tobi, Jared, Ellie, Lisa, Alioune, Andy, the Mülheimer Mädels, Franzi and Amaya; from Denmark: Naveeda, Emil, Bodil and Foto; from France: Lexou, Olive, Mémé, Daphi, Soso, Eric and Carole and from other time zones: Beubeu, Connie, Momti, Lorenzo, Jannie, Herbert, Kell and Yase. Thanks for the many encouragement speeches, long phone calls and simply for being there.

Finally, I wish to deeply thank my family for always being by my side. Many many thanks to my sisters Aurélie and Ghislaine for their unconditional support, to my godmother/mentor Marie-Laure for her valuable guidance, to my godmother Mélanie, their families, Martin, Tata and my father. Special thanks to my nephews Paul and Julie, you are my rock.

I dedicate this thesis to my mother.